DTU Wind Energy

DANAERO MW: Final Report

Department of Wind Energy Report 2013

Niels Troldborg, Christian Bak, Helge Aa. Madsen, Witold Skrzypinski

DTU Wind Energy E-0027

April 2013

DTU Vindenergi
Institut for Vindenergi

Author(s): Niels Troldborg, Christian Bak, Helge Aa. Madsen, Witold Skrzypiński
Title: DANAERO MW: Final report
Institute: DTU Wind Energy

DTU Wind Energy E-0027
April 2013

Summary:
This report describes the results of the EUDP funded DANAERO MW II project carried out by DTU Wind Energy (formerly Risø DTU) and the industrial partners, LM Wind Power, Vestas Wind Systems A/S and Siemens Wind Power. An overview of the data available from the project as well as the results from analysis of the data is given with the main objective to explore in detail the influence of atmospheric and wake turbulence on MW turbine performance, loading and stability. Finally, validation and demonstration of simulation codes are carried out.

ISSN 0106-2840
ISBN 978-87-92896-39-1

Contract no.:
64009-0258

Project no.:
43016

Sponsorship:
EUDP 2009-II

Cover:
Photograph of instrumented NM80 turbine at the Tjæreborg Enge site

Pages: 143
Tables: 23
References: 126

Technical University of Denmark
Deparment of Wind Energy
Frederiksborgvej 399
Building 118
DK-4000 Roskilde
Telephone
+45 4677 5085
www.vindenergi.dtu.dk

Preface

The present report is the final document in the project "DANAERO MW II: Influence of atmospheric and wake turbulence on MW turbine performance, loading and stability". The project was partly funded funded by EUDP2009-II and partly funded by the project partners (Vestas Wind Systems, LM Wind Power, Siemens Wind Power, DTU Wind Energy) themselves.

The investigations in chapter 14 in which full rotor simulations using Computational Fluid Dynamics (CFD) are validated by comparing with DANAERO MW measurements was supported by the project "Center for Computational Wind Turbine Aerodynamics and Atmospheric Turbulence" contract no.: 2104-09-0026.

The authors would like to thank all the involved partners for their invaluable help and support. Also, special thanks are given to Niels Sørensen and Pierre-Elouan Réthoré in the project "Center for Computational Wind Turbine Aerodynamics and Atmospheric Turbulence" for providing the numerical grids used for the investigations in chapter 14.

Technical University of Denmark, April 2013

Niels Troldborg, Christian Bak, Helge Aa. Madsen and Witold Skrzypiński

Contents

1 Summary

This section summarizes the main results of the DANAERO MW II project.

- **Calibration and organization of database**
  The extensive data obtained in the Tjæreborg experiment as part of the DANAERO MW project have been calibrated and a thorough description of the calibration procedures is provided. The calibration also includes synchronization of the measurements obtained with the different systems. Furthermore, all data from the experiment have been organized in files which are easy to read with standard analysis software. Finally, a MySQL database containing most of the data from the Tjæreborg and Høvsøre experiment, including a variety of derived quantities and some statistics, have been build along with tools for sorting and binning the data.

- **Analysis of measurements**
  The conclusions drawn from the analysis of measurements can roughly be divided as follows:

  – *2D/3D aerofoil data*
  Comparisons of the aerodynamic aerofoil characteristics measured in 2D in a wind tunnel with the corresponding characteristics measured in 3D full scale and atmospheric conditions revealed the following (see chapter 6 and 9): 1) For angles of attack (AoA) just larger than the AoA of maximum normal force coefficient, c_n, a lower negative slope of the c_n curve is measured on the blade sections of the NM80 turbine than on the corresponding aerofoils in a wind tunnel. Whether this is due to 3D effects or the absence of wall effects is not fully known. 2) In the 3D case a delay of separation was observed due to centrifugal and Coriolis forces which, especially for the inner section (r/R=0.325), caused an increase in c_n for AoA above maximum c_n compared to wind tunnel measurements. 3) For the outermost section (r/R=0.925) the overall level and slope of the c_n curve was lower than measured in 2D in a wind tunnel. 4) For the mid span sections of the turbine the aerofoil characteristics was found to be fairly 2D.

  – *Aerofoil data measured in different tunnels*
  A comparison of the aerodynamic polars measured on the same aerofoils in different wind tunnels revealed the following (see chapter 8): 1) The measured zero-lift-angle-of-attack, slope of the linear part of the lift curve, maximum lift, stall characteristics and drag, respectively, is different in each wind tunnel. 2) The agreement between the measurements improved with increasing Reynolds number. 3) The minimum drag seems to be unaffected by the turbulence intensity (TI) in the tunnel provided that $TI < 0.1\%$. For $TI > 0.1\%$ the minimum drag is influenced by the level of TI. 4) TI affects the location of the transition point and hence also the aerofoil performance. 4) No clear correlation between the lift curve characteristics and the wind tunnel layout could be identified. 5) Most of the differences between the measurements are ascribed to differences in aerofoil model shapes, methods for analysing the data and calibrations.

  – *Standstill*
  As described in chapter 10 extracting lift and drag polars from standstill measurements on the NM80 turbine proved to be difficult. The overall quality of the polars was unsatisfactory which seemed to be due to combined uncertainties in the measurements of all parameters involved in deriving the polars, i.e. angle of attack, wind speed and pressure distribution. The reason for the uncertainties was that the used equipment for measuring the polars were calibrated to work under normal operation and not at standstill. Thus, it seemed that an increase in quality of all the involved measurements, especially the pressure distribution, would be necessary to obtain reliable polars in standstill.

– *Transition*
A robust method for detecting transition from laminar to turbulent boundary layer from high frequency microphone measurements of the sound pressure level (SPL) has been proposed (see chapter 7). The method has been applied to the entire dataset obtained in the Tjæreborg experiment and the estimated positions of the transition points on both suction and pressure side have been included as a derived quantity in the database.

– *Noise*
In relation to wind turbine noise the following findings was achieved by analysing surface pressure (SP) measurements on an outboard blade section of the NM80 turbine and wind tunnel measurements on an identical aerofoil section (see chapter 12): 1) At low frequencies, increasing the angle of attack (AoA) yields an increase in SP spectral energy at the trailing edge (TE), and thereby TE noise in the far-field. At high frequencies the opposite is true. 2) For a wind turbine operating in wake the SP fluctuations near the leading edge (LE) is increased at low frequencies due to the inflow turbulence associated with the wake whereas the spectral energy of the SP fluctuations near the TE increases at high frequencies, which is a consequence of the different turbulent boundary layer characteristics created at the TE by the inflow turbulence as observed in the wind tunnel.

- **Validation and demonstration of simulation models**
A thorough validation and demonstration of various models have been conducted. The investigations included validation of computational fluid dynamics (CFD) models, blade element momentum (BEM) based methods, aeroelastic models and noise models. To facilitate the validation specific test cases from the Tjæreborg measurements were selected and described in a report. The main conclusions from the validation of the different models are:

  – *CFD based models*
  A comparison of different CFD models with measurements of the NM80 turbine operating in nearly non-sheared inflow revealed the following (see chapter 14): 1) Generally the computed aerodynamic forces and surface pressure distributions were in good agreement with measurements. 2) The standard deviation in the measurements made it difficult to conclude whether including a transition model improved the simulations. 3) Most of the physics could be captured without considering the inflow turbulence in the simulations.
  A comparison of computed aerofoil characteristics with measurements showed the following (see chapter 9): 1) 2D computations of lift and drag on aerofoils with relative thickness below 24% agree fairly well with wind tunnel measurements at low and moderate AoA but showed important differences at AoA above maximum lift. 2) For the thickest considered aerofoil (relative thickness of 33%) large differences were observed between wind tunnel measurements and computations at all AoA. The differences are likely to be due to wall effect in the tunnel but could also be because it may be inadequate to simulate thick aerofoils at high AoA using 2D CFD. 3) Comparison of aerofoil characteristics obtained from 3D rotor CFD and measurements generally revealed good agreement for all blade sections and AoA. This finding supports the conclusion that the differences between wind tunnel measurements and 2D aerofoil computations are due to wall effects in the tunnel.
  Furthermore, simulations of the inflow and loads on the NM80 turbine operating partly in the wake of another turbine were carried out using the Navier Stokes solver EllipSys3D and an actuator line technique (see chapter 11). A comparison with corresponding measurements revealed fair qualitatively agreement but showed also some significant quantitative differences. The differences are likely to be a consequence of uncertainties in the ambient conditions but also because the blades were assumed stiff in the simulations.

- *BEM based models*
  A comparison of different BEM models with measurements of the NM80 turbine operating in various inflow conditions revealed the following (see chapter 15): 1) In non-sheared inflow the different models agree well with each other and reasonably well with measurements. 2) In sheared and yawed inflow the differences between BEM computations and measurements are much larger. 3) More investigations are needed to explain fully the discrepancies but some of them are due to inaccurate aerofoil data. 4) The inaccuracy of the aerofoil data shows the importance of correcting aerofoil data obtained in wind tunnels before using them in BEM computations.

- *Noise models*
  Based on analysis of sound pressure (SP) measurements on the NM80 wind turbine the model by Amiet for turbulent inflow (TI) noise and the TNO-Blake model for trailing edge (TE) noise modelling were validated. The conclusions from this study are (see chapter 13): 1) A general good agreement between the model and measurement data was found. However, some discrepancies between the SP measured at the TE on the NM80 wind turbine and the TNO-Blake model were observed. These differences could however be explained by the presence of a turbulent inflow impacting the turbine blade which was not accounted for in the model. 2) For both TI and TE noise models, the use of the Von Karman spectrum for describing the respective turbulence characteristics may be source of errors at very low frequencies. 3) For the TE noise model, the assumption of uncorrelated vortex sheets across the turbulent boundary layer may also yield poor results at low frequencies.

- **Coordination of DANAERO MW measurements with other measurements**
  Chapter 4 in the present report describes three measuring campaigns which were undertaken simultaneously with the DANAERO Tjæreborg experiment at the same site as part of other projects. The chapter further documents where the different projects were running in parallel and thus potentially might provide simultaneous measurements of inflow, loads and wake conditions, which would make these datasets very extensive and unique.

Besides the results presented in this report the following publications where made as part of the DANAERO MW II project:

Internal documents:

C. Bak, H.Aa. Madsen, M. Gaunaa, U. Paulsen, P. Hansen, M. Rasmussen, P. Fuglsang, P. Enevoldsen, J. Laursen, and J. Romblad. DAN-AERO MW: Wind tunnel tests. Technical Report Risø-I-3047(EN), Technical University of Denmark, 2010.

C. Bak, H.Aa. Madsen, P. Hansen, M. Rasmussen, P. Fuglsang, J. Romblad, and N.A. Olesen. DAN-AERO MW: Measurement campaigns on the NM80 2.3MW turbine at Tjæreborg 2009. Technical Report Risø-I-3046(EN), Technical University of Denmark, 2010.

C. Bak, H.Aa. Madsen, N. Troldborg, M. Gaunaa, W. Skrzypiński, A. Fischer, U. Paulsen, R. Møller, P. Hansen, M. Rasmussen, and P. Fuglsang. DANAERO MW: Instrumentation of the NM80 turbine and meteorology mast at Tjæreborg . Technical Report DTU Wind Energy Report-I-0083, Technical University of Denmark, 2013.

C. Bak, H.Aa. Madsen, N. Troldborg, N.N. Sørensen, and J. Madsen. DANAERO MW: Data for the NM80 turbine at Tjæreborg Enge for aerodynamic evaluation. Technical Report DTU Wind Energy Report-I-0087, Technical University of Denmark, 2013.

C. Bak, H.Aa. Madsen, N. Troldborg, and J.J Wedel-Heinen. DANAERO MW: Data for the NM80 turbine at Tjæreborg Enge for aeroelastic evaluation. Technical Report DTU Wind Energy Report-I-0088, Technical University of Denmark, 2013.

M. Døssing, H.A. Madsen, C. Bak, A. Fischer, N. Troldborg, P. Hansen, and Bertagnolio F. High frequency microphone measurements for detection of transition on airfoils. Technical

Report Risø-I-3177(EN), Risø-DTU, Roskilde, Denmark, 2011.

M. Døssing, H.A. Madsen, C. Bak, A. Fischer, N. Troldborg, P. Hansen, and Bertagnolio F. DAN-AERO MW II: High frequency microphone measurements for detection of transition on airfoils. appendix report 20090625-20090716. Technical Report Risø-I-3178(EN), Risø-DTU, Roskilde, Denmark, 2011.

M. Døssing, H.A. Madsen, C. Bak, A. Fischer, N. Troldborg, P. Hansen, and Bertagnolio F. DAN-AERO MW II: High frequency microphone measurements for detection of transition on airfoils. appendix report 20090721-20090806. Technical Report Risø-I-3179(EN), Risø-DTU, Roskilde, Denmark, 2011.

M. Døssing, H.A. Madsen, C. Bak, A. Fischer, N. Troldborg, P. Hansen, and Bertagnolio F. DAN-AERO MW II: High frequency microphone measurements for detection of transition on airfoils. appendix report 20090807-20090818. Technical Report Risø-I-3180(EN), Risø-DTU, Roskilde, Denmark, 2011.

M. Døssing, H.A. Madsen, C. Bak, A. Fischer, N. Troldborg, P. Hansen, and Bertagnolio F. DAN-AERO MW II: High frequency microphone measurements for detection of transition on airfoils. appendix report 20090819. Technical Report Risø-I-3181(EN), Risø-DTU, Roskilde, Denmark, 2011.

M. Døssing, H.A. Madsen, C. Bak, A. Fischer, N. Troldborg, P. Hansen, and Bertagnolio F. DAN-AERO MW II: High frequency microphone measurements for detection of transition on airfoils. appendix report 20090827-20090901. Technical Report Risø-I-3182(EN), Risø-DTU, Roskilde, Denmark, 2011.

M. Døssing, H.A. Madsen, C. Bak, A. Fischer, N. Troldborg, P. Hansen, and Bertagnolio F. DAN-AERO MW II: High frequency microphone measurements for detection of transition on airfoils. appendix report 20090909-20090911. Technical Report Risø-I-3183(EN), Risø-DTU, Roskilde, Denmark, 2011.

N. Troldborg. DAN-AERO MW: Potential benchmark cases from the Tjæreborg campaign. Technical Report DTU Wind Energy Report-I-0090, DTU Wind Energy, 2013.

Public documents:

C. Bak, H.A. Madsen, U.S. Paulsen, M. Gaunaa, N.N. Sørensen, P. Fuglsang, J. Romblad, N.A. Olesen, P. Enevoldsen, J. Laursen, and L. Jensen. DAN-AERO MW: Comparisons of airfoil characteristics for two airfoils tested in three different wind tunnels. *Torque conference, Crete, Greece*, 2010.

C. Bak, H.A. Madsen, and N. Troldborg. DAN-AERO MW: Experimental aerodynamics and aeroacoustics of wind turbines in atmospheric conditions. Part I. *To be submitted for Wind Energy*, 2013.

C. Bak, H.A. Madsen, N. Troldborg, F. Bertagnolio, A. Fischer, and W. Skrzypiński. DAN-AERO MW: Experimental aerodynamics and aeroacoustics of wind turbines in atmospheric conditions. Part II. *To be submitted for Wind Energy*, 2013.

C. Bak, N. Troldborg, and H.A. Madsen. DAN-AERO MW: Measured airfoil characteristics for a MW rotor in atmospheric conditions. *EWEA, Brussels, Belgium*, 2011.

F. Bertagnolio, H.Aa. Madsen, C. Bak, N. Troldborg, and A. Fischer. Aerodynamic Noise Characterization of Full-Scale Wind Turbine through High-Frequency Surface Pressure Measurements. *Submitted for publication in Journal of Sound and Vibration*, 2013.

A. Fischer and H.A. Madsen. Investigation of the maximum load alleviation potential using trailing edge flaps controlled by inflow data. *Torque conference, Oldenburg, Germany*, 2012.

W. Skrzypiński and M. Gaunaa. Wind turbine blade vibration at standstill conditions - the effect of imposing lag on the aerodynamic response of an elastically mounted airfoil. *Submitted to*

Wind Energy, 2013.

W. Skrzypiński, M. Gaunaa, N.N. Sørensen, F. Zahle, and J. Heinz. Self-induced vibrations of a du96-w-180 airfoil in stall. *Submitted to Wind Energy*, 2013.

W. Skrzypiński, M. Gaunaa, N.N. Sørensen, F. Zahle, and J. Heinz. Vortex-induced vibrations of a du96-w-180 airfoil at 90 degrees angle of attack. *Submitted to Wind Energy*, 2013.

N. Troldborg, C. Bak, N.N. Sørensen, H.Aa. Madsen, P-E. Réthoré, F. Zahle, and S. Guntur. Experimental and numerical investigation of 3D aerofoil characteristics on a mw wind turbine. *EWEA, Vienna, Austria*, 2013.

2 Introduction

In the DANAERO MW project, which is an abbreviation for the EFP2007 project "Experimental Rotor and Airfoil Aerodynamics on MW Wind Turbines", a number of innovative and coordinated measurements on two modern full scale MW turbines as well as wind tunnel measurements on various airfoil sections were conducted. The project was carried out in the period from March 2007 to December 2009 in a corporation between RisøDTU and the companies LM Wind Power, Vestas Wind Systems, Siemens Wind Power and DONG Energy.
The outcome of the DANAERO MW project was a comprehensive and unique dataset, which contains data that the wind energy research community and the industry can benefit from in the next many years.

As a follow up on the project the EUDP funded DANAERO MW II project was established in 2010 with the participant RisøDTU (now DTU Wind Energy), LM Wind Power, Vestas Wind Systems A/S and Siemens Wind Power. The overall objective of DANAERO MW II is to use the data obtained in DANAERO MW to explore in detail the influence of atmospheric and wake turbulence on MW turbine performance, loading and stability. In order to achieve this the following work packages (WPs) were formulated in the DANAERO MW II project

- **WP1: Calibration and organization of database**
  The aim of this work package is to calibrate and organize the data from the DANAERO MW project and build a database together with tools for sorting and binning.
- **WP2: Analysis of measurements**
  The objective of this work package is to analyse the measurements with the aim of revealing the influence of atmospheric and wake turbulence on aerodynamic, aeroelastic and aeroacoustic characteristics and in general improve the design basis for MW rotors. A main part of the analysis is aimed at comparing aerodynamic characteristics obtained in 2D in a wind tunnel with the corresponding characteristics in 3D full scale and atmospheric conditions.
- **WP3: Validation of models**
  The objective of this work package is to demonstrate the validity of existing models and sub models for modelling aerodynamics, aeroelastics and wind turbine noise by making thorough comparisons with the measurements obtained in the DANAERO MW project.
- **WP4: Demonstration of influence of new models**
  The aim of this work package is a demonstration of the influence of the new findings on the wind turbine design, sitting, operation and performance verification by use of the complete design complex.
- **WP5: Coordinate the DANAERO MW measurements with other measurements**
  The purpose of this work package is to document the relation of the measurements carried out in the DANAERO project with related measurement campaigns carried out in parallel as part of other projects.

This final report describes the overall results of the DANAERO MW II project. In accordance with the objectives set in the project work packages the report is divided into three parts

- Part I: Data overview
- Part II: Analysis of data
- Part III: Validation of models

Part I: Data overview

3 Available data

Author(s): N. Troldborg

This section gives a brief overview of all the data available in the DANAERO MW experiment including the data contained in the database.

3.1 The Tjæreborg experiment

In this part of the DANAERO experiment a 2.3MW NM80 turbine located at the Tjæreborg Enge site and a nearby met mast were both heavily instrumented with various sensors.
The layout of the wind farm is sketched in Figure 3.1 and consists of 8 turbines organized in two rows. The turbines in the southern row and the instrumented turbine, denoted WT3, are all of the NM80 type, while the others are Vestas V80's.
The measurement campaign at the site was carried out in the summer of 2009 from July 16^{th}

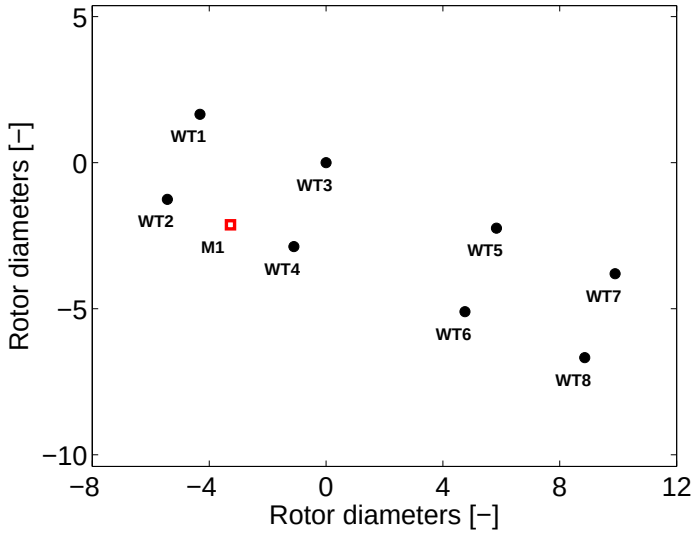

Figure 3.1. Layout of Tjæreborg Enge wind farm

to September 11^{th}. A detailed description of the instrumentation and acquired data is provided in [1] and here only a brief overview will be given.
Tables 3.1-3.3 summarizes the instrumentation of the blade, tower, nacelle, drive train and met mast. All data except for the surface pressure tap measurements and the surface microphone measurements are sampled at 35 Hz. Three different systems were used to acquire the data: The ScaniValve system which handled the surface pressure measurements, the cRIO system which handled the microphone measurements and the DaqWin system, which handled the remaining sensors.

Instrument	Sensor	Position [m]	Sampling rate [Hz]
Strain gauges	Flapwise and edgewise moments	{3.0, 8.0, 13.0, 16.0, 19.0, 22.0, 26.0, 30.0, 34.0, 37.0}	35
Five-hole Pitot tubes	Relative velocity and flow angles	{14.5 20.3, 31.0, 36.0}	35
Pressure taps	Surface pressure	{13.0, 19.0, 30.0, 37.0}	100
Accelerometers	Acceleration	{13.0, 19.0, 30.0, 37.0}	35
Thermometer	Blade temperature	{13.0, 19.0, 30.0, 37.0}	35
Microphones	Surface pressure	37.0	50000

Table 3.1. Instrumentation on the LM38.8 blade

Instrument	Sensor	Position	Sampling rate [Hz]
Strain gauges	Tower moments	Tower top/bottom	35
Strain gauges	Shaft moments	Shaft	35
-	Electrical power	nacelle	35
-	Rotor azimuth angle	nacelle	35
-	Rotational speed	nacelle	35
-	Yaw angle	nacelle	35
-	Pitch angle	nacelle	35
Cup anemometer	Wind speed at nacelle	nacelle	35

Table 3.2. Instrumentation of tower, nacelle and drive train

Instrument	Sensor	Height [m]	Sampling rate [Hz]
Cup anemometers	Wind speed	{17.0, 28.5, 41.0, 57.0, 19.0, 77.0, 93.0}	35
Sonic anemometers	Velocity, wind direction and temperature	{17.0, 57.0, 93.0}	35
Wind vanes	Wind direction	{17.0, 57.0, 93.0}	35
Thermometer	Temperature	{5.7 57.0, 93.0}	35
Barometer	Pressure	5.7	35
-	Precipitation	5.7	35

Table 3.3. Instrumentation of the nearby met mast

3.2 Wind tunnel measurements

As part of the DANAERO MW experiment a number of wind tunnel tests on different aerofoils were also carried out in different wind tunnels. A detailed description of the various tests is given in [2] and here only a summary will be given.
The objective of the wind tunnel tests were

- Benchmarking wind tunnels by testing each of the DU96-W-180, NACA63418 and Risø-B1-18 aerofoils in the LM Wind Power, Delft and VELUX wind tunnels, respectively.

- Testing copies of the four blade sections of the LM38.8 blade which were instrumented with pressure taps (see Table 3.1) during the tests on the NM80 wind turbine at Tjæreborg Enge, Denmark.

In all the performed tests the pressure distribution as well as the lift, drag, moment, normal force and tangential force coefficient are available as a function of angle of attack.
Tables 3.4- 3.6 give an overview of all the tests which were carried out.

Aerofoil	Configuration	Re $[10^6]$
LM38.8 (r=13.0 m)	Clean	{1.5, 3.1, 4.1, 5.1, 6.1}
LM38.8 (r=13.0 m)	Various roughness	{3.1, 6.1}
LM38.8 (r=19.0 m)	Clean	{1.5, 3.0, 4.1, 5.1, 6.1}
LM38.8 (r=19.0 m)	Various roughness	{3.0, 6.1}
LM38.8 (r=30.0 m)	Clean	{1.5, 3.0, 4.1, 5.1, 6.1}
LM38.8 (r=30.0 m)	Various roughness	{3.1, 6.1}
LM38.8 (r=37.0 m)	Clean	{1.5, 3.0, 4.1, 5.1, 6.1}
LM38.8 (r=37.0 m)	Various roughness	{3.1, 6.1}
DU96-W-180	Clean	{1.5, 3.0, 4.0, 5.0, 6.0}
DU96-W-180	Various roughness	{3.0, 6.0}
NACA63-418	Clean	{1.5, 3.0, 4.0, 5.0, 6.0}
NACA63-418	Various roughness	{3.0, 6.0}
Risø-B1-18	Clean	{1.5, 3.0, 4.0, 5.0, 6.0}
Risø-B1-18	Various roughness	{3.0, 6.0}

Table 3.4. Tests carried out in the LM Wind Power wind tunnel

Aerofoil	Configuration	Re $[10^6]$
NACA63-418	Clean	{1.6, 3.0}
NACA63-418	Zigzag tape	{1.6, 3.0}
NACA63-418	Grid	3.0
Risø-B1-18	Clean	{1.6, 3.0}
Risø-B1-18	Various zigzag tape	{1.6, 3.0}

Table 3.5. Tests carried out in the Delft wind tunnel

Aerofoil	Configuration	Re $[10^6]$
DU96-W-180	Clean	1.6
DU96-W-180	Zigzag tape	1.6
NACA63-418	Clean	1.6
NACA63-418	Zigzag tape	1.6
Risø-B1-18	Clean	1.6
Risø-B1-18	Zigzag tape	1.6

Table 3.6. Tests carried out in the VELUX wind tunnel

3.3 Høvsøre measurements

The final measurement campaign carried out within the DANAERO project is the inflow measurements with a five-hole Pitot tube mounted on one of the blades of the Siemens 3.6MW

turbine at the Høvsøre test site for large wind turbines in Denmark [3, 4]. The five hole pitot tube was mounted in radius 36.5 m on the leading edge of one of the blades of the 107 m diameter rotor.
The data available from this experiment was obtained in the period from late April 2009 until mid July 2009. Table 3.7 lists the instrumentation and type of data measured throughout the experiment.

Sensor	Sampling rate
Local velocity and flow angle from Pitot tube	25
Wind speed and direction at hub height from met mast	25
Electrical power (averaged over 10 s)	35
Rotor speed (averaged over 10 s)	25
Rotor azimuth position	25
Air temperature and density	25

Table 3.7. Instrumentation on the Siemens 3.6MW at Høvsøre

3.4 Database

All the data from the three experiments are available in data files with formats as explained in [1–3].
In addition to this, most of the data from the Høvsøre and Tjæreborg experiment have been gathered in a database, which is designed to ease searching for specific data.
From the Høvsøre experiment all data including the 10 minute statistics (mean, minimum, maximum and standard deviation) is available in the database.
From the Tjæreborg experiment the database contains 35 Hz measurements and 10 minute statistics (mean, minimum, maximum and standard deviation) of all the data acquired by the DaqWin system (see Tables 3.1 -3.3) as well as down sampled surface pressure measurements from five selected pressure taps at each of the four blade sections. Besides the data obtained directly from the instruments in Table 3.1-3.3 a number of derived quantities are also included from the Tjæreborg experiment as summarized in Table 3.8. Note that in the database all data acquired by the three different systems (see section 3.1) are synchronized using dedicated pulse signals.

Quantity	Position [m]	Note
Load normal to chord	{13.0, 19.0, 30.0, 37.0}	From integration of surface pressure distribution
Load parallel to chord	{13.0, 19.0, 30.0, 37.0}	From integration of surface pressure distribution
Moment around quarter chord	{13.0, 19.0, 30.0, 37.0}	From integration of surface pressure distribution
Spanwise, tangential and normal velocity	{14.5 20.3, 31.0, 36.0}	From Pitot tube measurements
Air density	-	Derived from pressure and temperature at met mast
Transition points on upper and lower airfoil surface	37	Derived from microphone measurements
Syncronized time	-	Derived from trigger signals

Table 3.8. Derived quantities included in the database

References

[1] C. Bak, H.Aa. Madsen, N. Troldborg, M. Gaunaa, W. Skrzypiński, A. Fischer, U. Paulsen, R. Møller, P. Hansen, M. Rasmussen, and P. Fuglsang. DANAERO MW: Instrumentation of the NM80 turbine and meteorology mast at Tjæreborg . Technical Report DTU Wind Energy Report-I-0083, Technical University of Denmark, 2013.

[2] C. Bak, H.Aa. Madsen, M. Gaunaa, U. Paulsen, P. Hansen, M. Rasmussen, P. Fuglsang, P. Enevoldsen, J. Laursen, and J. Romblad. DAN-AERO MW: Wind tunnel tests. Technical Report Risø-I-3047(EN), Technical University of Denmark, 2010.

[3] H.Aa. Madsen, C. Bak, U.S. Paulsen, and L. Na. DAN-AERO MW: Overview of inflow data on the Siemens 3.6 MW turbine at Høvsøre . Technical Report Risø-I-3067, Technical University of Denmark, 2010.

[4] H.Aa. Madsen, C. Bak, U.S. Paulsen, M. Gaunaa, P. Fuglsang, J. Romblad, N.A. Olesen, P. Enevoldsen, J. Laursen, and L. Jensen. The DAN-AERO MW Experiments Final report. Technical Report Risø-R-1726(EN), Technical University of Denmark, 2010.

4 Relation to other measuring campaigns

Author(s): N. Troldborg

During the DANAERO Tjæreborg experiment a number of other measuring campaigns were undertaken simultaneously at the site as part of other projects. This section describes each of these projects and how they are related to the DANAERO project.

4.1 The TOPFARM project

The EU project TOPFARM was running from 1^{st} December 2007 to 30^{th} November 2010, and addressed optimization of wind farm topology and control strategy based on aero-elastic modelling of loads as well as of power production [1]. As part of the TOPFARM project a full scale wake measurement campaign was held at Tjæreborg Enge wind farm (see Figure 4.1) where the instrumented NM80 turbine from the DANAERO project was equipped with a downwind scanning LIDAR in the period from February to September 2009.
The following instrumentation is available from the Tjæreborg Enge wind farm within the

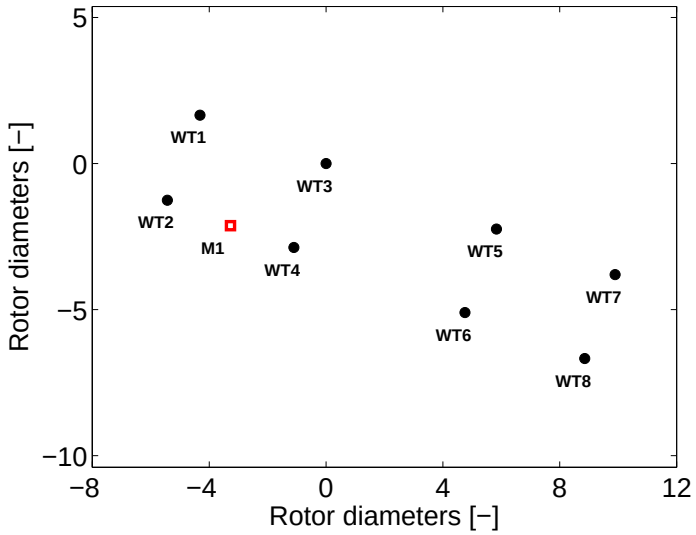

Figure 4.1. Layout of Tjæreborg Enge wind farm

TOPFARM project:

- SCADA data from WT1-WT2 and WT4-WT8 (see Figure 4.1).
- 1 Hz recordings of the WT3 controller values for power, pitch, yaw position and rotational speed
- 10 minute statistics of the meteorological signals from the 93 m mast, MM (see Figure 4.1).
- Focuses LIDAR mounted on nacelle of WT3, performing at 348 Hz.

The data from the experiment is partly available in the Database of Wind Characteristics [2] and in an internal network drive.
On the final day (September 11^{th}) of the TOPFARM Tjæreborg experiment the LIDAR system was mounted on a movable crane lift, placed downstream in a direction perpendicular to the rotor plane of the turbine, thus enabling successive scanning campaigns of different parts of the rotor plane [3]. It should be mentioned that the yaw position recordings of the turbines

WT01-WT02 and WT04-WT08 are not correct due to individual offset errors and cannot be used without a correction [4].

4.2 The WindScanner.dk facility

As part of the activities of the Danish research infrastructure facility WindScanner.dk [5, 6] a measuring campaign was conducted where the Tjæreborg NM80 turbine (WT03) was equipped with an upwind scanning spinner LIDAR [7, 8]. The experiment took place from the beginning of April 2009 until the 11^{th} of September 2009.
During this experimental campaign the following instrumentation was available:

- 1 Hz recordings of the WT03 controller values for power, pitch, yaw position and rotational speed
- 10 Hz recordings of wind speed and direction measured by cup anemometers and wind vanes, respectively at various heights on the met mast.
- 20 Hz recordings of velocity from sonic anemometers at various height on the met mast
- 50 Hz recordings of an upwind scanning ZephIR LIDAR mounted in the spinner of WT03.

In the period from July $7th$ to August 27^{th} the spinner LIDAR was equipped with a 30^{o} optical wedge prism and the focus distance was set to 53 m. On September 11^{th} the focus distance was set to 160 m and a 15^{o} optical wedge was used.

4.3 The "Noise from wind turbines in wake" project

The EFP project "Noise from wind turbines in wake" [9] was carried out as a supplement to the DANAERO project. In this project the far field noise levels was measured by a parabolic measurement system (PMMS) and related to the surface pressure and inflow angles measured on different blade sections of the instrumented NM80 turbine (WT03) at the Tjæreborg Enge site.
During the campaign the PMMS measurements was synchronized using a trigger signal from the DANAERO measurements and one of the PMMS trigger channels.
A total of 65 far field noise measurement series were carried out during the project and they were distributed on the dates listed below:

- 16 July 2009 (22 measurement sessions)
- 14 August 2009 (4 measurement sessions)
- 1 September 2009 (28 measurement sessions)
- 11 September 2009 (11 measurement sessions)

4.4 Concurrency of related projects

Figures 4.2-4.3 show histograms of where the above described projects are running concurrently with the DANAERO project. There are a total of 174 parallel 10-minute recordings between the DANAERO and TOPFARM campaigns. The corresponding number of simultaneous 10 minute recordings of the DANAERO and the WindScanner project is 201. For completeness Figure 4.4 shows histograms of where the DANAERO project is running concurrently with both the TOPFARM and the WindScanner projects (the specific times for the wake noise project is not known).

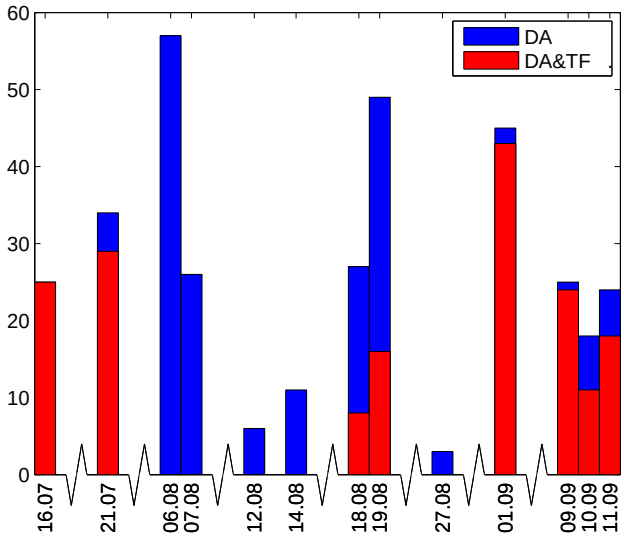

Figure 4.2. Distribution of available 10 minute recordings in the DANAERO (DA) project and where the DANAERO (DA) and TOPFARM (TF) campaigns are running in parallel.

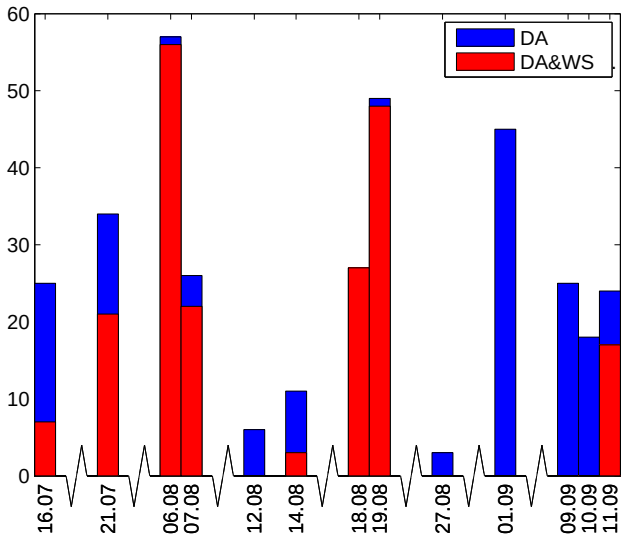

Figure 4.3. Distribution of available 10 minute recordings in the DANAERO (DA) project and where the DANAERO (DA) and WindScanner (WS) campaigns are running in parallel.

There are 62 recordings of 10 minute length where the three projects are running at the same time. However, it should be mentioned that even though there are several times where the project are running in parallel they may not be directly synchronized so some efforts may be needed to achieve this. Furthermore, the quality of the concurrent datasets have not yet been verified. Nevertheless, the cases where the three projects are running simultaneously could potentially provide knowledge of inflow, loads and wake conditions at the same time, which would make these datasets very extensive and unique.

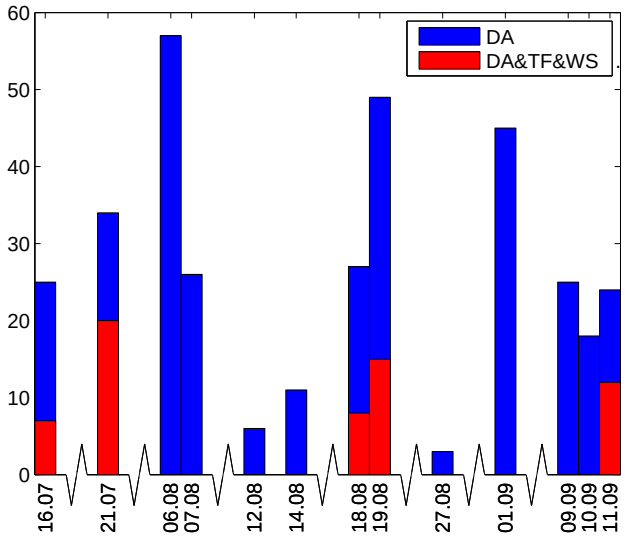

Figure 4.4. Distribution of available 10 minute recordings in the DANAERO (DA) project and where the DANAERO (DA), TOPFARM (TF) and WindScanner (WS) campaigns are running in parallel.

References

[1] TOPFARM - NEXT GENERATION DESIGN TOOL FOR OPTIMISATION OF WIND FARM TOPOLOGY AND OPERATION. Technical Report Risø-R-1805(EN), Technical University of Denmark, 2011.

[2] Database on wind characteristics. Internet wind database of wind field measurements, URL=http://www.winddata.com/.

[3] G.C. Larsen and K.S. Hansen. Full-scale measurements of aerodynamic induction in a rotor plane. *Torque, 2012, Oldenburg, Germany*, 2012.

[4] E. Machefaux. Wake analysis on full scale LiDAR based measurements. *internal document*, 2011.

[5] T. Mikkelsen, S. Knudsen, M. Sjöholm, N. Angelou, and A. Tegtmeier. WindScanner.eu - a new Remote Sensing Research Infrastructure for On- and Offshore Wind Energy. *To be published*, 2013.

[6] Windscanner.dk. URL=http://www.windscanner.dk/.

[7] N. Angelou, T. Mikkelsen, K.H. Hansen, M. Sjöholm, and M. Harris. LIDAR Wind Speed Measurements from a Rotating Spinner: "SpinnerEx 2009". *Risø-R-1741(EN)*, 2010.

[8] T. Mikkelsen, N. Angelou, K. Hansen, M. Sjöholm, M. Harris, C. Slinger, P. Hadley, R. Scullion, G. Ellis, and G. Vives. A spinner-integrated wind lidar for enhanced wind-turbine control. *Accepted for publication in Wind Energy*, 2013.

[9] D.M Madsen, B. Plovsing, T. Sørensen, H.Aa. Madsen, and F. Bertagnolio. EFP07-II noise emission from wind turbines in wake. Technical report, DELTA and Risø-DTU, 2011.

5 Calibration of data obtained in the Tjæreborg experiment

Author(s): N. Troldborg

One of the tasks in DANAERO MW II was to calibrate the sensors used during the experiment. As outlined in detail in [1] this turned out to be much more challenging than expected.
In most cases the complications arose from sensor failures caused by e.g. saturation of strain gauges, broken tube connections to the pressure taps or blocked holes in the Pitot tubes.
Even though a lot of efforts were made to maintain, clean and protect the measurements equipment during the experiment it is nearly impossible to avoid sensor failure when equipment are used in the field where it naturally is exposed to various external effects.
In other cases the calibration was challenging because some sensors drifted from their original calibration. An example is the strain gauges measuring edgewise bending moments which were affected by the blade temperature and hence needed to be recalibrated.
Finally, some sensors needed to be recalibrated because of human mistakes, e.g. misplacement of calibration sheets, wrong calibration coefficients provided by suppliers or small offsets in position of strain gauges.
The difficulty when sensors are to be recalibrated is that it must be based on measurements carried out during the campaign while the initial calibrations typically are carried out under controlled conditions. Fortunately, the experimental campaign was from the beginning designed with some degree of redundancy making it possible to calibrate one sensor using measurements from other sensors.
An example of a particularly challenging sensor to calibrate was the strain gauge measuring shaft torque. This sensor was calibrated by using the strain gauges measuring the edgewise bending moment distribution along the blade to compute the moment around the shaft. However, the measurements of these strain gauges were found both to depend on blade temperature and on the flapwise bending moment. Thus, the calibration of the shaft torque strain gauge relied on accurate calibration of the strain gauges measuring both edgewise and flapwise bending moments as well as blade temperature and should still be consistent with the measurements of electrical power.

References

[1] C. Bak, H.Aa. Madsen, N. Troldborg, M. Gaunaa, W. Skrzypiński, A. Fischer, U. Paulsen, R. Møller, P. Hansen, M. Rasmussen, and P. Fuglsang. DANAERO MW: Instrumentation of the NM80 2.3MW wind turbine including the LM 38.8 m blade and the meteorology mast at Tjæreborg . Technical Report Risø-I-3045(EN), Technical University of Denmark, 2013.

Part II: Analysis of data

6 Measured airfoil characteristics for a MW rotor in atmospheric conditions

Author(s): C. Bak, N. Troldborg, H.A. Madsen

This section is a shortened description of a paper presented by Bak et al. [1] and shows examples on pressure and inflow measurements carried out during the DAN-AERO MW project on both a full scale rotor and in a wind tunnel.

6.1 Experimental approach

In order to explain how the aerodynamic characteristics are on a real wind turbine and how 2D wind tunnel data should be transferred to 3D this investigation uses both full scale and wind tunnel experiments as a basis.
From the field experiment on the NM80 turbine the following sensors are used:

- 4×64 surface pressure taps at the four radial stations, r/R=0.325, 0.475, 0.750 and 0.925 of the LM38.8 blade.
- Four five-hole Pitot tubes mounted at r/R=0.36, 0.51, 0.78 and 0.90, respectively.
- Rotational speed of the rotor
- Air density (derived from temperature and pressure measurements)

From the measurements in the LM Wind Power wind tunnel the following sensors are used:

- 4×64 surface pressure taps on four aerofoils with nearly the same geometry as the four blade sections of the LM38.8 blade which were instrumented with pressure taps.

6.1.1 Predicting the angle of attack

The results from wind tunnel tests are commonly polars in terms of lift, drag and moment coefficients as a function of angle of attack. These data are used in aeroelastic calculations with corrections of e.g. 3D effects. In this way the rotor performance and the loads on the entire wind turbine can be predicted. However, the angle-of-attack term is an entity, which is not possible to measure directly on or at the blade. The bound circulation on the blade and the downwash are some of the effects influencing the flow around the blade sections. Thus, even though Pitot tubes are measuring the angle of attack, the measured angles are not corresponding to those measured in wind tunnels, because angles of attack in the tunnel are measured as the pitch angle of the airfoil with corrections of blockage, streamline curvature and downwash. The hypothesis in this analysis is that the pressure distributions corresponding to airfoil flow is similar in the wind tunnel and at the rotor. In this way transfer functions from angles of attack measured by the Pitot tubes and angles of attack measured in wind tunnels are established. In situations with attached flow it is expected that good agreement will be seen for all parts of the pressure distribution despite of the rotational effects. This is based on experience from 3D CFD calculations on several rotors. However, with separated flow a delay of the separation is expected based on observations from other experiments and therefore a good agreement is generally only expected on the pressure side and close to the trailing edge on the suction side. Therefore, angles of attack are estimated in an optimization process, where pressure distributions measured at the rotor are compared to pressure distributions measured in the wind tunnel, by minimizing the standard deviation of the pressure differences with higher weight from x/c=0.40 to x/c=1.00 at the pressure side and x/c=0.70 to x/c=1.00 at the suction side and lower weight on the rest of the airfoil.

However, in the analysis process it turned out that the inner section, Section 03 at r/R=0.325, needs special treatment. For each measured pressure distribution on the rotor similar distributions from the wind tunnel were searched for, but the agreement was far less pronounced than on the three other sections. Thus, another method for searching for the right pressure distributions was developed for the inner section. Since the dynamic pressure and the angle of attack were determined for the three outer sections, the corresponding inflow velocity can be predicted and good correlations between the inflow velocities for these sections are observed. This was the reason for assuming that the inflow velocity for the inner section, Section 03 at r/R=0.325, can be determined by extrapolating/regression of the inflow velocities from the outer sections.

6.2 Results

In the following, results from an analysis of a number of selected time series are shown.

6.2.1 Pressure distributions

Figure 6.1 shows pressure distributions corresponding to lowest and highest angles of attack extracted from these time series in comparison to wind tunnel data. The pressure distributions are normalized as:

$$C_p = \frac{p_\infty - p}{\frac{1}{2}\rho W^2}$$

Where C_p is the normalized pressure, p_∞ is the static pressure [Pa] in the far field, p is the pressure [Pa] measured at the blade surface, ρ is the air density $[kg/m^3]$ and W is the relative velocity [m/s]. For the three outboard sections the agreement is very good. For low angles of attack the pressure distributions are very similar and fit well both at the leading edge and trailing edge. However, at high angles of attack Section 05 (r/R=0.475) shows deviations between pressure distributions in the tunnel and on the rotor. The pressure recovery from minimum pressure to the trailing edge is not as abrupt on the rotor as in the tunnel. This could be caused by 3D effects on the rotor, but could also be the influence from the walls in the wind tunnel. This is yet unknown. However, for the inner section, Section 03 at r/R=0.325, the agreement is not so good. The pressure around the leading edge fits well, but the pressure around the trailing edge does not agree as well as for the three outer sections even at fairly low angles of attack. At higher angles of attack, as shown in Figure 6.1, the pressure distribution measured on the rotor is much bigger than from the wind tunnel and a nearly constant pressure level is reached at a chord position closer to the trailing edge at the rotor (x/c=0.44) compared to the wind tunnel data (x/c=0.38). This indicates the position of the separation point, which again indicates a delay in stall on the rotor compared to the wind tunnel.
To investigate the precision of this method to derive airfoil characteristics for the rotor Figure 6.2 compares the derived angles of attack and dynamic pressures, called "synthetic", to those measured by the Pitot tube in Section 05. There is a distinct trend, however with some scatter of data. This was the reason not to use the Pitot tube measurements directly and it indicates the degree of correlation between angles of attack and pressure distributions.

6.2.2 Integrated forces

Figure 6.3 shows the normal force coefficients c_n and Figure 6.4 shows the tangential force coefficient c_t integrated from the pressure distributions for the rotor and for wind tunnel flows both with clean surface and leading edge roughness (LER). The normal force coefficient, c_n,

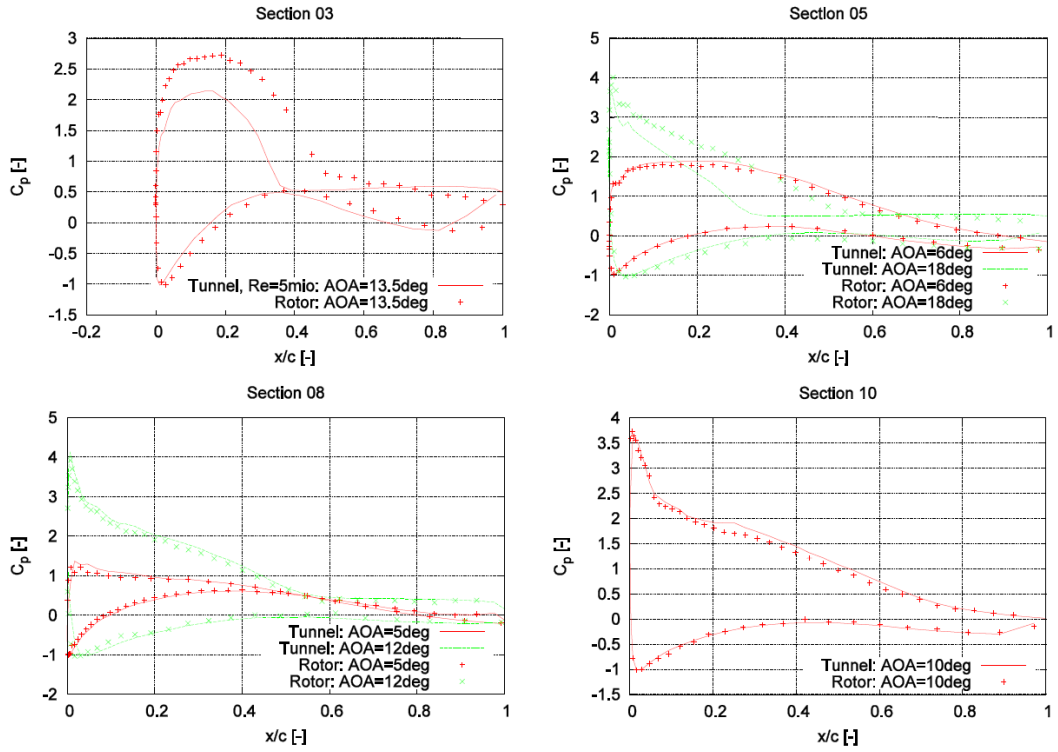

Figure 6.1. Pressure measurements for four different blade sections. Upper left: Section 03 (r/R=0.325). Upper right: Section 05 (r/R=0.475). Lower right: Section 08 (r/R=0.750). Lower left: Section 10 (r/R=0.925).

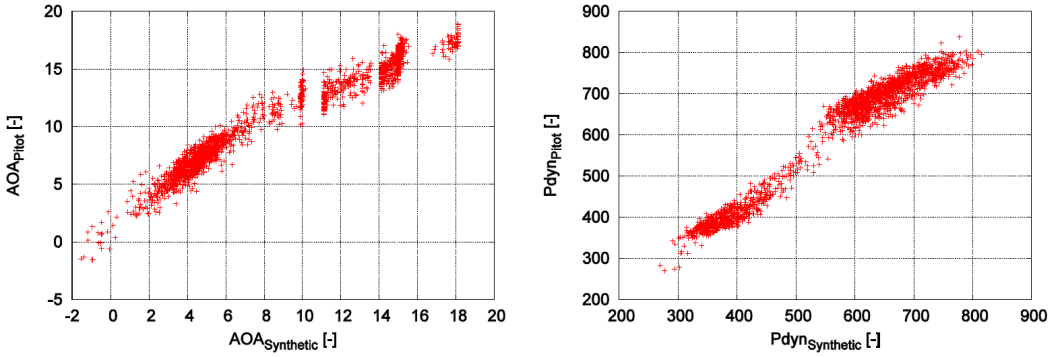

Figure 6.2. Angles of attack (left) and dynamic pressures (right) predicted by comparing pressure distributions from the rotor with pressure distributions from the wind tunnel ("synthetic") plotted against the angles of attack and dynamic pressures as measured by the Pitot tube in Section 05 ("Pitot"), respectively.

and the tangential force coefficient, c_t, were computed, respectively, as:

$$c_n = \frac{n}{\frac{1}{2}\rho W^2 c}$$

$$c_t = \frac{t}{\frac{1}{2}\rho W^2 c}$$

where n and t is the normal and tangential force per meter [N/m] , respectively, integrated from the C_p distributions, ρ is the air density $[kg/m^3]$, W is the relative velocity [m/s] and c is the chord length [m]. For the three outboard sections the agreement is very good for both

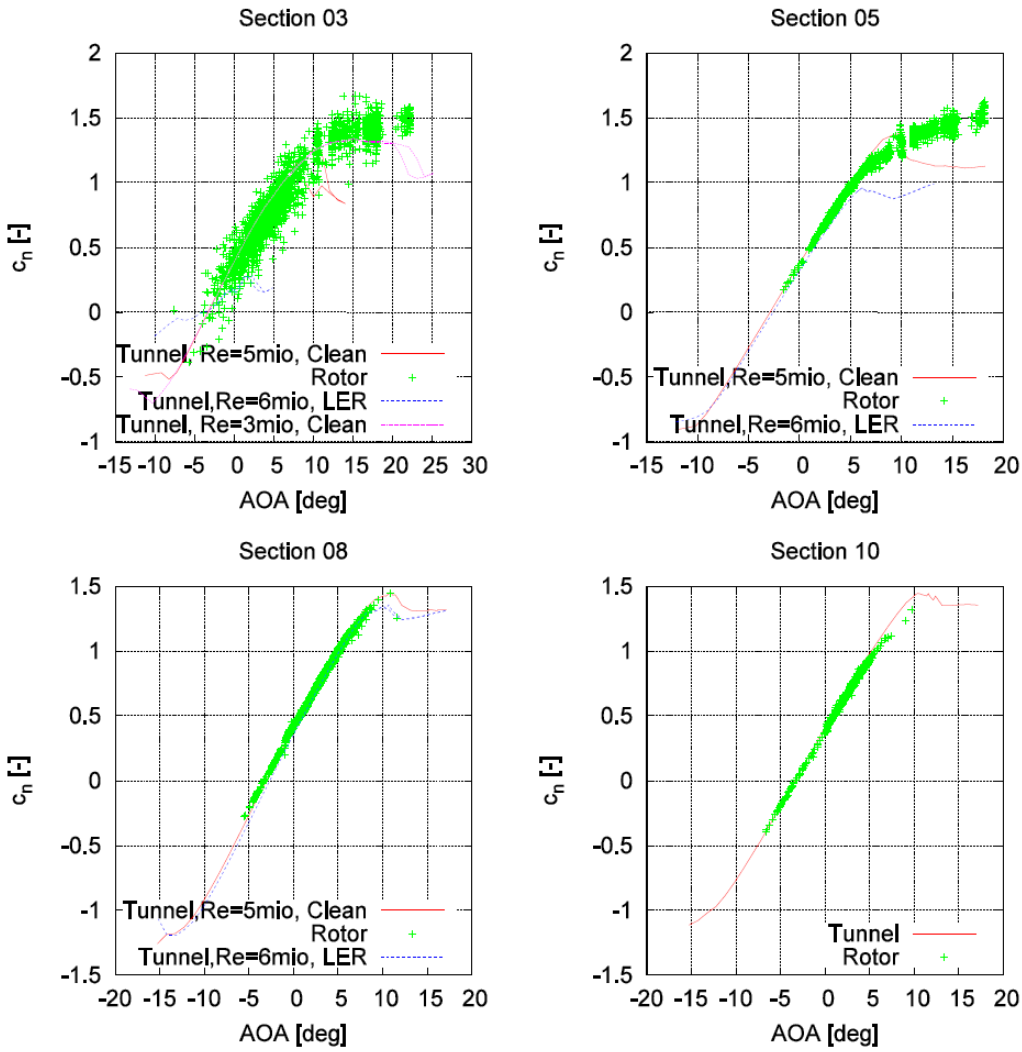

Figure 6.3. Measured c_n polars for four different blade sections. Upper left: Section 03 (r/R=0.325). Upper right: Section 05 (r/R=0.475). Lower right: Section 08 (r/R=0.750). Lower left: Section 10 (r/R=0.925).

c_n and c_t. However, it seems that comparing to maximum c_n for the clean wind tunnel model the rotor showed slightly lower c_n. This could be caused by surface roughness or differences in surface quality, i.e. the roughness height on the airfoil surface. More interesting, it seems that the decrease in c_n for angles of attack above maximum c_n observed in the characteristics from the wind tunnel is less pronounced on the rotor at Section 05 at r/R=0.475. This might be controlled by centrifugal/Coriolis forces or controlled by the lack of walls around the airfoil section. For the inner section, Section 03 at r/R=0.325, the agreement is good, but not as good as the other sections with higher scatter in the values even at low angles of attack. This is due to the method used, where the inflow velocity found by extrapolation/regression of the inflow velocities measured at the outer sections and where angles of attack are not determined by comparison of pressure distributions. At high angles of attack the c_n values in stall are higher than in the wind tunnel which indicates that the separation is delayed like for Section 05. It should be noted that the plot of c_n shows wind tunnel data at two Reynolds numbers, $Re = 3 \times 10^6$ and $Re = 5 \times 10^6$. The data is different in stall, with low Re c_n higher than the high Re c_n. The increase of c_n in stall supports earlier observations of higher c_n values when separation starts.

Figure 6.5 shows c_n polars for the two blade sections at the inner part of the rotor, compared to polars derived from wind tunnel tests corrected for 3D effects using the model by Bak et al.

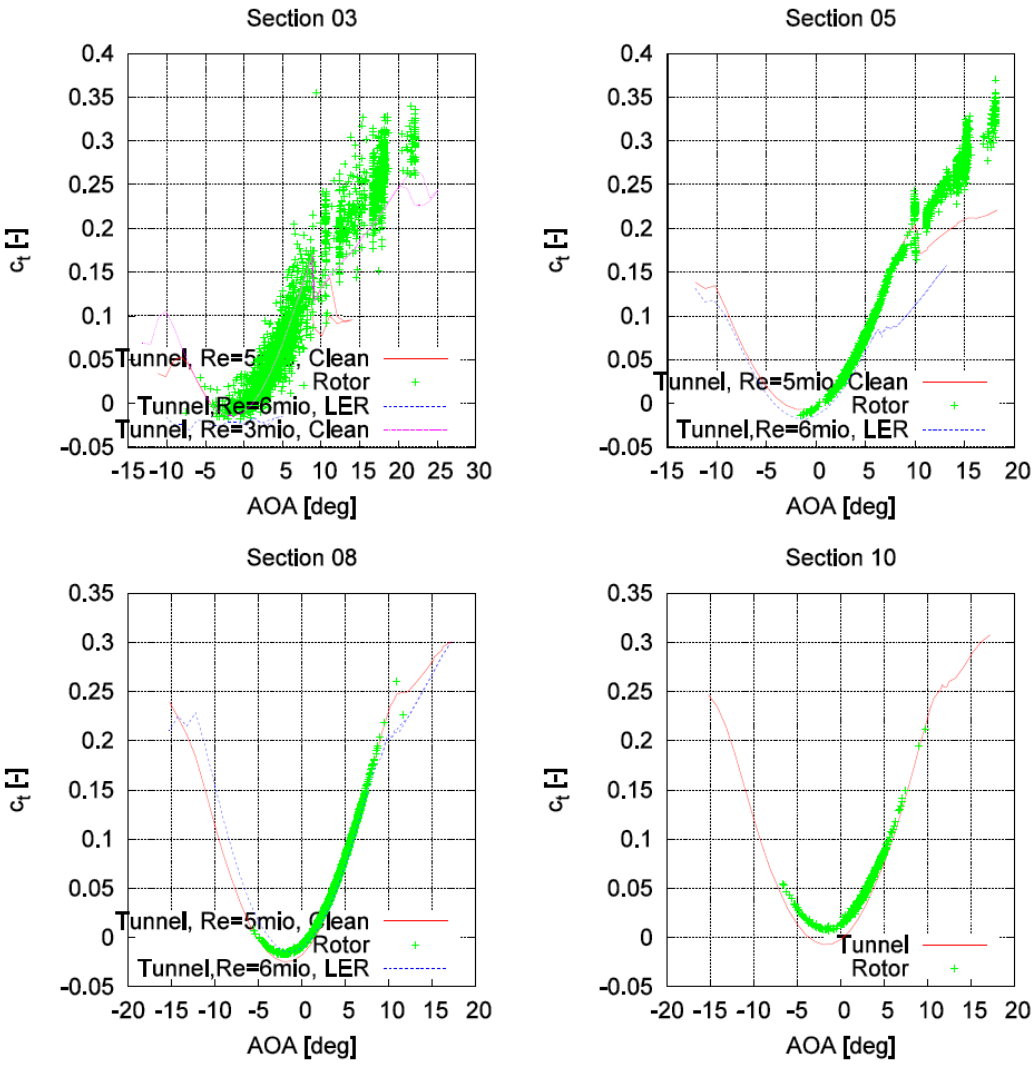

Figure 6.4. Measured c_t polars for four different blade sections. Upper left: Section 03 (r/R=0.325). Upper right: Section 05 (r/R=0.475). Lower right: Section 08 (r/R=0.750). Lower left: Section 10 (r/R=0.925).

[2].

Only the two inner sections are considered because it is only those that are significantly affected by the 3D correction model. However, it seems that the drop in c_n for angles of attack just above maximum c_n still exists despite of the 3D correction. With the given wind tunnel data in Section 03 and 05 it seems that the 3D correction is too small compared to the actual data from the rotor. However, this is mainly due to the drop in c_n just after maximum c_n.

6.3 Conclusion

This paper showed examples on pressure and inflow measurements carried out in the DAN-AERO MW project on both a full scale rotor and in a wind tunnel. Wind tunnel tests in the LM Wind Power LSWT on four airfoil sections identical to the blade sections on the LM38.8 blade were carried out. Also, measurements on an NM80 2MW wind turbine were carried out, including pressure measurements in four sections, inflow measured with four Pitot tubes and several other sensors, such as strain gauges, accelerometers and those controlling the turbine. The pressure measurements as well as the integrated normal force and tangential force coef-

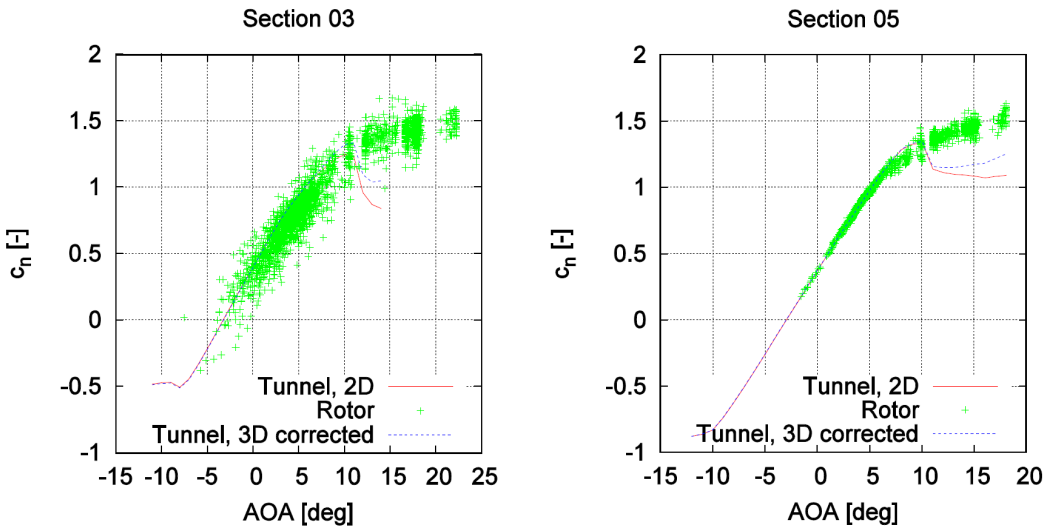

Figure 6.5. Measured c_n polars for two different blade sections compared to 3D corrected wind tunnel data using the method by Bak et al [2]. Left: Section 03 (r/R=0.325). Right: Section 05 (r/R=0.475).

ficients, c_n and c_t, revealing the airfoil performance from the full scale rotor in atmospheric conditions and the airfoil performance in the wind tunnel are compared to reflect the differences and compare to models for 3D correction. A general trend is that the negative slope of the c_n curve just above angles of attack corresponding to maximum c_n as measured in wind tunnels is not as pronounced at the rotor. Whether this is due to 3D effects or the lack of walls around the section on the rotor is not known. Also, delay of separation was observed, especially for the inner section, which caused an increase in c_n for angles of attack above maximum c_n as measured in the wind tunnel. However, 3D correction of wind tunnel data showed for these measurements too abrupt decrease in the forces for angles of attack just above the maximum normal force coefficient as measured in the tunnel.

References

[1] C. Bak, N. Troldborg, and H.A. Madsen. DAN-AERO MW: Measured airfoil characteristics for a MW rotor in atmospheric conditions. *EWEA, Brussels, Belgium*, 2011.

[2] C. Bak, J. Johansen, and P.B. Andersen. Three-Dimensional Corrections of Airfoil Characteristics Based on Pressure Distributions. *European Wind Energy Conference, Athens*, 2006.

7 Detection of transition on airfoils from high frequency microphone measurements

Author(s): M. Døssing, H.A. Madsen, C. Bak, A. Fischer, N. Troldborg, P. Hansen, F. Bertagnolio

This chapter presents a method which uses high frequency surface microphone measurements to detect transition from laminar to turbulent boundary layer flow on a full scale wind turbine blade. The chapter is a shorter version of the report by Døssing et al. [1].

7.1 Introduction

The chordwise position of the transition from laminar to turbulent boundary layer flow is a key parameter in both experimental and computational aerodynamics as well as in airfoil design. Previous work carried out in wind tunnels have shown that high frequency surface pressure measurements is an efficient way of detecting transition [2–4]. Figure 7.1 shows an example of

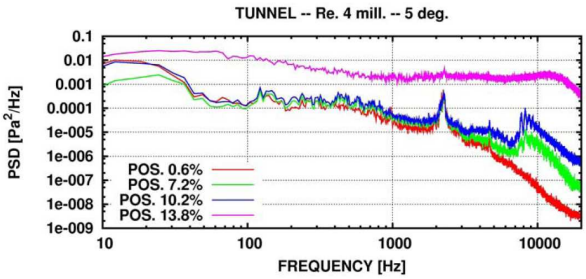

Figure 7.1. Power spectrum of surface pressure from four microphones in the leading edge region of an airfoil in a wind tunnel. Transition is detected to be between position 10.2% from the leading edge and position 13.8%.

a surface pressure power spectrum measured by four microphones in the leading edge region of an airfoil in a wind tunnel. The figure is taken from work by Madsen et al. [4]. As seen the spectrum for the microphone at position 13.8% from the leading edge is much higher than the spectrum for the microphone at position 10.2%. So, the transition has been detected to be within these two positions. In the wind tunnel measurements on airfoils by Bak and Døssing [2] and Døssing [3] transition was identified as the chordwise position with an increase in the quantity μ_l defined as:

$$\mu_l = \frac{\int_0^{f_{ny}} f P_{sp} df}{\int_0^{f_{ny}} P_{sp} df} \tag{1}$$

where f_{ny} is the Nyquist frequency and P_{sp} the power spectrum of the surface pressure. This definition of μ_l means that the energy at high frequencies are weighted higher than the energy at low frequencies.
This approach does however not work in the DANAERO field experiment because the low frequency part of the power spectrum dominates. Therefore, the method proposed here is to use microphones to measure the sound pressure level (SPL) in a given frequency band and infer transition as locations with a sudden chordwise increase of the SPL.

7.2 Measurement data

The used measurements are obtained in the part of the DANAERO MW project where a 2MW NM80 wind turbine and a nearby met mast located at the Tjæreborg site near Esbjerg, Denmark was extensively instrumented to facilitate inflow and load measurements on the turbine. As part of the instrumentation of the blade of the NM80 turbine 50 high frequency microphones measuring surface pressure fluctuations at 50 kHz was installed at a position 3 m from the tip. See [5] for further details.

7.3 Method

As mentioned in the introduction the method proposed here is to detect transition as positions with a chordwise increase in the sound pressure level L_p.

7.3.1 Computing the sound pressure level

The sound pressure level L_p at each of the 50 microphone positions is computed from the power spectral density of the surface pressure, P_{sp} as follows

$$L_p = 20\log_{10}\left(\frac{P_{rms}}{p_{ref}}\right) \tag{2}$$

where $p_{ref} = 20\mu Pa$ and

$$P_{rms}^2 = 2\int_{f_1}^{f_2} P_{sp}(f)df \tag{3}$$

where $f_1 \leq f \leq f_2$ is a given frequency range. The influence of f_1 and f_2 on the sound pressure level is studied in section 7.4.
In order to derive temporal variations in the transition point each time series of surface pressure measurements are divided into K sections (windows) with a 50% overlap and for each of these windows L_p is computed from equation 2 and 3. To each of the K windows is then associated a sound pressure level $L_{p,k}$ and a discrete time t_k, which is taken to be at the center of the window. In the present work the method described by Welch [6] is used to make the Fourier analysis needed to compute P_{sp} and a Hanning window function is applied to each window section. More details about the procedure can be found in [1]. The number of surface pressure samples in each window is denoted L, which is equivalent to a time span of $\Delta t = L/f_s$, where $f_s = 50\ kHz$ is the sampling frequency.

7.3.2 Detection of transition

The transition point at each discrete time step t_k is determined from the chordwise distribution of the sound pressure level, L_p in the following way:

- Sort L_p according to chordwise position, x, of the 50 microphones.
- Filter spatially L_p to obtain a smooth distribution denoted $L_p(x)$.
- Determine transition points, x_t, as positions where the chordwise derivative of $L_p(x)$ is larger than a specified limit $(dL_p(x)/dx)_{limit}$.
- In general there will be a range of chordwise positions which fulfils this criteria and the exact position is defined to be the zero crossing of the second order derivative $d^2L_p(x)/dx^2$.

- If more than two chordwise positions on each side of the airfoil satisfy the criteria then $(dL_p(x)/dx)_{limit}$ is increased until only two transition points are found on each side of the airfoil.

Figure 7.2 shows an example of calculated transition points together with the corresponding sound pressure level and its first and second derivative. The parameters used in Figure 7.2 are

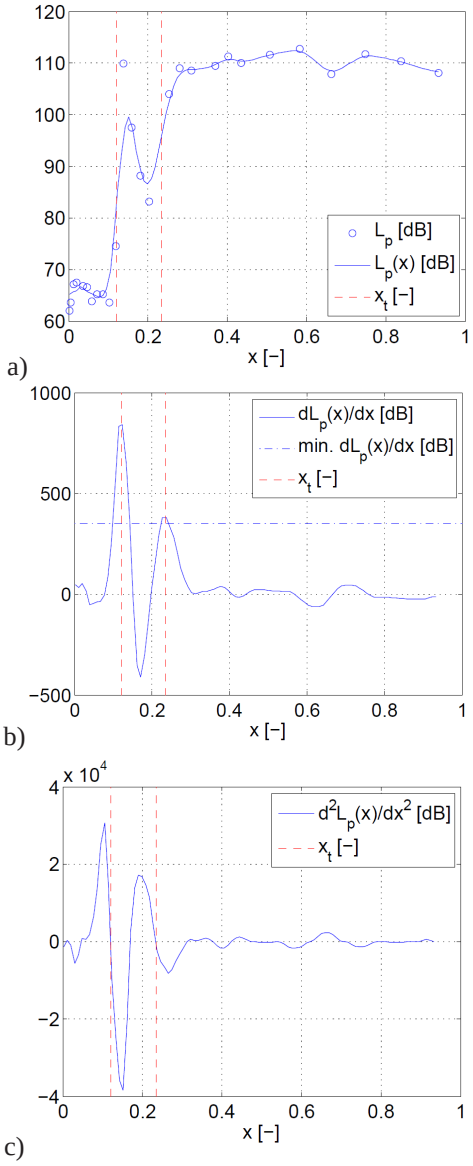

Figure 7.2. Example of calculated transition points on suctions side at a given time t_k and the corresponding SPL (a) as well as its derivative (b) and second derivative (c)

shown in Table 7.1.

$(dL_p(x)/dx)_{limit}$	350 dB
f_1	2.0 kHz
f_2	6.0 kHz
L	2048

Table 7.1. Key parameters for detection of transition

7.4 Parameter study

In this section the influence of various parameters on the prediction of the transition point on the suction side is investigated. The parameter study includes the following parameters:

- Window size, L
- Frequency range, $f_1 \leq f \leq f_2$
- Limit on derivative of L_p, $(dL_p(x)/dx)_{limit}$

The measurements used for the parameter study was obtained on july 21^{st} and is located in the data file *cRIO_20090721_144710.tim*.

7.4.1 Dependency on window size

Figure 7.3 shows contour plot of L_p versus t_k and x for various window sizes, L. In all plots L_p has been computed using $f_1 = 1kHz$, $f_2 = 6kHz$ and $(dL_p(x)/dx)_{limit} = 350dB$. The plots are converging when L is decreased and there is only small differences when L is less than approximately 2048.

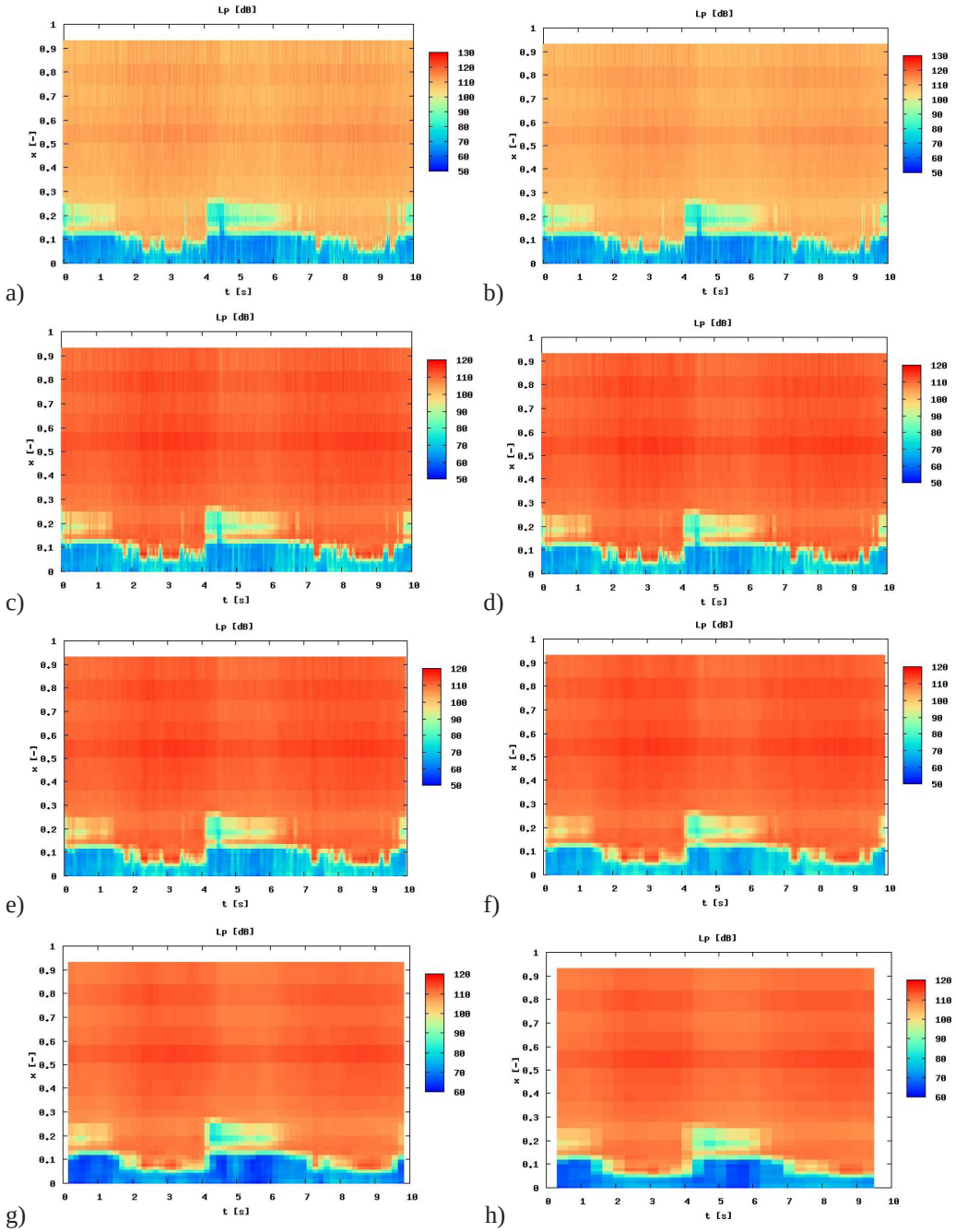

Figure 7.3. Contours of L_p as function of chordwise position and time. $f_1 = 1.0\ kHz$, $f_2 = 6.0\ kHz$ and $(dL_p(x)/dx)_{limit} = 350\ dB$. a) $L = 256$; b) $L = 512$; c) $L = 1024$; d) $L = 2048$; e) $L = 4096$; f) $L = 8192$; g) $L = 16384$; h) $L = 32768$

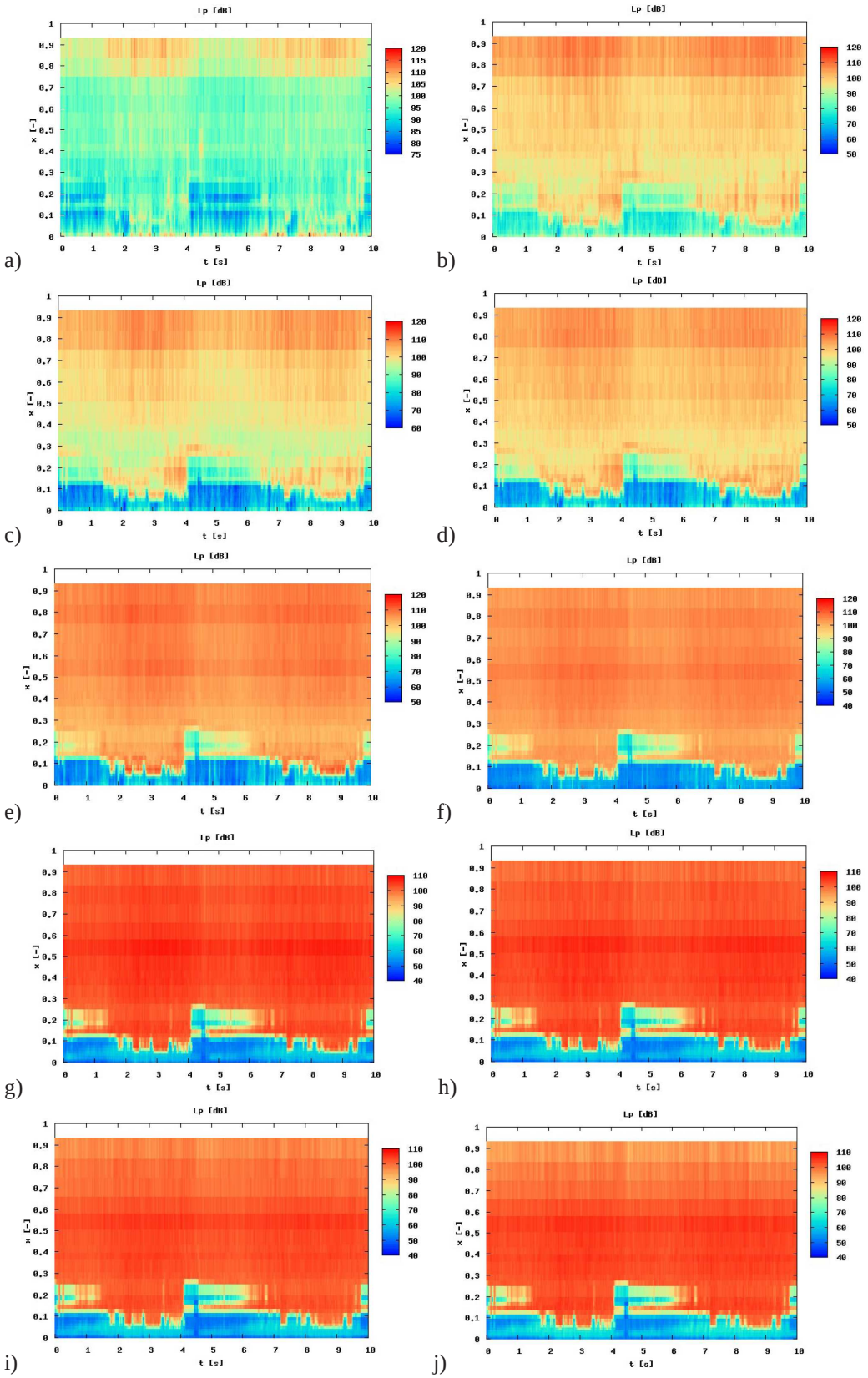

Figure 7.4. Contours of L_p as function of chordwise position and time. In all cases $L = 2048$ and $(dL_p(x)/dx)_{limit} = 350dB$. The frequency range (f_1, f_2) is (in [Hz]): a) $(100,300)$, b) $(300,500)$; c) $(500,750)$; d) $(750,1000)$; e) $(1000,2000)$; f) $(2000,3000)$; g) $(3000,4000)$; h) $(4000,5000)$; i) $(5000,6000)$; j) $(6000,7000)$

7.4.2 Dependency on frequency range

Figure 7.4 shows contour plot of L_p versus t_k and x for various frequency ranges. In all plots $L = 2048$ and $(dL_p(x)/dx)_{limit} = 350dB$.
The plots show that the chordwise distribution of the sound pressure level based on low frequencies differs substantially to the corresponding values at higher frequencies.

7.4.3 Dependency on $(dL_p(x)/dx)_{limit}$

Figure 7.5 shows contour plots of L_p versus t_k and x for $L = 2048$, $f_1 = 2kHz$ and $f_2 = 6kHz$. Also included in the plots are the predictions of the transition points x_t using various values of $(dL_p(x)/dx)_{limit}$.

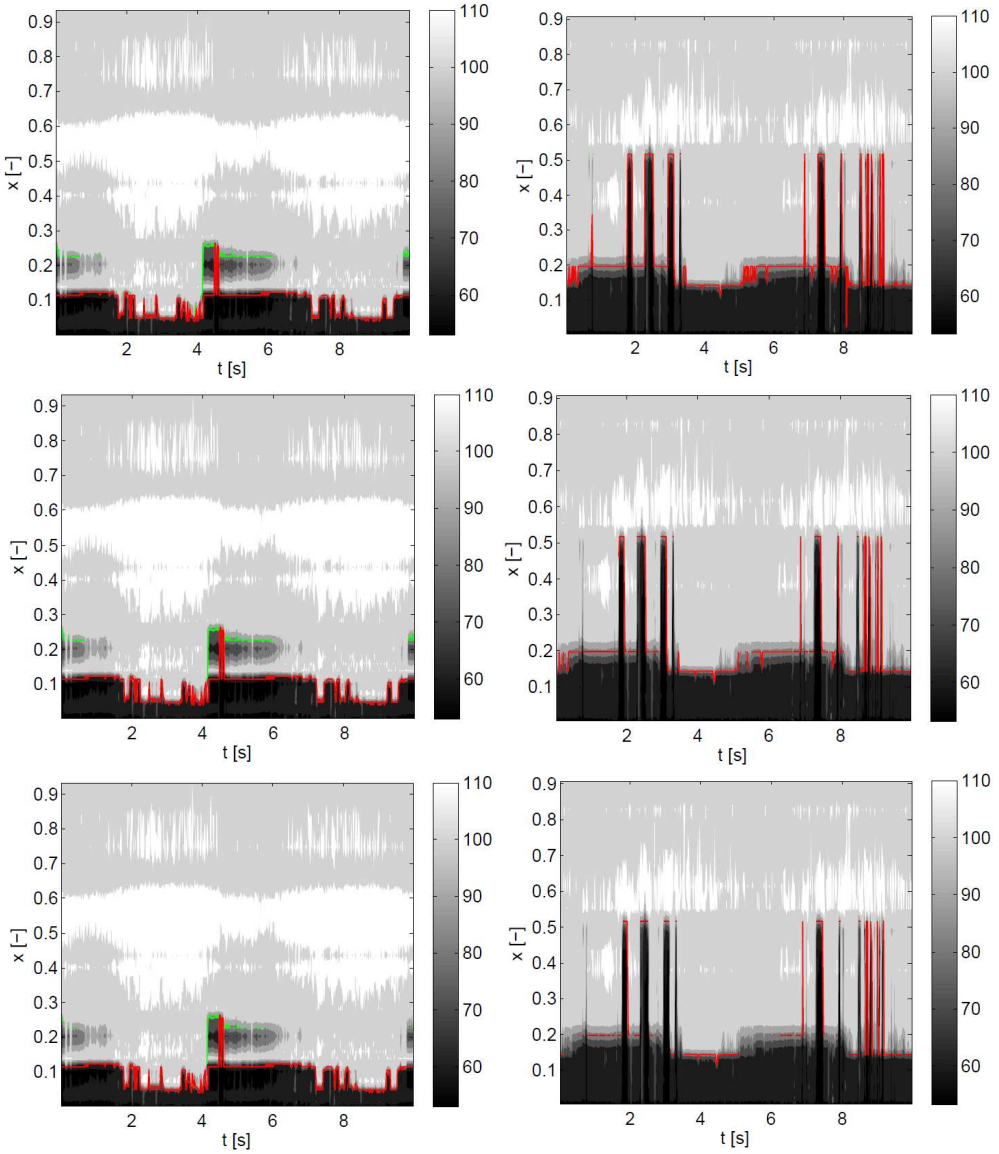

Figure 7.5. Contours of SPL as function of chordwise position and time together with predictions of transition points for various values of $(dL_p(x)/dx)_{limit}$. In all cases $L = 2048$, $f_1 = 2.0\ kHz$ and $f_2 = 6.0\ kHz$). Left: Suction side; Right: Pressure side. Top: $(dL_p(x)/dx)_{limit} = 300\ dB$; Middle: $(dL_p(x)/dx)_{limit} = 400\ dB$; Bottom: $(dL_p(x)/dx)_{limit} = 500\ dB$.

Note that x denotes the chordwise position scaled with the chord of the airfoil section, i.e. $0 \leq x \leq 1$. The red curve shows the first transition point and the green curve shows the second transition point. The first transition point (red) has the largest derivative $dL_p(x)/dx$. The aim of the analysis is to determine a value of $(dL_p(x)/dx)_{limit}$ which gives numerically stable detections of the transition points. Choosing $min(dL_p(x)/dx)$ to be between 300 dB and 400 dB gives good predictions of the transition points in the shown case. Therefore, $(dL_p(x)/dx)_{limit} =$ 350 dB was selected for the full analysis of all data.

7.5 Results

In section 7.4 we saw that it is possible to use small data windows and thereby analyse the time variations of L_p in the boundary layer and hence also the dynamics of the transition points.

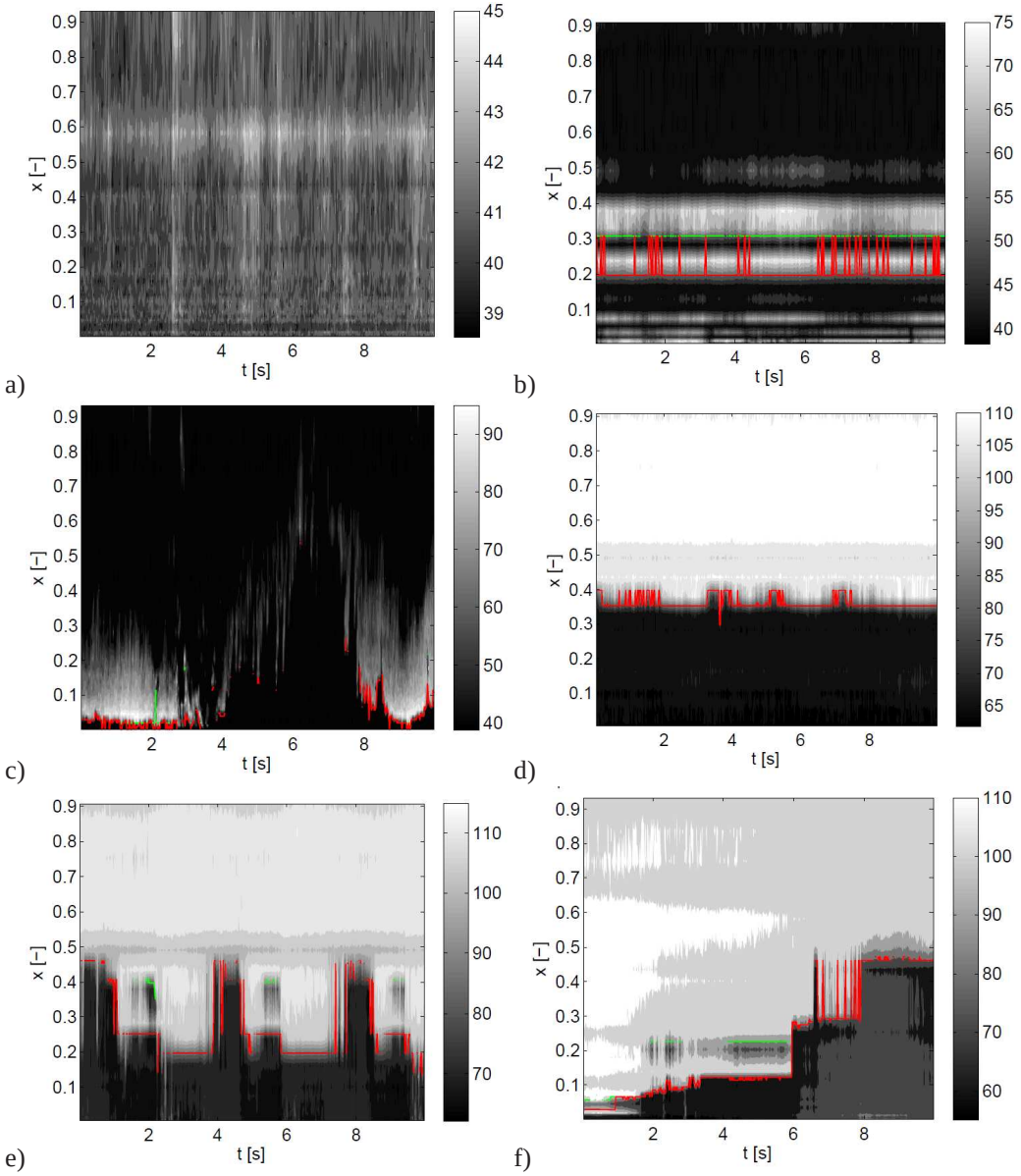

Figure 7.6. Various representative examples of contours of SPL on suction side versus chordwise position and time together with predictions of transition points. In all cases $L = 2048$, $f_1 = 2000kHz$, $f_2 = 6000Hz$) and $(dL_p(x)/dx)_{limit} = 350\ dB$

Figure 7.5 already indicates that the method used for identifying the transition point is robust and accurate. To further verify the method Figure 7.6 show contours of sound pressure level on the suction side in different cases together with the predictions of the corresponding transition points using the parameters in Table 7.1. In cases where the turbine is in operation i.e. where the L_p levels are not too low the proposed method is generally successful in detecting the transition point. Figure 7.6d reveal a case with nearly steady transition from laminar to turbulent boundary layer, Figure 7.6e show periodic variations with transition and relamination zones corresponding to the rotational speed of the turbine, while Figure 7.6f show a non-periodic behaviour. However, as indicated in Figure 7.6b), the method may fail in cases with low values of L_p where the turbine is at standstill or rotates very slowly. Based on the plots in Figure 7.6 the SPL can roughly be divided into the following regimes when using the parameters in Table 7.1:

- **0 - 60 dB** Turbine at standstill and background noise
- **60 - 85 dB** Laminar boundary layer
- **85 - 95 dB** Transition
- **95 - 120 dB** Turbulent boundary layer

The proposed technique for identifying transition points have been applied with the parameters in Table 7.1 to all microphone data obtained in the Tjæreborg experiment and are available in appendix reports [7–12]. The resulting chordwise positions of the transition points on both the suction and pressure side are available in the database.

7.6 Conclusions

The calculated sound pressure (SPL) level is converging when the size of the data window is decreased. In practice a window of 2048 data points yields converged data and corresponds to a sampling time of 0.041 seconds.
A frequency range of 2000-6000 Hz was found useful for detection of transition. The approximate SPL associated with standstill, laminar, transitional and turbulent flow has been identified. Transition was detected by enforcing a minimum derivative of SPL of 350 dB i.e. a 35 dB increase over 10% of the chord. This yielded good results in most cases, however transition was erroneously detected in a few special cases. The analysis has resulted in appendix reports [7–12], which contains results for each file sampled in the period from June 25^{th} to Semptember 11^{th}. These contains plots which gives an indication of the time varying properties in the boundary layer on the suction and pressure side.

References

[1] M. Døssing, H.A. Madsen, C. Bak, A. Fischer, N. Troldborg, P. Hansen, and Bertagnolio F. High frequency microphone measurements for detection of transition on airfoils. Technical Report Risø-I-3177(EN), Risø-DTU, Roskilde, Denmark, 2011.

[2] Research in Aeroelasticity EFP-2007. Technical Report Risø-R-1649(EN), RisøNational Laboratory, Technical University of Denmark, 2008.

[3] M. Døssing. High Frequency Microphone Measurements for Transition Detection on Airfoils. Technical Report Risø-R-1645(EN), Risø-DTU, Roskilde, Denmark, 2008.

[4] H.Aa. Madsen, C. Bak, U.S. Paulsen, M. Gaunaa, P. Fuglsang, J. Romblad, N.A. Olesen, P. Enevoldsen, J. Laursen, and L. Jensen. The DAN-AERO MW Experiments Final report. Technical Report Risø-R-1726(EN), Technical University of Denmark, 2010.

[5] C. Bak, H.Aa. Madsen, N. Troldborg, M. Gaunaa, W. Skrzypiński, A. Fischer, U. Paulsen, R. Møller, P. Hansen, M. Rasmussen, and P. Fuglsang. DANAERO MW: Instrumentation of the NM80 turbine and meteorology mast at Tjæreborg . Technical Report DTU Wind Energy Report-I-0083, Technical University of Denmark, 2013.

[6] P.D. Welch. The use of fast Fourier transform for the estimation of power spectra: A method based on time averaging over short, modified periodograms. *IEEE Trans. Audio and Electroacoust.*, AU-15:70–73, 1967.

[7] M. Døssing, H.A. Madsen, C. Bak, A. Fischer, N. Troldborg, P. Hansen, and Bertagnolio F. DAN-AERO MW II: High frequency microphone measurements for detection of transition on airfoils. Appendix report 20090625-20090716. Technical Report Risø-I-3178(EN), Risø-DTU, Roskilde, Denmark, 2011.

[8] M. Døssing, H.A. Madsen, C. Bak, A. Fischer, N. Troldborg, P. Hansen, and Bertagnolio F. DAN-AERO MW II: High frequency microphone measurements for detection of transition on airfoils. Appendix report 20090721-20090806. Technical Report Risø-I-3179(EN), Risø-DTU, Roskilde, Denmark, 2011.

[9] M. Døssing, H.A. Madsen, C. Bak, A. Fischer, N. Troldborg, P. Hansen, and Bertagnolio F. DAN-AERO MW II: High frequency microphone measurements for detection of transition on airfoils. Appendix report 20090807-20090818. Technical Report Risø-I-3180(EN), Risø-DTU, Roskilde, Denmark, 2011.

[10] M. Døssing, H.A. Madsen, C. Bak, A. Fischer, N. Troldborg, P. Hansen, and Bertagnolio F. DAN-AERO MW II: High frequency microphone measurements for detection of transition on airfoils. Appendix report 20090819. Technical Report Risø-I-3181(EN), Risø-DTU, Roskilde, Denmark, 2011.

[11] M. Døssing, H.A. Madsen, C. Bak, A. Fischer, N. Troldborg, P. Hansen, and Bertagnolio F. DAN-AERO MW II: High frequency microphone measurements for detection of transition on airfoils. Appendix report 20090827-20090901. Technical Report Risø-I-3182(EN), Risø-DTU, Roskilde, Denmark, 2011.

[12] M. Døssing, H.A. Madsen, C. Bak, A. Fischer, N. Troldborg, P. Hansen, and Bertagnolio F. DAN-AERO MW II: High frequency microphone measurements for detection of transition on airfoils. Appendix report 20090909-20090911. Technical Report Risø-I-3183(EN), Risø-DTU, Roskilde, Denmark, 2011.

8 Comparisons of airfoil characteristics for two airfoils tested in three different wind tunnels

Author(s): C. Bak, P. Fuglsang, J. Romblad, P. Enevoldsen, L. Jensen

In this work comparisons are carried out between the commonly used NACA 63_3-418 airfoil [1] and the wind turbine dedicated high lift airfoil Risø-B1-18 [2] measured in the three different wind tunnels:

- The VELUX wind tunnel (DK)
- The LM Wind Power Low Speed Wind Tunnel (LSWT) (DK)
- The Delft Low Speed Low Turbulence (LSLT) tunnel (NL)

For the NACA 63_3-418 airfoil additionally available data from the Stuttgart LWK (GER) and the Langley LTPT (USA) were shown in the comparison of the data.
Key values for the different wind tunnel layouts are related to the test results.

8.1 Experimental setup and approach

Two different airfoil designs were tested:
The commonly used NACA 63_3-418 airfoil designed for airplanes and the wind turbine dedicated high lift airfoil Risø-B1-18. One NACA 63_3-418 airfoil model and one Risø-B1-18 airfoil model with chord length 0.600 *m* were used in both the VELUX tunnel and the Delft tunnel. For the LM Wind Power tunnel new models were manufactured with a chord length of 0.900 *m*.
Tests were carried out at $Re = 1.5 \times 10^6$ and $Re = 1.6 \times 10^6$. For the Delft and LM tunnel $Re = 3 \times 10^6$ was also tested. Different configurations were tested such as clean surface and leading edge roughness in terms of zigzag tape at the leading edge.

8.2 The airfoils

NACA 63_3-418

The NACA 63_3-418 airfoil is described by Abbott and Doenhoff [1] and is designed for use on airplanes. However, it has been extensively used in the wind turbine industry for a few decades, because of the relatively smooth stall characteristics, the relatively high insensitivity of maximum lift to leading edge roughness, the quite good aerodynamic performance and the good structural characteristics. The intended use for airplanes causes the maximum lift- drag ratio to appear at a rather low lift coefficient (cl 0.9) and with a medium maximum lift coefficient ($c_{l,max} \approx 1.3$ for Reynolds numbers between 1.5 and 3×10^6).

Risø-B1-18

The Risø-B1-18 airfoil is described by Fuglsang and Bak [2] and is designed for wind turbines and specifically for those with Pitch Regulation and Variable rotor Speed (PRVS). For this type of regulation, stall is to a great extent avoided and the stall characteristics require less consideration. The airfoil is designed to be insensitive of maximum lift to leading edge roughness, to have high maximum lift ($c_{l,max} \approx 1.6$) and to show maximum lift-drag ratio at a quite high lift coefficient ($c_l \approx 1.3$ for Reynolds numbers between 1.5 and 3×10^6). The two airfoil contours are shown in Figure 8.1.

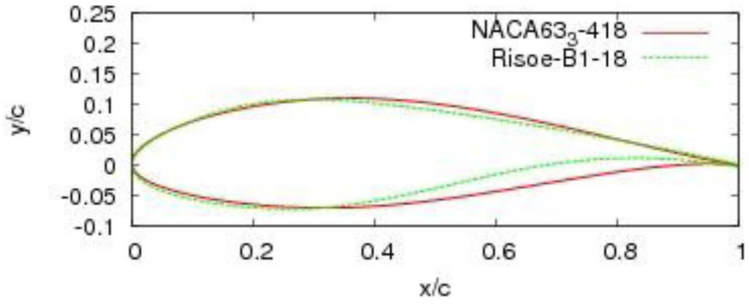

Figure 8.1. The NACA 63_3-418 and Risø-B1-18 airfoil contours

8.3 The leading edge roughness

With the requirement of 20 years wind turbine operation it is unavoidable that the blades surface condition will vary especially at the leading edge. The surface will change either because of contamination caused by dust and bugs sticking to the surface or by erosion. Thus, apart from testing airfoils with a clean surface, also leading edge roughness (LER) should be simulated in wind tunnel tests. However, there is still no consensus of how to do it. In this work four different types of roughness were used:

- Zigzag tape mounted at $x/c = 0.05$ at the suction side and at $x/c = 0.10$ at the pressure side with a tape thickness of 0.4 *mm*, a tape width of 3 *mm* and a tape pattern of 90^o.
- Zigzag tape mounted at $x/c = 0.02$ at the suction side with a tape thickness of 0.4 *mm*, a tape width of 3 *mm* and a tape pattern of 90^o.
- Zigzag tape mounted at $x/c = 0.05$ at the suction side and at $x/c = 0.10$ at the pressure side with a tape thickness of 0.4 *mm*, a tape width of 3 *mm* and a tape pattern of 60^o.
- Sandpaper 3M Safety-Walk of width $0.15m$ (6 inches) wrapped around the leading edge covering the entire airfoil from the leading edge to $x/c = 0.08$ on both pressure and suction side.

Only the first type of simulation was used in all the tunnels, whereas the second was used only in the LM LSWT and the third and fourth were used in the Delft tunnel. In this paper only the results from the first roughness simulation type will be compared. With a constant thickness of the zigzag tape in all the tunnels, the relative thickness in the LM tunnel was $t/c = 4.4 \times 10^{-4}$ and 50% higher in the LM and Delft tunnels, $t/c = 6.7 \times 10^{-4}$

8.4 The tunnels

Below the three wind tunnels are described. However, also the Stuttgart LWK and the NASA Langley LTPT are described because measured characteristics for the NACA 63_3-418 airfoil from these tunnels are also shown here. In all wind tunnels the drag was measured using a wake rake (an arrangement of parallel total pressure tubes in the wake of the airfoil). Thus, the pressure distribution (or the pressure/velocity deficit) in the wake of the airfoil is measured and converted to a drag coefficient.

VELUX wind tunnel

This wind tunnel is situated in Østbirk, Denmark, is owned by the roof top window manufacturer VELUX and is of the closed return type. The test section is open and the turbulence intensity is relatively high, TI=1%. The airfoil forces are measured using pressure taps in the

airfoil surface and the drag is measured using a fixed wake rake. The distributed pressure measurements are integrated to lift, drag and moment coefficients. The forces are corrected with respect to down wash and stream line curvature, see Ref. [3]. The test stand is mobile and owned by Risø DTU, so the measurements are carried out in campaigns over three to four days. The tunnel has been used by Risø DTU since the start of the 1990s. The dimensions of the tunnel are seen in Table 8.1.

LM Wind Power LSWT

This wind tunnel is situated in Lunderskov, Denmark, is owned by LM Wind Power and is of the closed return type. The test section is closed and the turbulence intensity is relatively low, TI=0.1%. The airfoil forces are measured using airfoil surface pressure taps and the drag is measured using a traversing wake rake. The distributed pressure measurements are integrated to lift, drag and moment coefficients and corrected according to Fuglsang and Bove [4]. The tunnel has been active since 2006. The dimensions of the tunnel are seen in Table 8.1.

The Delft LSLT

This Low Speed Low Turbulence (LSLT) wind tunnel is situated in Delft, The Netherlands, at Delft University of Technology. It is of the closed return type and the test section is closed. The turbulence intensity is very low, TI=0.02%. The airfoil forces are measured using the same principles as in the LM tunnel and lift, drag and moment coefficients are integrated and corrected according to the method described by Timmer [5]. The dimensions of the tunnel are seen in Table 8.1.

The Stuttgart LWK

This Stuttgart Laminar Windkanal (LWK) was not part of the general comparisons, but was used because one of the two airfoils was measured in the tunnel. It is situated in Stuttgart, Germany, at Stuttgart University and is of the open type and the test section is closed. The turbulence intensity is extremely low, TI=0.0002%. The airfoil forces are measured using pressure taps on the wind tunnel walls and the drag is measured using a traversing wake rake. The distributed pressure measurements are integrated to lift and drag coefficients and corrected, see Althaus [6]. The dimensions of the tunnel are seen in Table 8.1.

The NASA Langley LTPT

As for the Stuttgart wind tunnel, this tunnel was not part of the general comparisons, but was used because one of the airfoils was measured at one Reynolds number. It is situated in Hampton, Virginia, USA, at the NASA Langley Research Center and is a Low Turbulence Pressure Tunnel (LTPT). It is of the closed return type and the test section is closed. The turbulence intensity is unknown, but is probably similar to the turbulence level in the Delft tunnel, because of the similarities in contraction ratio. The airfoil forces are measured using pressure taps on the wind tunnel walls and the drag is measured using a wake rake. The dimensions of the tunnel are seen in Table 8.1. A further feature of this tunnel is the possibility of increasing the pressure from $1atm$ to $10atm$ increasing the density and thereby increasing the Reynolds number. The tunnel has been used for test of a huge number of e.g. NACA airfoils, which are reported by e.g. Abbott and Doenhoff [1].

Summary of the wind tunnels

In Table 8.1 a summary of the tunnels is seen in terms of key parameters. The knowledge of these parameters is important for interpretation of the results, because the boundary and initial conditions for the tunnel flow affect the airfoil performance. The question is how the following parameters influence the performance:

- The turbulence intensity: A high turbulence intensity will move the transition from laminar to turbulent flow towards the leading edge. However, energy spectra of the turbulence are unspecified.
- The wind tunnel blockage: The ratio between the height of the test section and the chord length is a measure of how the walls/jet boundary will interact with the airfoil forces.
- The aspect ratio: The ratio between the chord length and the span width of the airfoil model gives an indication of the degree of two-dimensionality of the flow.
- Fixed or traversing wake rake: The wake rake can either be fixed to measure the velocity deficit in one plane or the wake rake can be traversed to integrate possible changes along the airfoil span.

The above list of parameters is not meant to be complete, but shows some of the very important factors that can contribute to deviations in measurements between wind tunnels.
Finally, from the limited list of wind tunnels, Table 8.1, there is a relation between contraction ratio, c_r, and turbulence intensity, TI, that follows the function: $c_r[\text{-}] = 4(TI[\%])^{-0.38}$. However, according to the theory, Barlow et al. [7], the relation should for the longitudinal direction be $c_r[\text{-}] \approx TI(U)[\%]^{-0.5}$ and for the lateral direction $c_r[\text{-}] \approx TI(V)[\%]^{-2}$, which do not agree with the observation. As stated by Barlow et al. [7], there does not appear to be a good method of predicting the effects of contraction ratios in turbulence reduction. Thus, to support the validity of the above observed relation significantly more wind tunnels have to be analyzed.

Tunnel	VELUX	LM	Delft	Stuttgart	Langley
Return	Closed	Closed	Closed	Open	Closed
Test section	Open	Closed	Closed	Closed	Closed
Test section length, L [m]	7.50	7.00	2.60	3.15	2.29
Test section height, H [m]	3.40	2.70	1.80	2.73	2.29
Test section width, W [m]	1.90	1.35	1.25	0.73	0.91
Turbulence intensity, TI [%]	1.0	0.1	0.02	0.0002	-
Chord length, c[m]	0.60	0.90	0.60	0.60	0.60
Height-chord ratio, H/c [-]	5.7	3.0	3.0	4.55	3.81
Aspect ratio, W/c [-]	3.2	1.5	2.1	1.2	1.5
Contraction ratio [-]	3.11	10	17.8	100	17.6
Maximum speed [m/s]	40	105	120	90	130
Lift measurements	Airfoil	Airfoil	Airfoil	Wall	Wall
Wake rake	Fixed	Traverse	Traverse	Traverse	-

Table 8.1. Key parameters describing the dimensions and setup of the wind tunnels.

8.5 Results

The airfoils were tested in the three tunnels at $Re = 1.6 \times 10^6$ in Delft [8] and VELUX [9] and at $Re = 1.5 \times 10^6$ in LM [10, 11]. Also, the airfoils were tested at $Re = 3.0 \times 10^6$ in Delft and at LM, but not in the VELUX wind tunnel. Furthermore, the NACA 63_3-418 airfoil was tested at $Re = 1.5 \times 10^6$ and 3×10^6 in the Stuttgart LWK and at $Re = 3.0 \times 10^6$ in the Langley LTPT.

Key parameters extracted from the wind tunnel measurements are seen for $Re = 1.5 \times 10^6$ and $Re = 3.0 \times 10^6$ for the NACA 63_3-418 airfoil in Tables 8.2-8.3 and for the Risø-B1-18 airfoil in Tables 8.4-8.5.

The measurements at $Re = 3.0 \times 10^6$ in clean configurations are compared to XFOIL, Drela [12]. XFOIL is a panel code with inviscid/viscous interaction and for a given angle of attack, AoA, and Re, it provides the c_p-distribution and lift and drag coefficients. Transition from laminar to turbulent flow was modeled by the e^n method with n = 9 corresponding to TI=0.07%. Investigations carried out by Bertagnolio et al. [13] showed that XFOIL for thin airfoils in many cases over predicts and delayed maximum lift slightly compared to EllipSys2D [14–16]. Later, Bertagnolio et al. [17] investigated 3D airfoil computations using different turbulence models, which showed significant differences in the prediction of maximum lift. However, at low angles of attack both XFOIL and EllipSys predicted the airfoil performance quite well.

	Delft	LM	Stuttgart	VELUX
$Re \times 10^{-6}$	1.6	1.5	1.5	1.6
AoA_0	-2.5	-3.5	-3.3	-2.2
$c_{l,max}$	1.23	1.31	1.32	1.33
$AoA_{cl,max}$	11.3	11.1	12.3	16.3
$c_{d,min}$	0.0064	0.0083	0.0072	0.0093
$\left(\frac{c_l}{c_d}\right)_{max}$	119.5	101.1	110.9	73.0
$AoA_{(cl/cd)_{max}}$	6.1	5.1	5.7	5.0
$c_{l,(cl/cd)_{max}}$	1.00	0.94	1.02	0.80

Table 8.2. Key values describing the aerodynamic performance of the NACA 63_3-418 *in clean surface configuration at* $Re = 1.5 \times 10^6$ *to* $Re = 1.6 \times 10^6$

	Delft	LM	Stuttgart	Langley
$Re \times 10^{-6}$	3.0	3.0	3.0	3.0
AoA_0	-2.5	-3.2	-3.0	-2.8
$c_{l,max}$	1.30	1.35	1.30	1.38
$AoA_{cl,max}$	12.8	11.7	10.9	13.3
$c_{d,min}$	0.0062	0.0054	0.0062	0.0060
$\left(\frac{c_l}{c_d}\right)_{max}$	121.1	134.8	114.7	121.6
$AoA_{(cl/cd)_{max}}$	5.2	5.1	4.4	6.1
$c_{l,(cl/cd)_{max}}$	0.91	0.93	0.86	1.01

Table 8.3. Key values describing the aerodynamic performance of the NACA 63_3-418 *in clean surface configuration at* $Re = 3.0 \times 10^6$

8.5.1 NACA 63_3-418

Reynolds number 1.5×10^6

Figure 8.2 shows results for the clean configuration. Here, also data from the Stuttgart tunnel is included for comparison. It is seen that there is no exact agreement between the data from the different tunnels. There are several deviations between the measurements. The determination of the zero-lift-angle-of-attack, AoA_0, from the different tunnels is measured within the range of 1.3 degrees. This can be due to uncertainties in measuring the geometric AoA, shape deviations in the airfoil contour and corrections of the measured lift. The slopes of the linear part of the lift curve agree fairly well between 0.111 and 0.116 per degree (between $2\pi + 0.077 rad^{-1}$ and $2\pi + 0.363 rad^{-1}$) with a somewhat higher slope in the Delft tunnel and lower slope in the

	Delft	LM	VELUX
$Re \times 10^{-6}$	1.6	1.5	1.6
AoA_0	-3.6	-4.3	-3.3
$c_{l,max}$	1.55	1.50	1.64
$AoA_{cl,max}$	11.8	11.4	13.5
$c_{d,min}$	0.0080	0.0074	0.0090
$\left(\frac{c_l}{c_d}\right)_{max}$	122.6	125.3	100.2
$AoA_{(cl/cd)_{max}}$	8.2	7.1	6.5
$c_{l,(cl/cd)_{max}}$	1.36	1.21	1.16

*Table 8.4. Key values describing the aerodynamic performance of the Risø-*B1-18 *in clean surface configuration at* $Re = 1.5 \times 10^6$ *to* $Re = 1.6 \times 10^6$

	Delft	LM
$Re \times 10^{-6}$	3.0	3.0
AoA_0	-3.5	-3.9
$c_{l,max}$	1.68	1.66
$AoA_{cl,max}$	12.3	12.9
$c_{d,min}$	0.0072	0.0067
$\left(\frac{c_l}{c_d}\right)_{max}$	135.8	129.7
$AoA_{(cl/cd)_{max}}$	7.2	6.1
$c_{l,(cl/cd)_{max}}$	1.30	1.15

*Table 8.5. Key values describing the aerodynamic performance of the Risø-*B1-18 *in clean surface configuration at* $Re = 3.0 \times 10^6$

VELUX tunnel. The slope seems not to correlate with the wind tunnel layout parameters shown in Table 8.1. The maximum lift coefficients, $c_{l,max}$, agree fairly well between 1.23 and 1.33. It is noted that the AoA, at which $c_{l,max}$ appears, $AoA_{cl,max}$, increases with increasing ratio of H/c. This means that a reduction in blockage could be the reason for an increase in $c_{l,max}$. However, several other parameters determine the level of $c_{l,max}$ such as TI [18], the aspect ratio and whether the lift measurement is carried out on the tunnel walls or on the airfoil surface. Also, the quality of the models determines the level. However, to the extent that these parameters are known they do not correlate with the variations in $c_{l,max}$.

The drag coefficient, c_d, differs somewhat and especially in the VELUX tunnel which has a rather high TI compared to the other tunnels. Because the Delft tunnel shows the lowest minimum drag values, $c_{d,min}$, there seems however not to be a clear correlation between TI and $c_{d,min}$, since the Stuttgart tunnel has lower TI than the Delft tunnel. However, parameters such as the degree of two-dimensionality of the flow and the method of measuring the wake deficit can also affect the prediction of c_d. Somewhat fluctuating c_d from the LM tunnel seems to appear, which probably is caused by less sensitivity of the measurement equipment, because it is calibrated for Reynolds numbers between $Re = 3.0 \times 10^6$ and $Re = 6.0 \times 10^6$.

Figure 8.3 shows data for the LER configuration (zigzag tape mounted on suction side at $x/c = 0.05$ from the leading edge and on pressure side at $x/c = 0.10$ from the leading edge). Here, only data from Delft and VELUX is available with the prescribed zigzag tape. Also, measurements from Stuttgart [6] are shown with a somewhat different way of simulating the leading edge roughness. The data from Delft and VELUX agrees very well, however with somewhat higher c_d in the VELUX tunnel. The data from Stuttgart is not based on the same LER simulation and cannot be directly compared. However, it shows the same trends in the decrease in $c_{l,max}$ and increase in c_d.

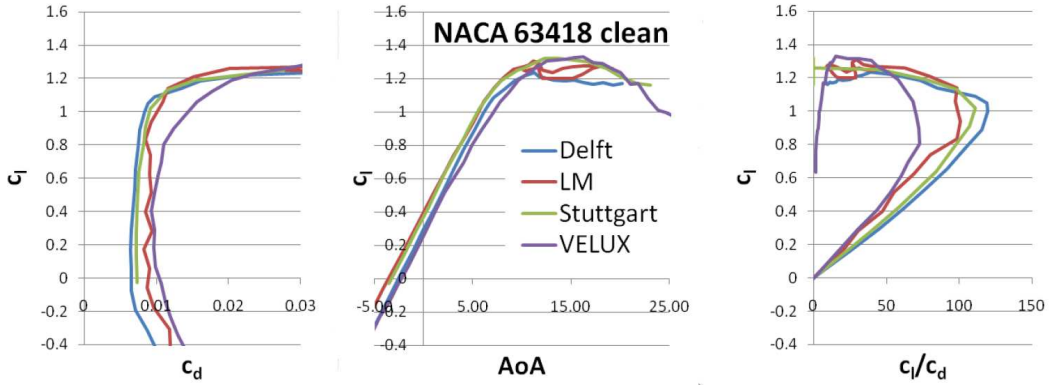

Figure 8.2. Polars of the NACA 63_3-418 airfoil at $Re = 1.5 \times 10^6$ to $Re = 1.6 \times 10^6$ in clean configuration

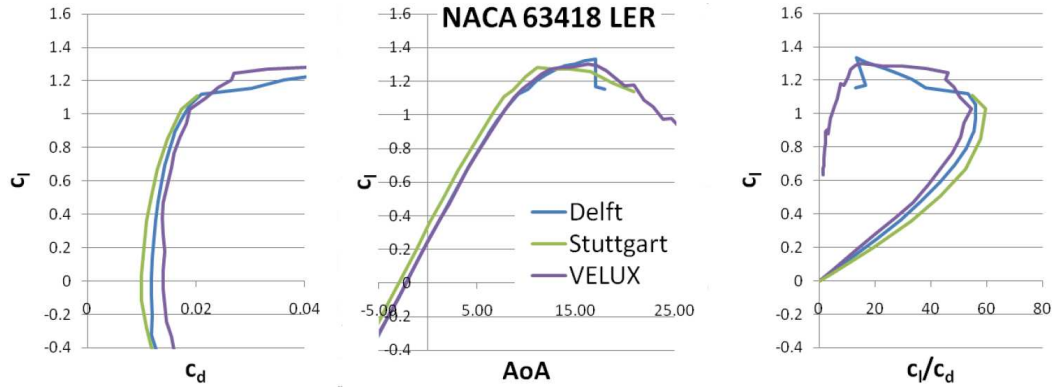

Figure 8.3. Polars of the NACA 63_3-418 airfoil at $Re = 1.6 \times 10^6$ in LER configuration

Reynolds number 3.0×10^6

Figure 8.4 shows results for the clean configuration. Here, the VELUX tunnel is not part of

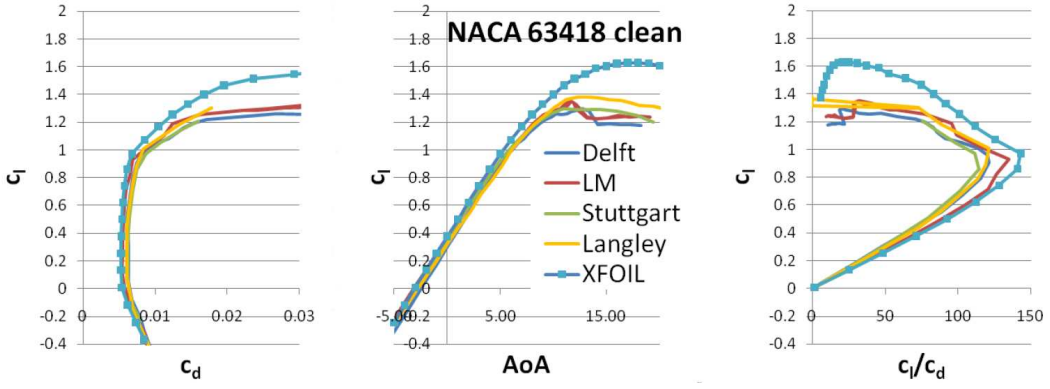

Figure 8.4. Polars of the NACA 63_3-418 airfoil at $Re = 3.0 \times 10^6$ in clean configuration

the comparisons, because this Reynolds number is above the range of this tunnel. However, data from the Stuttgart and the Langley tunnels are included for comparison. It is seen that the agreement between the data in the different tunnels are much better than at 1.5×10^6 for the

clean configuration. However, there are still some deviations between the measurements. The determination of AoA_0 from the different tunnels is measured within the range of 0.7 degree. As for the lower Reynolds number this can be due to uncertainties in measuring the geometric AoA, shape deviations in the airfoil contour and corrections of the measured lift.
The slopes of the linear part of the lift curve agree fairly well between 0.112 and 0.120 per degree (between $2\pi + 0.114 rad^{-1}$ and $2\pi + 0.592 rad^{-1}$) with a somewhat higher slope in the Delft tunnel and lower slope in the Langley tunnel. As was the case for the lower Reynolds number, the slope seems not to correlate with the wind tunnel layout parameters shown in Table 8.1. Agreement of $c_{l,max}$ is fairly good between 1.30 and 1.38. No correlations between the $AoA_{cl,max}$ and the four parameters 1) the ratio H/c, 2) TI, 3) the ratio W/c and 4) whether the pressure is measured on the airfoil surface or on the walls have been detected as was the case at the lower Reynolds number.
Agreements of c_d are quite well at all lift coefficients with $c_{d,min}$ between 0.0055 in the LM tunnel and 0.0062 in the Stuttgart tunnel. Because the LM tunnel with the highest TI (which is quite low) shows the lowest c_d and the Stuttgart tunnel with lowest TI shows the highest c_d, an expected reduction in c_d with a reduction in TI is not observed. Since c_d depend on more parameters than TI such as the airfoil surface quality, the resolution of the pressure tubes in the wake rake measuring the pressure in the airfoil wake, the method used to detect the wake and the Mach number, no conclusions regarding correlation of the drag measurements to the wind tunnel configuration can be drawn. Finally, the results with clean configuration are compared to XFOIL computations. It is seen that XFOIL predicts the aerodynamic performance well at low AoA, however with somewhat under predictions of c_d. At high AoA XFOIL seems to over predict $c_{l,max}$ and c_l for separated flows significantly.

8.5.2 Risø-B1-18

Reynolds number 1.5×10^6

The Risø-B1-18 airfoil was like the NACA 63_3-418 airfoil tested in the three tunnels at $Re = 1.6 \times 10^6$ at Delft and VELUX and at $Re = 1.5 \times 10^6$ at LM. Figure 8.5 shows data for the clean configuration and Figure 8.6 shows data for the LER configuration at $Re = 1.5 \times 10^6$ to $Re = 1.6 \times 10^6$.
As for the NACA 63_3-418 airfoil at $Re = 1.6 \times 10^6$. it is seen that there is no exact agreement

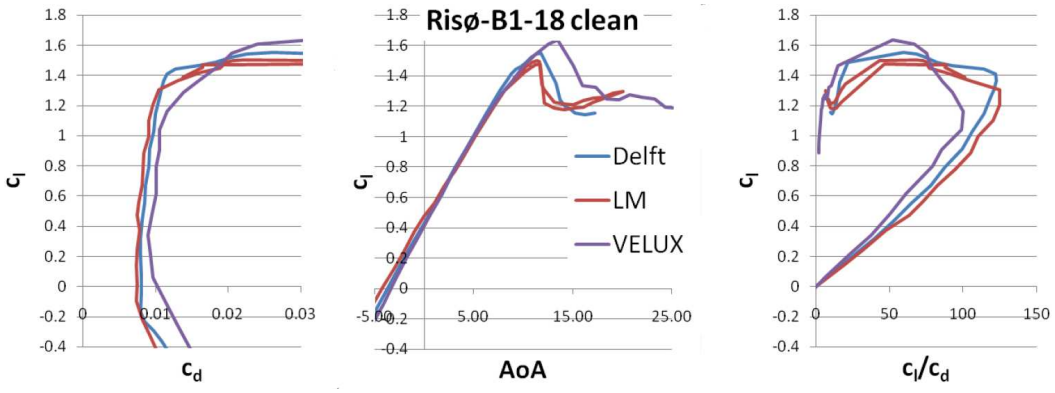

Figure 8.5. Polars of the Risø-B1-18 airfoil at $Re = 1.5 \times 10^6$ to 1.6×10^6 in clean configuration

between the data in the different tunnels for the clean configuration. The results deviated from each other in several ways.
The determination of AOA_0 from the different tunnels is within 1.0 degree. As for the NACA 63_3-418 airfoil this can be due to uncertainties in measuring the geometric AoA, shape deviations in the airfoil contour and corrections of the measured lift.

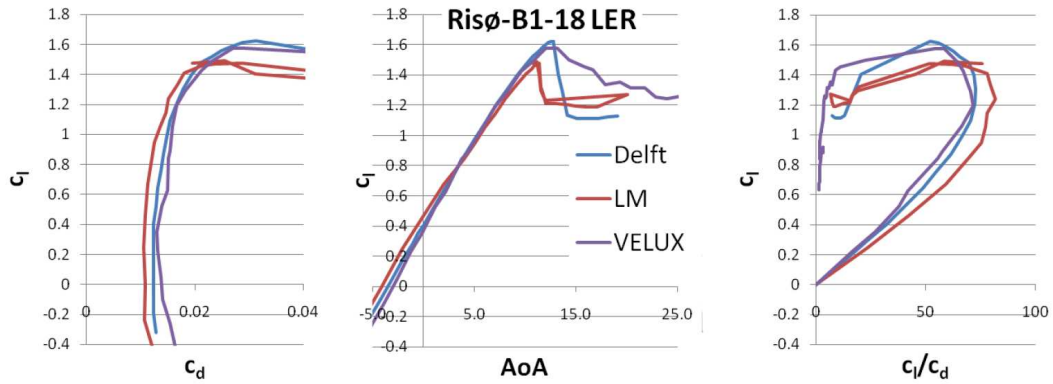

Figure 8.6. Polars of the Risø-B1-18 airfoil at $Re = 1.5 \times 10^6$ to 1.6×10^6 in LER configuration

The slopes of the linear part of the lift curve differ somewhat between 0.106 and 0.122 per degree (between $2\pi - 0.21 rad^{-1}$ and $2\pi + 0.71 rad^{-1}$), again with somewhat higher slope in the Delft tunnel and lower slope in the LM tunnel. However, the slope seems not to correlate with the wind tunnel layout parameters shown in Table 8.1.
Significant differences are seen for $c_{l,max}$ and the stall characteristics, between 1.48 and 1.64. Since the VELUX tunnel shows the highest $c_{l,max}$ there might be a correlation between on one hand the ratio H/c, the ratio W/c or whether the test section is open or closed and on the other hand $c_{l,max}$. However, other parameters such as TI might influence the measurements significantly. Thus, there is no clear correlation between $c_{l,max}$ and the wind tunnel layout.
Some differences are seen for c_d and especially in the VELUX tunnel as was the case for the NACA 63_3-418 airfoil. Thus, the measurements show that high TI affects c_d, but that TI below a certain level does not affect the determination of $c_{d,min}$. However, comparing the c_l vs c_d plot, Figure 8.5, a "knee" in the curve is seen for both LM and Delft data. The knees appear at $c_l \approx 1.3$ for the LM data and at $c_l \approx 1.4$ for the Delft data. The knees indicate the lift levels at which the transition from laminar to turbulent flow moves towards the leading edge. Thus, it seems that the somewhat higher TI or the given energy spectra of the turbulence in the LM tunnel affects the transition from laminar to turbulent flow in an earlier stage than the Delft tunnel. For the LER configuration c_l from Delft and VELUX agrees very well, however with somewhat higher c_d in the VELUX tunnel and more abrupt stall in the Delft tunnel.

Reynolds number 3.0×10^6

The Risø-B1-18 airfoil was tested in only two tunnels, Delft and LM, at $Re = 3.0 \times 10^6$. Figure 8.7 shows results for the clean configuration and Figure 8.8 shows data for the LER configuration at $Re = 3.0 \times 10^6$. It is seen that there is very good agreement between the data in the two tunnels for the clean configuration. However, the results deviated from each other in a few ways. The determination of AoA_0 from the different tunnels is within 0.4 degree. No other reasons for this than those mentioned for the test at the lower Reynolds number are known.
The slopes of the linear part of the lift curve differ somewhat between 0.115 and 0.123 per degree (between $2\pi + 0.31 rad^{-1}$ and $2\pi + 0.76 rad^{-1}$), again with somewhat higher slope in the Delft tunnel and lower slope in the LM tunnel. Very similar values of $c_{l,max}$ is seen, between 1.66 and 1.68, and also the stall characteristics are very similar.
Also, the c_d values are very similar. However, as was the case at $Re = 1.6 \times 10^6$, the knee of the c_l vs c_d plot appears at different cl for the two tunnels. In the Delft tunnel the knee appears at higher c_l, indicating lower TI, which is in good agreement with the specifications for the tunnels. Thus, as long as TI is fairly low ($\leq 0.1\%$) it seems that it does not affect c_d very much. However, it seems to affect the dynamics of the transition point location.

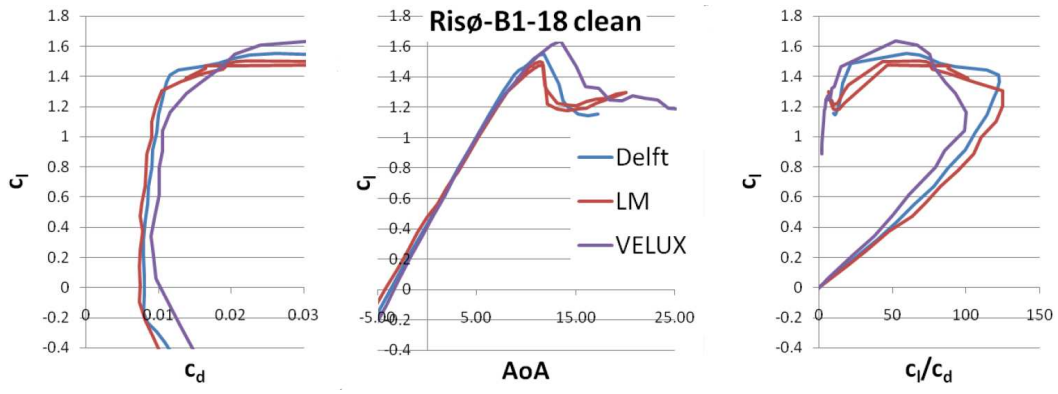

Figure 8.7. Polars of the Risø-B1-18 airfoil at $Re = 3.0 \times 10^6$ in clean configuration

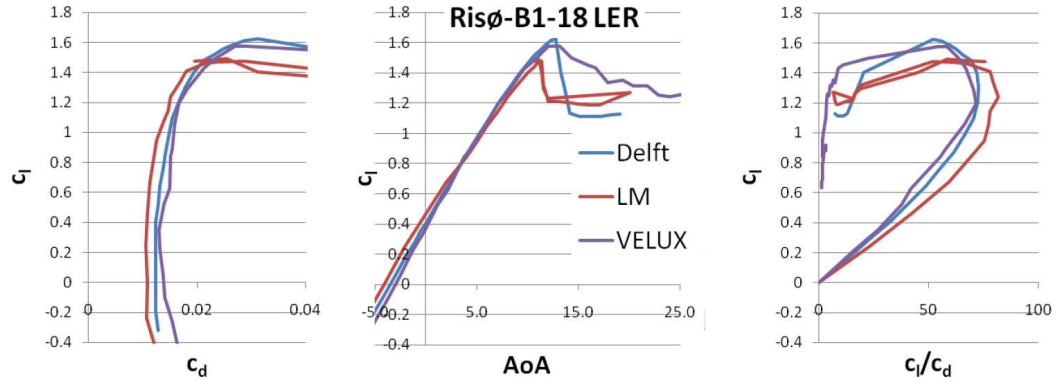

Figure 8.8. Polars of the Risø-B1-18 airfoil at $Re = 3.0 \times 10^6$ in LER configuration

For the LER configuration c_l from Delft and LM agrees very well, but with some difference in $c_{l,max}$, between 1.62 and 1.72.
The determination of AoA_0 is within 0.5 degrees in this case. Also, differences are seen in c_d, with higher c_d in the Delft tunnel. Thus, some deviations in aerodynamic performance are observed for the Risø-B1-18 airfoil when comparing the clean configuration with the LER configuration.
This can however be due to small differences in the geometry of the zigzag tape and the relatively thicker zigzag tape as stated in section 8.3, or the way the zigzag tape was mounted on the airfoil surface.
Finally, the data with clean configuration is compared to XFOIL computations using the e to the nth method with $n = 9$. It is seen that XFOIL predicts the aerodynamic performance well at low AoA, however with somewhat under predictions of c_d. Especially the knee at the c_l vs c_d plot is quite well predicted. At high AoA, the measurements do not agree very well with the predictions and XFOIL over predicts $c_{l,max}$ and c_l for the separating airfoil significantly.

8.6 Conclusions

This paper showed polars measured in the LM Wind Power LSWT, the Delft LSLT tunnel and the VELUX tunnel carried out in the DAN-AERO MW project. Comparing the polars revealed differences in zero-lift-angle-of-attack, the slope of the linear part of the lift curve, maximum lift, the stall characteristics and the drag. Here, also a few measurements carried out in the

Stuttgart LWK and the Langley LTPT were used for the comparisons. Even though the wind tunnel tests deviated in several ways, only the general conclusions will be emphasized here. The best agreement between results was seen for Reynolds number of $Re = 3.0 \times 10^6$. The results for Reynolds numbers of $Re = 1.6 \times 10^6$ deviated somewhat from each other. This was probably due to the (lack of) sensitivity of the measurement equipment and the calibration of the wind tunnels, because the tunnels are designed to work at different Reynolds numbers.
With the rather high turbulence intensity of 1% in the VELUX tunnel all comparisons of polars showed significantly higher drag values in the VELUX tunnel. However, for the rest of the wind tunnels it seems that the minimum drag was not influenced by the turbulence intensity. Thus, with a turbulence intensity below a certain value, which is minimum TI=0.1%, minimum drag seems to be unaffected by the turbulence level. However, the transition point location seems to be affected by the turbulence intensity, so that differences in the airfoil performance will be seen clearly, if fast changes appear in the transition point location. No clear correlation between on one side the maximum lift, the stall, the zero-lift angle-of-attack and the slope of the linear part of the lift curve and on the other side the wind tunnel layout could be identified. However, this might be due to counteracting mechanisms such as extremely low turbulence intensity, which could tend to reduce maximum lift, combined with a relatively high ratio between test section height and chord length, which might increase the maximum lift. Thus, most of the differences between the measurements are ascribed to differences in airfoil model shapes, methods for analyzing the data and calibrations.
In addition, the measurements were compared to XFOIL computations. This comparison revealed the necessity to be aware of e.g. the turbulence intensity when using airfoil characteristics for wind turbine design. It also revealed the limitations in XFOIL, where the drag coefficient in general was under predicted and maximum lift and the lift on the separating airfoil was significantly over predicted. Furthermore, the comparisons between measurements and the predictions by XFOIL stress the necessity to carry out wind tunnel measurements to validate the flow simulations. When validating the airfoil performance in a wind tunnel, this work revealed the importance of specifying the turbulence intensity. It is however not known for the time being, which turbulence intensity that represents atmospheric flow on wind turbine blades.

References

[1] I.H. Abbot and A.E. von Doenhoff. *Theory of wing sections*. New York Dover publications Inc., 1959.

[2] P. Fuglsang and C. Bak. Development of the Risø wind turbine airfoils. *Wind Energy*, 7:145–162, 2004.

[3] P. Fuglsang, I. Antoniou, N.N. Sørensen, and H.Aa. Madsen. Validation of a wind tunnel testing facility for blade surface pressure measurements. Technical Report Risø-R-981(EN), Risø National Laboratory, 1998.

[4] P. Fuglsang and S. Bove. Wind tunnel testing of airfoils involves more than just wall corrections. *EWEC, 2008, Brussels, Belgium*, 2008.

[5] W.A. Timmer. Wecs-blade airfoils-the NACA 63-4xx series. *Proc. European Community Wind Energy. Conference Madrid, Spain*, 1990.

[6] D Althaus. *Niedriggeschwindigkeitsprofile*. Vieweg & Sohns Verlagsgesellschaft, 1996.

[7] J.B. Barlow, W.H. Rae Jr., and A. Pope. *Low-Speed Wind Tunnel Testing*. John Wiley & Sons, Inc., third edition, 1999.

[8] W. Timmer. Wind tunnel test results for airfoils NACA 633-418 and Risø B1-18. Technical Report WE-082063, Delft University of Technology, Faculty of Aerospace Engineering, Wind Energy Research Group, 2008.

[9] P. Fuglsang, C. Bak, M. Gaunaa, and I. Antoniou. Wind tunnel tests of Risø-B1-18 and Risø-B1-24. Technical Report Risø-R-1375(EN), Risø National Laboratory, 2003.

[10] O. Müller. LSWT report of campaign NACA 63-418 1, public version. Technical Report Rev 1.0, LM Glasfiber, 2009.

[11] O. Müller. LSWT report of campaign Risø-B1-18. Technical Report Rev 3.0, LM Glasfiber, 2009.

[12] M. Drela. *XFOIL, An Analysis and Design system for Low Reynolds Number Airfoils, Low Reynolds Number Aerodynamics. Volume 54*. Springer- Verlag Lec. Notes in Eng., 1989.

[13] F. Bertagnolio, N.N. Sørensen, J. Johansen, and P. Fuglsang. Wind Turbine Airfoil Catalogue. Technical Report Risø-R-1280(EN), Risø National Laboratory, 2001.

[14] J.A. Michelsen. Basis3D - a platform for development of multiblock PDE solvers. Technical report AFM 92-05, Technical University of Denmark, Lyngby, 1992.

[15] J.A. Michelsen. Block structured multigrid solution of 2D and 3D elliptic PDEs. Technical Report AFM 94-06, Technical University of Denmark, 1994.

[16] N.N. Sørensen. *General Purpose Flow Solver Applied to Flow over Hills*. PhD thesis, Technical University of Denmark, 1995.

[17] F. Bertagnolio, N.N. Sørensen, and J. Johansen. Profile Catalogue for Airfoil Sections Based on 3D Computations. Technical Report Risø-R-1581(EN), Risø National Laboratory, 2006.

[18] C. Bak, P.B. Andersen, H.A. Madsen, M. Gaunaa, P. Fuglsang, and S. Bove. Design and Verification of Airfoils Resistant to Surface Contamination and Turbulence Intensity. *AIAA 2008-7050, 26th AIAA Applied Aerodynamics Conference, 18 - 21 August 2008, Honolulu, Hawaii*, 2008.

9 Investigation of 3D aerofoil characteristics on the NM80 turbine

Author(s): N. Troldborg, C. Bak, N.N Sørensen, H.Aa. Madsen, P-E, Réthoré, F. Zahle, S. Guntur

This section deals with 3D aerofoil characteristics on the NM80 wind turbine.

9.1 Introduction

Aerodynamic aerofoil characteristics used for design of wind turbines are usually obtained from wind tunnel tests. However, the actual 3D aerofoil characteristics on a rotor can be quite different from those measured in a wind tunnel because of centrifugal forces in the boundary layer, spanwise pressure gradients generated by the Coriolis force as well as unsteady and turbulent inflow conditions. Thus, a direct application of the 2D characteristics obtained in a wind tunnel shows bad agreement between measured and calculated loads especially at the inner part of the blade where the 3D effects are most dominant.
This chapter studies 3D aerofoil characteristics in comparison with aerofoil performance in 2D flow through a combination of field measurements, wind tunnel tests and computational fluid dynamics (CFD).

9.2 Experimental approach

In this investigation both field and wind tunnel measurements obtained within the DANAERO experiment have been used.
From the field experiment on the NM80 turbine the following sensors are used:

- 4×64 surface pressure taps at the four radial stations, r/R=0.325, 0.475, 0.750 and 0.925 of the LM38.8 blade where the relative thickness of the aerofoils is 33%, 24%, 20% and 19%, respectively.
- Four five-hole Pitot tubes mounted at r/R=0.36, 0.51, 0.78 and 0.90, respectively.
- Rotational speed of the rotor
- Pitch of the blade
- Velocity measured at the met mast
- Air density (derived from temperature and pressure measurements)

From the wind tunnel measurements the following sensors are used:

- 4×64 surface pressure taps on four aerofoils with nearly the same geometry as the four blade sections of the LM38.8 blade which were instrumented with pressure taps.
- Drag measurements from a wake rake.

These data creates a basis for studying how the aerodynamic characteristics on a real wind turbine deviates from those obtained in 2D in a wind tunnel.

9.3 Computational approach

Two different types of simulations are carried out using the in-house incompressible finite volume Reynolds Averaged Navier-Stokes (RANS) flow solver EllipSys [1–3]:

- 2D steady state simulations on the four aerofoil sections using the $k-\omega$ SST turbulence model [4] and a correlation based transition model [5–7]. The grids used for the simulations were of the O-mesh type. The domain height was set to approximately 30 chord lengths and the height of the first cell adjacent to surface was set to 10^{-6} chord lengths corresponding to a maximum y^+ of approximately 0.2. All grids had 256 cells around the aerofoil and 128 cells normal to the aerofoil.
- 3D rotor computations on the NM80 turbine in steady and uniform inflow using the same turbulence and transition models as used for the 2D simulations. In the simulations the rotor geometry and the blade surface boundary layer is fully resolved using a standard O-O mesh configuration. The radius of the domain was approximately 10 rotor diameters and the height of the first cell adjacent to the blade surface was set to satisfy the condition $y^+ < 1$ as required for this type of computations. The blades of the turbines were resolved with $256 \times 128 \times 128$ cells in the chordwise, spanwise and normal direction, respectively. The grid consisted of 432 block of 32^3 ($14 \cdot 10^6$) grid cells.

These computed data can be considered analogous to the experimental datasets and forms a basis for studying the difference between 2D and 3D aerofoil characteristics.

9.4 Results

In the following selected results from the analysis of measurements and simulations will be presented.

9.4.1 Comparison of wind tunnel measurements and 2D simulations

In this section the wind tunnel measurements and 2D aerofoil computations are validated by comparing them against each other.
Figure 9.1 shows C_p distributions at three different angles of attack (AoA) for smooth aerofoils at a Reynolds number of $Re = 5 \cdot 10^6$. For the sections at r/R=0.475, 0.750 and 0.925 the agreement is good except at the highest AoA, where the computations predicts a much larger suction peak than observed in the measurements. Similar discrepancies have been seen in previous work [8] and indeed these aerofoils are quite challenging to simulate at high AoA because the transition point is located rather far aft on these aerofoils. For the thickest aerofoil (r/R=0.325) there are quite large discrepancies between computations and measurements for all AoA. The reason for these discrepancies are most likely due to tunnel blockage and 3D effects caused by the walls of the wind tunnel. While 3D effects are also present for thin aerofoils they are only important at higher AoA. As shown in [9] 3D effects are particularly pronounced for thick aerofoils as well as at high AoA and in order to predict the correct stalling behaviour the inclusion of the tunnel walls is important as these may play an important role in the actual aerodynamic behaviour of the aerofoil in the wind tunnel.
Figures 9.2-9.3 shows C_L and C_D polars for each section. The lift and drag coefficients are defined as:

$$C_L = \frac{F_L}{\frac{1}{2}\rho c V_{rel}^2}$$

$$C_D = \frac{F_D}{\frac{1}{2}\rho c V_{rel}^2}$$

where F_L and F_D is the lift and drag force per meter, respectively, ρ is the air density, V_{rel} is the relative velocity and c is the local chord length.
Computations have been carried out assuming both transitional and fully turbulent flow over the aerofoil surface. For the three thinnest sections the computed $C_{L,max}$ is significantly higher than the measured, which is as expected from the C_p distributions shown in Figure 9.1. For the

thickest aerofoil the computed and measured lift coefficient does not show much resemblance, which is most likely a combined consequence of wind tunnel effects and the inadequacy of simulating the flow over thick aerofoils as 2D. In all cases the simulations are seen to predict higher drag at low AoA than what is measured in the wind tunnel. This is because the used grid resolution in the chordwise direction is not sufficiently high for this type of aerofoils. We did simulations with increased chordwise resolution of 384 cells and found that the drag in these simulations were in much closer agreement with measurement at low AoA. However, these results are not shown here because we want to make a one-to-one comparison with the 3D computations where 256 grid cells were used in the chordwise direction.

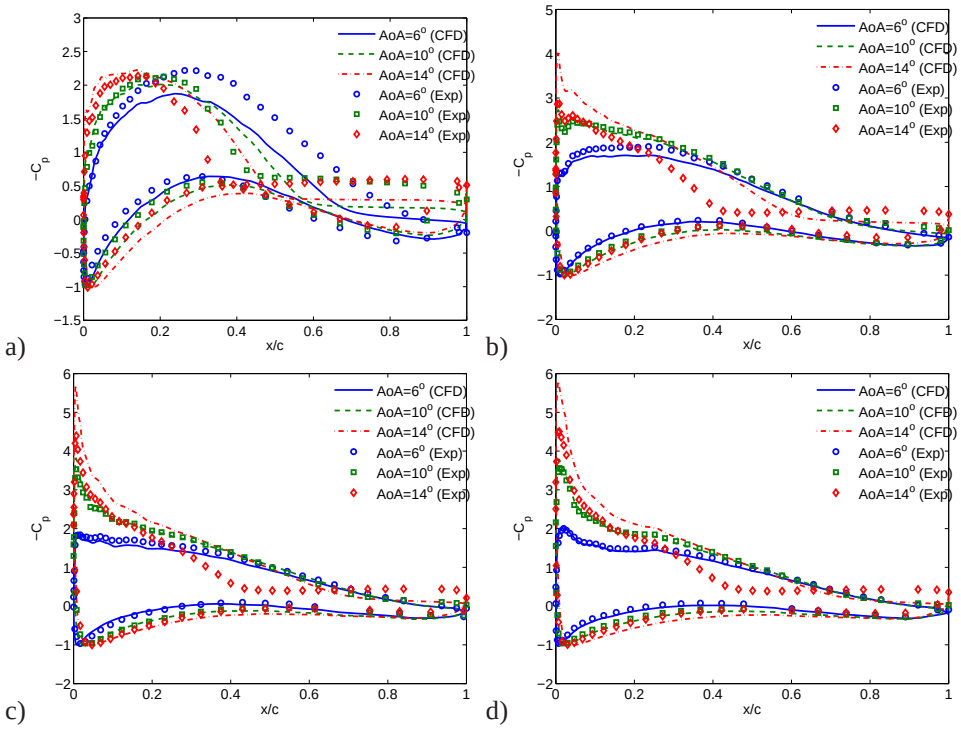

Figure 9.1. C_p^* distributions predicted from wind tunnel measurements and 2D computations.a) r/R=0.325; b) r/R=0.475; c) r/R=0.750; d) r/R=0.925.

9.4.2 Comparison of field measurements and 3D rotor simulations

In order to validate the 3D rotor computations and the field measurements a comparison of the pressure distributions along the four investigated blade sections was conducted at different operational conditions.

For the comparison 1-minute averages of C_p distributions were extracted from the DANAERO database in cases where the turbine was operating in undisturbed flow at nearly constant rotational speed and pitch. During the DANAERO field measurement campaign a number of tests were carried out where the turbine was forced to operate at fixed pitch and rotational speed. Even though this means that the turbine is operating off design in these cases they are suitable for comparison with CFD. In all cases the measured C_p distribution is computed as:

$$C_p = \frac{p - p_\infty}{\frac{1}{2}\rho\left(V_\infty^2 + (r\Omega)^2\right)}$$

where V_∞ is the free-stream velocity measured by the met mast located nearby, P_∞ is the ambient pressure, r is the radial position of the blade section, Ω is the rotational speed of the turbine

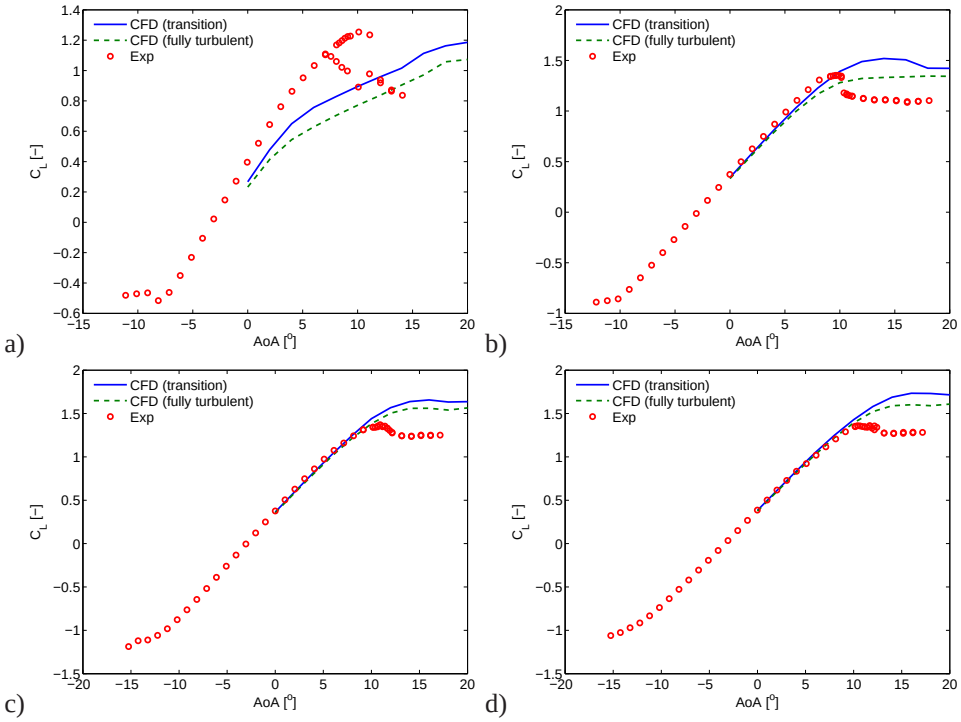

Figure 9.2. Lift coefficient predicted from wind tunnel measurements and 2D aerofoil computations. a) r/R=0.325; b) r/R=0.475; c) r/R=0.750; d) r/R=0.925.

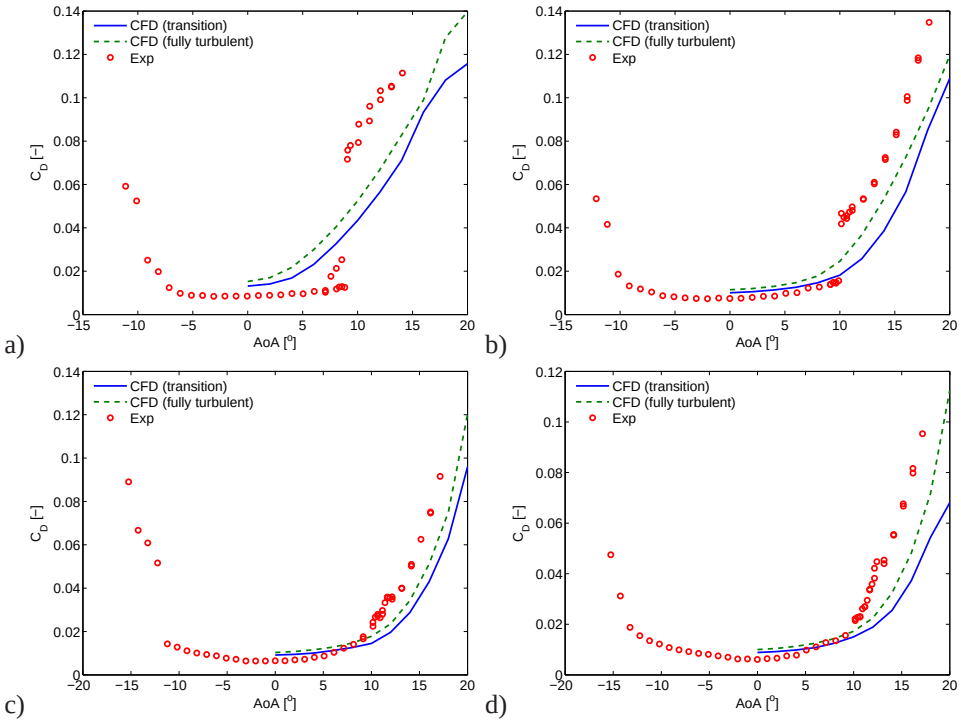

Figure 9.3. Drag coefficient predicted from wind tunnel measurements and 2D aerofoil computations. a) r/R=0.325; b) r/R=0.475; c) r/R=0.750; d) r/R=0.925.

and ρ is the air density.
Figures 9.4-9.5 compare measured and computed pressure distributions at different free-stream velocity and operational conditions as specified in the figure captions. Note that a negative pitch

angle means towards stall. The errorbars included in the plots shows the standard deviation of the measured 1 minute averages and thus represent the scatter in the measurements. As seen the pressure distributions are generally in quite good agreement and the numerical predictions generally lie within the uncertainty bars. However, a general trend is that the computed suction peak for the two outermost sections is over predicted in comparison with measurements. The discrepancies may be explained as differences in inflow conditions caused by wind shear/veer, turbulence and yaw error.

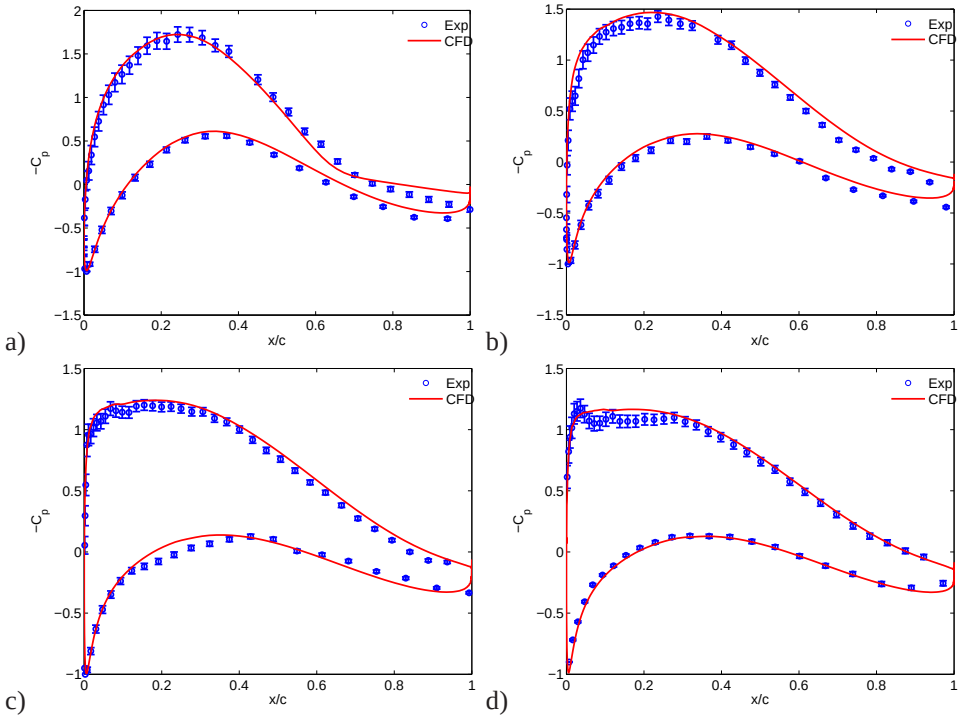

Figure 9.4. Comparison of measured and computed C_p distributions on the NM80 turbine operating at $V_\infty = 6.1ms^1$ at a rotational speed of 12.1 RPM and a pitch angle of 0.15^o. a) r/R=0.325; b) r/R=0.475; c) r/R=0.750; d) r/R=0.925.

9.4.3 Comparison of 2D and 3D aerofoil characteristics

In order to compare 2D and 3D aerofoil characteristics it is necessary to determine the angle of attack (AoA) at the different blade sections on the rotor blade. Several methods have been proposed for this purpose. Here we use the azimuthal averaging technique (AAT) employed by Hansen and Johansen [10, 11] in which the velocity, at a given radial position in the rotor plane, is calculated using the azimuthally averaged velocity at axial positions up and downstream of the rotor. Since the AAT requires information about the velocity field both up and downstream we can not use it to estimate the AoA from the measurements. Instead the AoA in the measurements is computed using the following procedure:

- Extract measured 1-minute averaged C_p^{exp} distributions for each blade section and bin average them on the flow angle measured directly by the pitot tube located at r/R=0.78 using bins of $\pm 0.5^o$, i.e. establish $C_p^{exp}(AoA_{pitot})$
- From the 3D rotor computations determine the AoA for each blade section using the AAT and establish the computed $C_p^{cfd}(AoA)$.
- Estimate the measured AoA in an optimization process involving minimizing the objective

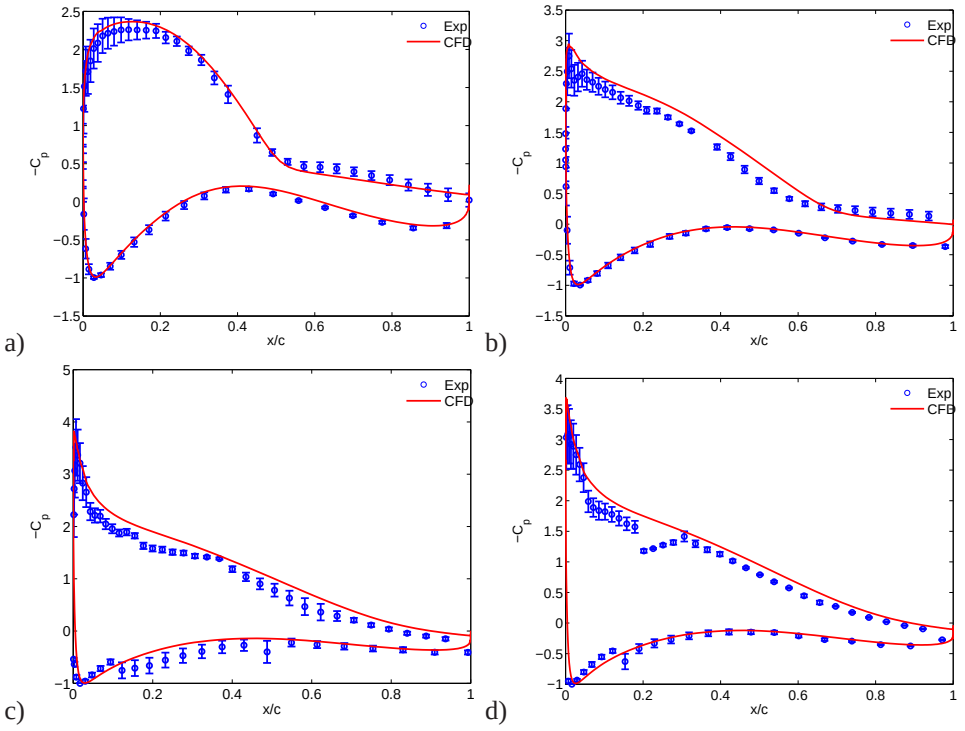

Figure 9.5. Comparison of measured and computed C_p distributions on the NM80 turbine operating at $V_\infty = 10.5ms^1$ at a rotational speed of 16.2 RPM and a pitch angle of -4.75^o. a) r/R=0.325; b) r/R=0.475; c) r/R=0.750; d) r/R=0.925.

function:

$$min \left\| \sum_{i=1}^{n} \left(C_p^{exp}(AoA_{pitot}) - C_p^{cfd}(AoA) \right)^2 \right\|$$

where $n = 64$ is the number of pressure taps along the aerofoil section.

In this way transfer functions from AoA_{pitot} to AoA in 3D is established.
Figures 9.6-9.7 show measured and computed C_p distributions at the different blade sections in comparison with the corresponding distributions obtained in the wind tunnel and using 2D computations. Generally, the agreement between the measurements on the rotor and the rotor computations is fairly good. The observed discrepancies is partly due to uncertainties in determining C_p from the measurements where we do not know the true free-stream velocity but also due to inadequate turbulence modelling.
For $AoA = 6^o$ the flow appears to be 2D over most of the blade span but even at this low AoA there are important difference between 2D and 3D flows at the inner and outermost sections. The pressure over the suction side is generally slightly higher in 2D than in 3D. We cannot explain this difference but it is interesting to notice that it appears both in the computations and in the measurements.
At the high AoAs, the suction over most of the upper aerofoil surface at r/R=0.325 is higher in 3D than in 2D and also the position where a nearly constant pressure level is reached is closer to the trailing edge in 3D than in 2D. This indicates a delay in stall on the rotor compared to the 2D case. This stall delay can be explained to be caused by the presence of Centrifugal/Coriolis on the rotor.
Figure 9.8-9.9 shows respectively the normal and tangential force coefficients integrated from the pressure distributions. The normal force coefficient, C_n, and the tangential force coefficient,

C_t, are defined as:

$$C_n = \frac{F_n}{\frac{1}{2}\rho c\,(V_\infty^2 + (r\Omega)^2)}$$

$$C_t = \frac{F_t}{\frac{1}{2}\rho c\,(V_\infty^2 + (r\Omega)^2)}$$

where F_n and F_t is the normal and tangential force per meter, respectively, integrated from the C_p distributions.
Generally, the agreement between 3D rotor computations and rotor measurements is good, however there are important differences at r/R=0.750, where it seems that C_n measured on the rotor is closer to the $2D$ computations.
At high AoA the C_n values indicate delay in stall at r/R=0.325 and r/R=0.475. At the outermost section the C_n values are below the 2D values for all AoA and it also seems that the slope of the C_n curve is lower in 3D than in 2D. Shen et al. [12] showed similar behaviour of the lift coefficient near the tip of a rotor. From Figure 9.7 it appears that the lower C_n is caused by a reduction in the suction peak.

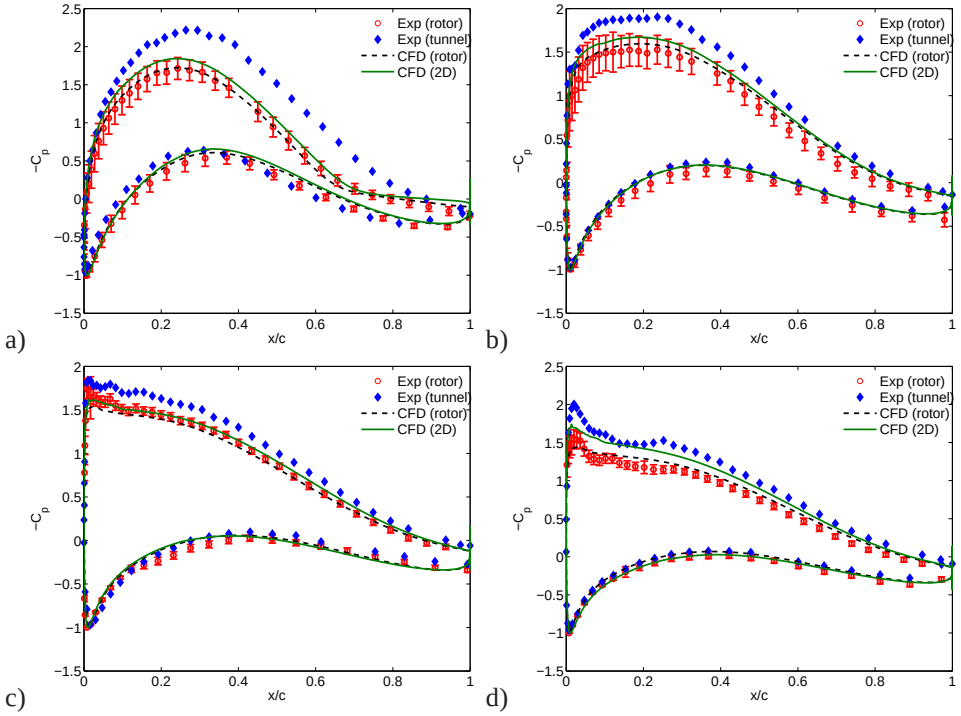

Figure 9.6. C_p distributions for the four different blade sections at $AoA = 4^o$. a) r/R=0.325; b) r/R=0.475; c) r/R=0.750; d) r/R=0.925.

9.5 Conclusion

In this chapter the aerodynamic performance of aerofoils measured on the NM80 wind turbine was investigated and compared to the corresponding aerofoil characteristics deduced in the wind tunnel and as predicted from both 2D aerofoil simulations and full 3D rotor computations using CFD. The combination of field tests, wind tunnel measurements as well as 2D and 3D CFD provides a unique dataset for studying the complex phenomena of 3D aerofoil characteristics.
Initially wind tunnel measurements on four different aerofoil sections were compared to 2D

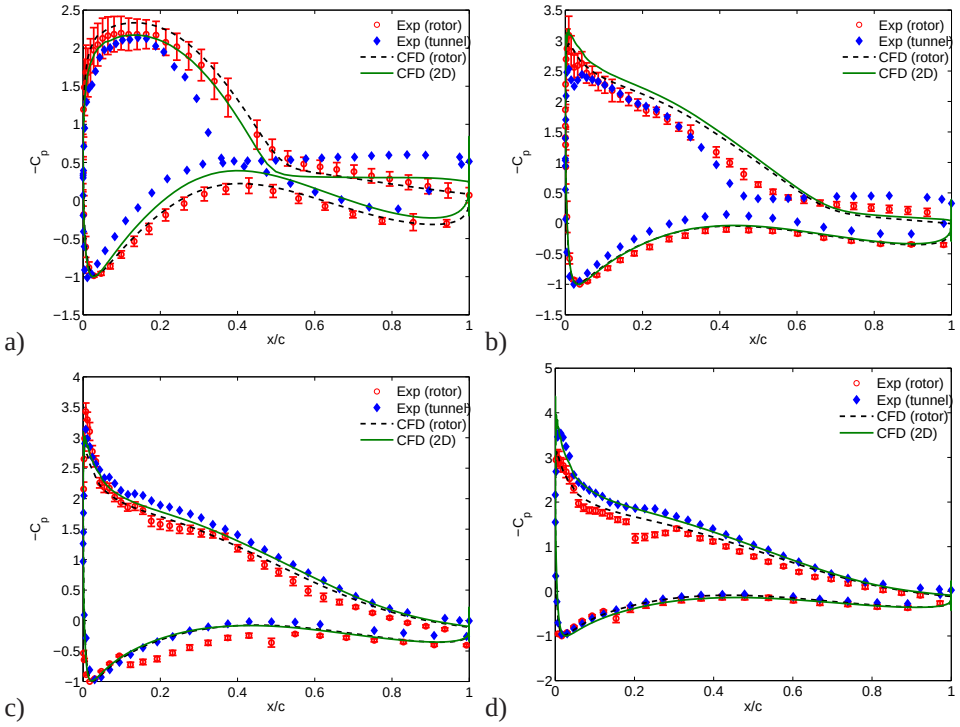

Figure 9.7. C_p distributions for the four different blade sections at different *AoA*. a) r/R=0.325 ($AoA = 14^o$); b) r/R=0.475 ($AoA = 12^o$); c) r/R=0.750 ($AoA = 9^o$); d) r/R=0.925 ($AoA = 10^o$).

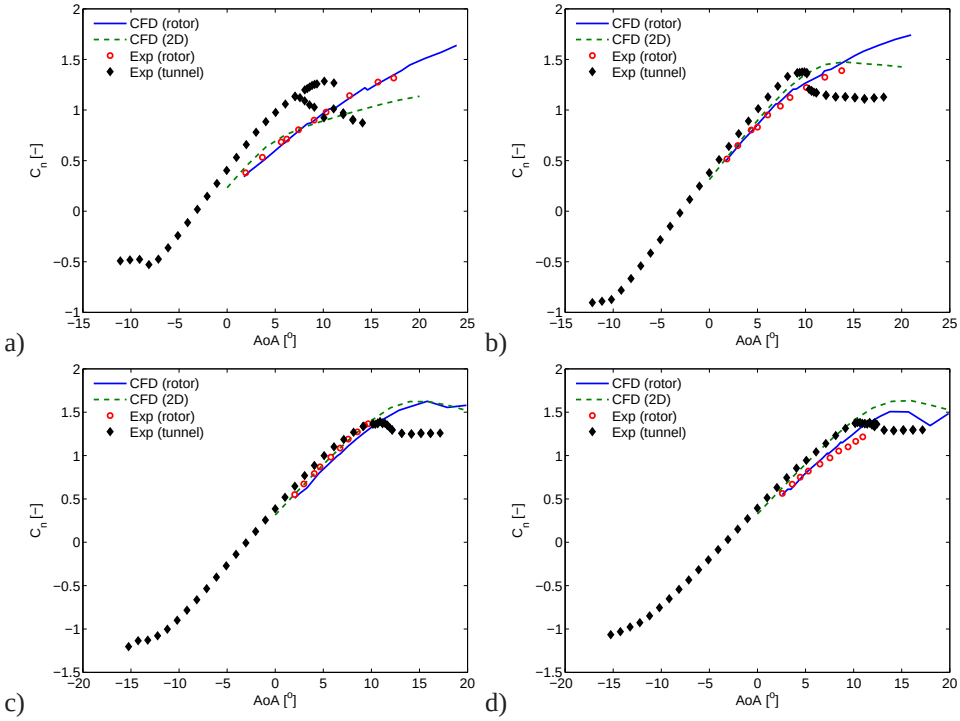

Figure 9.8. C_n polars for the four different blade sections. a) r/R=0.325; b) r/R=0.475; c) r/R=0.750; d) r/R=0.925.

aerofoil simulations. The agreement was found to be fairly good but there were important differences at high angles of attack (AoA). For the thickest aerofoil large difference was found between measured and computed aerofoil performance. These difference was argued to be

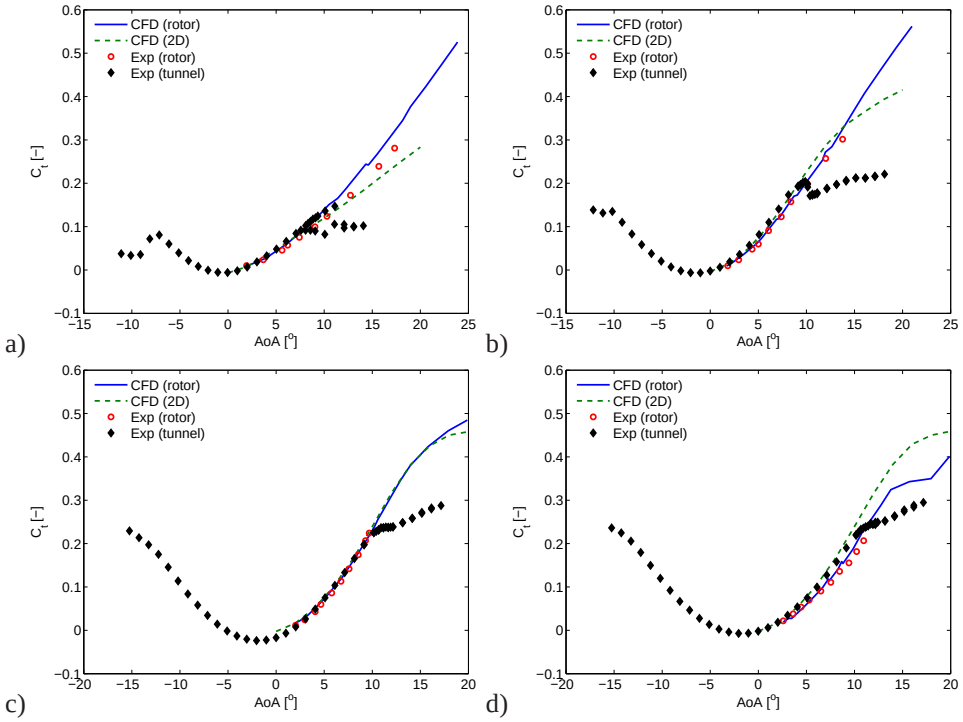

Figure 9.9. C_t polars for the four different blade sections. a) r/R=0.325; b) r/R=0.475; c) r/R=0.750; d) r/R=0.925.

partly due to wall effect in the tunnel but also because it may be inadequate to simulate thick aerofoils at high AoA using 2D CFD.
Secondly a comparison of surface pressure distributions predicted from full rotor CFD and measurements showed rather good agreement at both low and high inflow velocities.
Finally, a comparison of 2D and 3D aerofoil performance was conducted. It was shown that the aerofoil at the inner section (r/R=0.325) experienced augmented performance compared to 2D because of centrifugal and Coriolis forces. For the outermost section (r/R=0.925) it was found that both the overall level and the slope of the normal force coefficient (C_n) curve was lower than in 2D. For the mid span sections the aerofoil characteristics was found to be fairly 2D.

References

[1] J.A. Michelsen. Basis3D - a platform for development of multiblock PDE solvers. Technical report AFM 92-05, Technical University of Denmark, Lyngby, 1992.

[2] J.A. Michelsen. Block structured multigrid solution of 2D and 3D elliptic PDEs. Technical Report AFM 94-06, Technical University of Denmark, 1994.

[3] N.N. Sørensen. *General Purpose Flow Solver Applied to Flow over Hills*. PhD thesis, Technical University of Denmark, 1995.

[4] F.R. Menter. Zonal Two Equation k-ω Turbulence Models for Aerodynamic Flows. *AIAA Journal*, (93-2906), 1993.

[5] F.R. Menter, R.B. Langtry, S.R. Likki, Y.B. Suzen, P.G. Huang, and S. Völker. A Correlation-Based Transition Model Using Local Variables, Part I - Model Formulation. *Proc. of ASME Turbo Expo, Power for Land, Sea and Air. Vienna, Austria*, 2004.

[6] F.R. Menter, R.B. Langtry, S.R. Likki, Y.B. Suzen, P.G. Huang, and S. Völker. A Correlation-Based Transition Model Using Local Variables, Part II - Test cases and In-

dustrial Applications. *Proc. of ASME Turbo Expo, Power for Land, Sea and Air. Vienna, Austria*, 2004.

[7] N. N. Sørensen, A. Bechmann, and F. Zahle. 3D CFD computations of transitional flows using DES and a correlation based transition model. *Wind Energy*, 14, 2011.

[8] P. Fuglsang, I. Antoniou, K.S. Dahl, and H.A. Madsen. Wind Tunnel Tests of the FFA-W3-241, FFA-W3-301 and NACA 63-430 Airfoils. Technical Report Risø-R-1041(EN), Technical University of Denmark, 1998.

[9] Aeroelastic Optimization of MW Wind Turbines. Technical Report Risø-R-1803(EN), Technical University of Denmark, 2011.

[10] Hansen M.O.L. and J. Johansen. Tip studies using CFD and computation with tip loss models. *Wind Energy*, 7, 2004.

[11] J. Johansen and N.N. Sørensen. Airfoil characteristics from 3D CFD rotor computations. *Wind Energy*, 7, 2004.

[12] Shen W.Z., Hansen M.O.L., and Sørensen J.N. Determination of the angle of attack on rotor blades. *Wind Energy*, 12, 2009.

10 Standstill

Author(s): W. Skrzypiński, M. Gaunaa, C. Bak

This chapter describes research on standstill wind turbine blade vibrations carried out within the DANAERO project. The work was divided into experimental and computational investigations. In the experimental part an attempt to extract full airfoil polars from the standstill measurement carried out on the LM 38.8m blade of the NM80 wind turbine at the Tjæreborg site was made. The numerical investigations included preliminary derivation of an engineering model for stall-induced vibrations as well as CFD analysis of vortex-induced and stall-induced vibrations. In the following both parts of the work will briefly be described.

10.1 Experimental investigations

The standstill measurements were carried out twice: on August 19th from 16:50 till 17:40, and on September 1st, from 16:20 till 17:00. In order to acquire the data, the turbine was set to standstill with one of the blades set in vertical position with its tip facing up. Then, the turbine was slowly yawed at a rate of 0.3 deg./sec. The surface-pressure distributions used for calculating the loading were recorded at 4 sections of the blade. Each of the 4 sections was equipped with 64 pressure taps. Locations of the sections together with their names are listed in Table 10.1.

This chapter deals exclusively with the data obtained at section 5A, on August 19th. At that

Section name	Distance from the tip [m]
3A	27
5A	21
8A	10
10E	3

Table 10.1. Names and positions of blade sections with surface-pressure-taps

time, the rotor approximately made two yaw revolutions at standstill. September 1st was excluded because preliminary analysis revealed that the data obtained on this date was of insufficient quality. Section 5 was chosen because the measurement equipment at sections 8 and 10 was of lower resolution. That was because the equipment was primarily set up to measure while the turbine operated. During operation, the Pitot tubes and surface-pressure sensors at the outer part of the blade were subjected to higher wind speeds due to rotation. Therefore, their resolution was lower than that at section 5. On the other hand, section 3, which is the innermost section of the blade, was subjected to 3-D effects during standstill more than the other sections were. Therefore, choosing section 5 for standstill analysis was a compromise between measurement resolution and influence of the 3-D effects. Moreover, on August 7th, the measurement system experienced a failure which caused a permanent malfunction of the surface-pressure measurement equipment at sections 8 and 10. Even though a successful attempt to partly restore the corrupted data was made [1] the use of restored data from sections 8 and 10 would impose additional uncertainty.

10.1.1 Experimental setup and data storage

The experimental setup is extensively described by Bak et al.[1]. The layout of the pressure taps at section 5 is presented in Figure 10.1, together with the profile geometry. 40 sensors around the leading edge had resolution of 2.5 psi while the remaining sensors had resolution of 1 psi. The sensors of lower resolution are marked with red. The profile used at this section

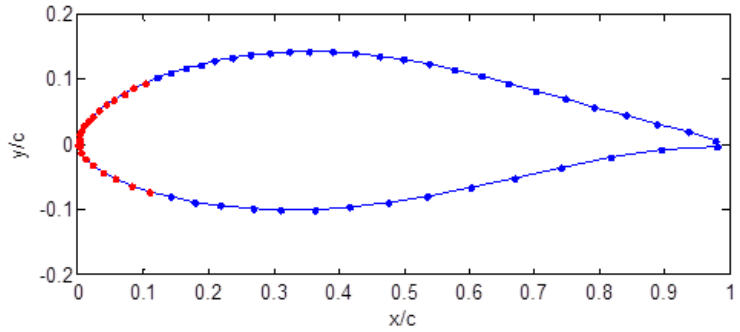

Figure 10.1. The surface-pressure tap layout at blade section 5

was NACA 63424. The gauge pressure values at all the sensors were recorder by Scanivalve system at the frequency of 100 Hz. Some of the sensors malfunctioned during the standstill which showed during analysis of the pressure-distribution time series. The data related with these sensors was interpolated linearly based on the values from the neighbouring sensors. The angle of attack, necessary for the calculation of the polars, was determined in the following way:

$$\alpha = 90^o - \theta - \tau + \varepsilon \tag{4}$$

where θ is the pitch angle, τ is the twist at section 5, and ε is the yaw misalignment. The yaw misalignment is the difference between the wind and yaw directions. The yaw misalignment angle was calculated in three alternative ways:

- Measurement of yaw position of the rotor and wind direction at the nacelle
- Measurement of yaw position of the rotor and wind direction at the met mast
- Measurements from the Pitot tubes mounted at the leading edge at sections 5 and 8. The data from both tubes was analyzed in order to limit potential error in case of a malfunction of one of the tubes.

Calculating the polars also require determination of the wind speed. This was done in five alternative ways: The wind speed was measured at the nacelle, met mast, by the Pitot tubes at sections 5 and 8, and calculated based on the surface pressure at the stagnation point at section 5. The angle-of-attack and wind-speed time series from the Pitot tubes were only relevant in the relatively narrow operational region of the Pitot tubes, i.e. approx. between -20 and 20 degrees of the inflow angle relative to the tubes.

10.1.2 Angle-of-attack measurement

The angle-of attack time series was calculated in four alternative ways. The results showed that the Pitot tube at section 5 measured the angle of attack incorrectly. This was probably due to the tube's hoses being blocked. During processing of all the data, parts of the time series where sudden changes of the angle of attack occurred were removed together with a safety margin in order to exclude potentially unsteady loading conditions. The time series are presented in Figure 10.2. A sign of edgewise blade vibration may be visible in the time series from the nacelle at approx. 150 degrees of the angle of attack, between samples $3 \cdot 10^4$ and $3.5 \cdot 10^4$. A similar signal was present in the edgewise root bending moment (MX) time series. The jump in the time series visible approx. between samples $5 \cdot 10^4$ and $5.5 \cdot 10^4$ is due to a pitch change.

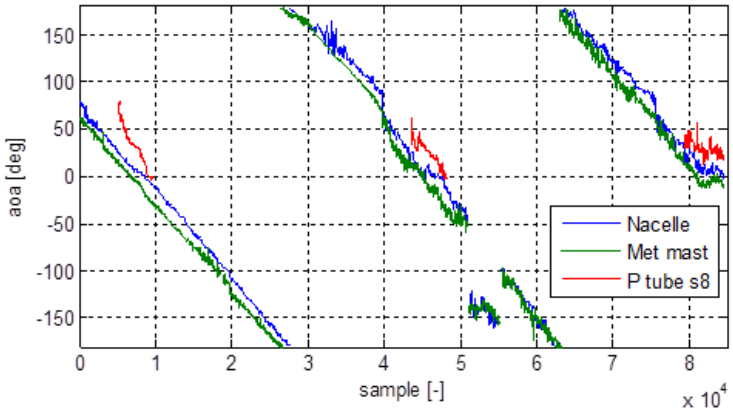

Figure 10.2. Time series of angle-of-attack at section 5

Parts of the time series corresponding to the pitch being in motion were removed together with a safety margin, in order to exclude potentially unsteady loading.
The measurement carried out by the Pitot tube at section 8 was treated as a source of additional information, and not used for the load computation, due to its limited angle coverage. Both the nacelle and met-mast time series were potentially interesting source of information. On one hand, the met mast is at certain distance from the turbine. Therefore, it unfortunately looses some information about the flow around the turbine. On the other hand, the measurement made on the nacelle was influenced by the presence of the nacelle itself and the blade. Both angle-of-attack time series were corrected by applying an offset, in order to achieve polars closest to the reference polars extracted from measurements of the same profile, performed in the LM Wind Power wind tunnel [2]. The time series from the nacelle appeared as more accurate since a lower offset value needed to be applied in order to meet the reference polars: 2 deg offset was applied to the nacelle time series while 21 deg offset was applied to the met-mast time series in order for the resulting polars to meet the reference.

10.1.3 Wind-speed measurement

Wind speed was measured in five alternative ways: at the nacelle, met mast, by the Pitot tubes at sections 5 and 8, and calculated based on the dynamic pressure at the stagnation point at section 5. Resulting time series are presented in Figure 10.3.
In order for the figure to be clear, the time series were plotted only up to sample $5 \cdot 10^4$. Again, the measurements made by the Pitot tubes were only considered a source of additional information due to their limited angle-of-attack coverage. The Pitot tube at section 5 seemed to record wind speed correctly, despite the faulty angle-of-attack measurement. Pressure-distribution time series had been processed before the stagnation-pressure time series was extracted. This was done by first removing insubstantially high instantaneous pressure peaks, and second, by applying a low-pass filter. The filter applied was Butterworth of order 10 and cut-off frequency of 1 Hz. Analysis of polars normalized by means of different wind-speed time series indicated that the wind speed measured at the nacelle was the most reliable. As it was mentioned in the previous section, the data from the nacelle was also used for determination of the angle-of-attack time series. As seen the stagnation-point time series was not in agreement with any other time series. This indicated that the pressure measurement may have been of poor quality. This, in turn could be caused by the measurement equipment being set up to work in the operational region where the flow velocities are significantly higher than in standstill. In such a case, when measuring at standstill, the signal-to-noise ratio may have been too low to record substantial data.

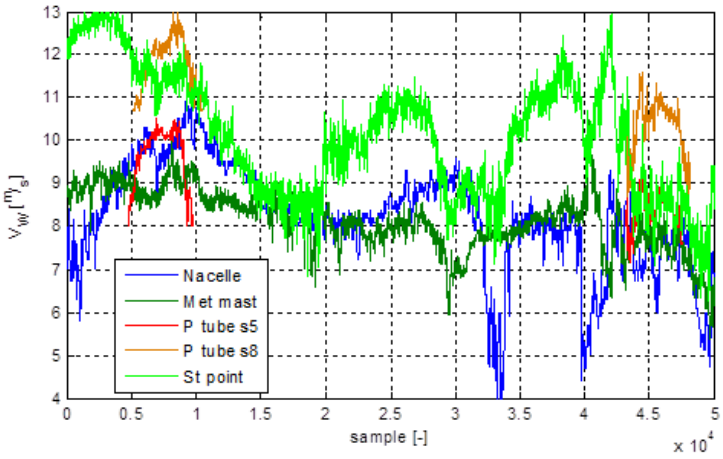

Figure 10.3. The wind-speed time series obtained in the 5 alternative ways

10.1.4 Pressure-distribution measurement

Measured pressure distributions were compared with XFOIL computations of the same profile at the same Reynolds number. XFOIL computations were carried out with both free and forced transition models. In order to validate the XFOIL computations, the polars resulting from the XFOIL computations were compared with results of the wind-tunnel measurements performed by LM Wind Power [2]. The comparison was made in the angle-of-attack region from -6 to 19 deg. However, XFOIL forced-transition polars were unavailable in the angle-of-attack region below -1 deg. Pressure distributions from the aforementioned wind-tunnel measurements were unfortunately unavailable as well. The comparison of the polars is presented in Figures 10.4 and 10.5 The first two entries in both legends refer to the measurements of the clean profile

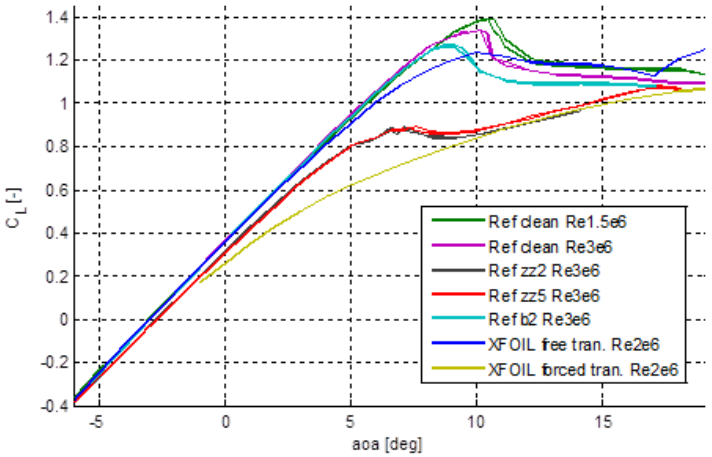

Figure 10.4. Comparison of the XFOIL and measured lift coefficients

at Reynolds numbers of $1.5 \cdot 10^6$ and $3 \cdot 10^6$, respectively. The third entry corresponds to the measurement on the profile with zigzag tape of 0.4 mm thickness placed at 2% chord on the suction side. The fourth entry to zigzag tape of 0.4 mm thickness placed at 5% chord on the suction side and 10% chord on the pressure side. The fifth to bump tape of 0.1 mm thickness placed at 2% chord on the suction side. The last two entries correspond to the XFOIL predictions with free and forced transition models, respectively. The XFOIL free-transition lift

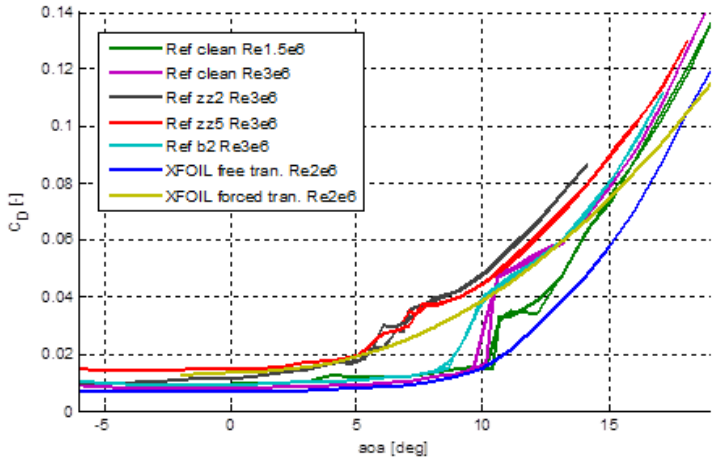

Figure 10.5. Comparison of the XFOIL and measured drag coefficients

coefficient corresponds well with the lift coefficients from the measurements on the clean airfoil and the airfoil with the bump tape installed. The XFOIL forced-transition lift coefficient corresponds well with the measurements on the airfoil with the zigzag tape installed, in the angle-of-attack region above 10 deg. The XFOIL free-transition drag coefficient corresponds well with the measurements on the clean airfoil and the airfoil with the bump tape installed, in the angle-of-attack region below 10 deg. The XFOIL forced-transition drag coefficient corresponds well with the measurements on the airfoil with the zigzag tape installed, especially in the angle-of-attack region below 5 deg. Overall, the polars compared satisfactorily, and therefore the comparison verified the XFOIL computations. This, in turn, made XFOIL a reliable reference for the measured pressure distributions. Figure 10.6 shows the measured pressure dis-

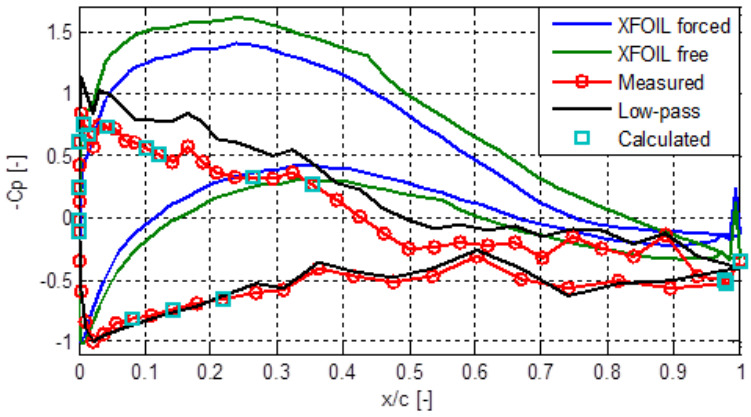

Figure 10.6. The measured pressure distribution at approx. 5 deg. of angle of attack, compared with the XFOIL computations, plotted as a function of the normalized x coordinate

tributions both before and after the processing. The latter distribution was processed with the low-pass Butterworth filter of order 10 and cut-off frequency of 1 Hz. In both distributions the faulty points were linearly interpolated. The measured distributions were compared with the XFOIL computations of the same profile at Reynolds number of $2 \cdot 10^6$. Two XFOIL distributions are presented above, one corresponding to free and one to forced transition model. Also, the measured angle of attack was subjected to the low-pass filter of the same characteristic, in order to remove high frequency variations. The same pressure distributions are presented as a function of the normalized y coordinate in Figure 10.7 The comparison of the measured and

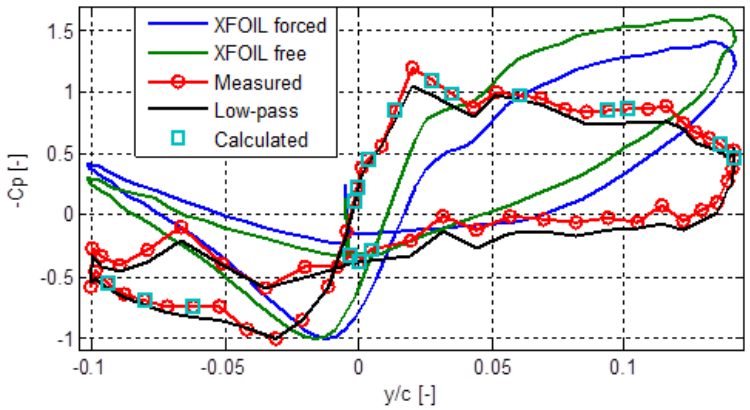

Figure 10.7. The measured pressure distribution at approx. 5 deg. of angle of attack, compared with the XFOIL computations, plotted as a function of the normalized y coordinate

computed pressure distributions was unfortunately unsatisfactory. That was because significant differences in the distribution shapes were present. Moreover, the difference between the pressure distributions coming from the two XFOIL computations appears significantly smaller than the difference between the measured distribution and either of the two XFOIL distributions. To shed more light on this issue, the offset between the XFOIL and measured pressure-distribution mean values was analyzed. Another analyzed parameter was the ratio between the integrated pressure distributions (XFOIL/measured). These two parameters are presented as functions of the angle of attack in Figures 10.8-10.9. If either the offset or the ratio appeared as constant, it would imply that some sort of systematic error had been present during the measurement.

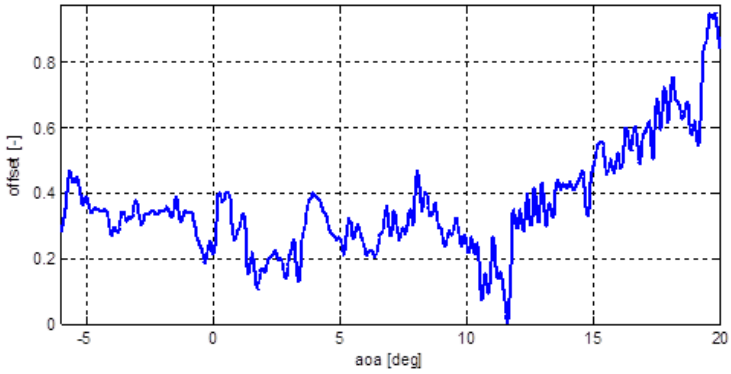

Figure 10.8. The offset between the measured and XFOIL pressure-distribution mean values

Unfortunately, both the offset and the ratio show relatively high variation in the angle-of-attack region between -1 and 20 deg. The offset varies approx. from 0 to 1. The ratio varies approx. from 0.4 to 2. In the angle-of-attack range from -6 to -1 deg., it varies from -10 to 9, what is not shown in the figure above.

10.1.5 Comparison of the polars

In order to obtain the lift and drag coefficients, the following steps were taken:

- Normal and tangential loads were calculated and normalized

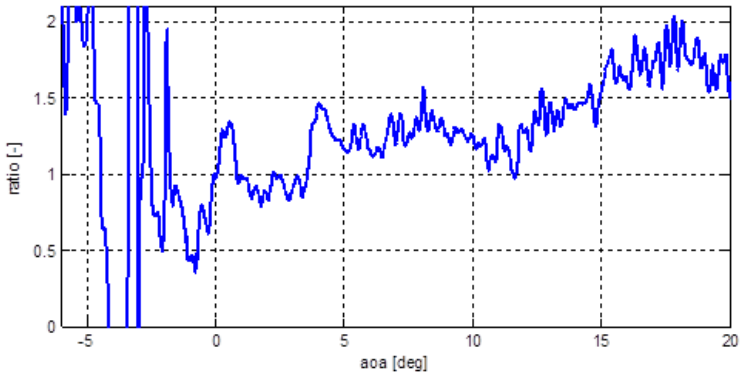

Figure 10.9. The ratio between the measured and XFOIL pressure-distribution integrated values

- Angles of attack were calculated as in equation 4
- The normal and tangential load coefficients were projected according to the angle-of-attack values, to obtain the lift and drag coefficients
- The lift and drag coefficients were binned because the measurement involved two yaw revolutions of the turbine

Figures 10.10-10.12 present the lift and drag coefficients, normalized by the dynamic pressure values obtained in two ways:

- measured at the stagnation point of the profile at section 5 (labelled "SEC")
- calculated according to the wind-speed measurement at the nacelle (labelled "NAC")

Moreover, figures 10.11 and 10.12 show a comparison with the two reference sets of polars coming from the wind tunnel measurements, previously presented in figures 10.4 and 10.5.

Unfortunately, the resulting polars presented in figures 10.10- 10.12 are of poor quality. The

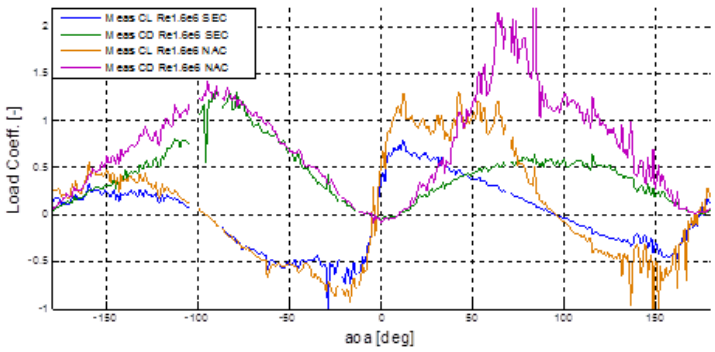

Figure 10.10. The measured polars, normalized by the dynamic pressure values obtained in the two alternative ways

first issue is that neither the lift nor the drag curves overlap with any of the reference curves. This could actually have been foreseen by looking at the wind-speed time series presented in Figure 10.3. There, it is clear that the wind-speed time series measured on the nacelle and at blade section 5 differ significantly. The most significant difference in the lift coefficient is visible approx. between 0 and 100 deg. The drag curves differ most significantly approx.

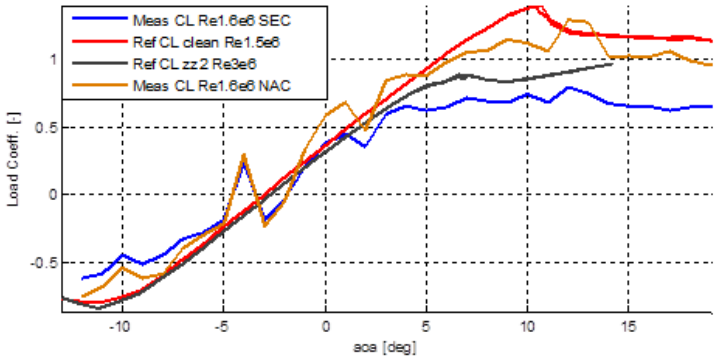

Figure 10.11. The measured lift coefficients, compared with the reference wind-tunnel results.

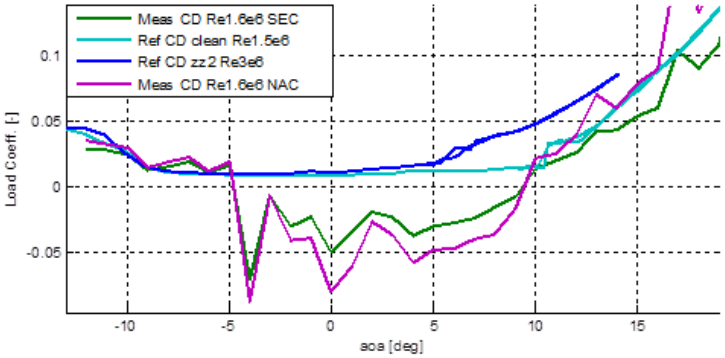

Figure 10.12. The measured drag coefficients, compared with the reference wind-tunnel results

between 20 and 150 degrees. However, both the lift and drag curves normalized by means of the wind speed read on the nacelle are especially uncertain in the angle-of-attack region around 90 deg. The reason is that around this angle the measurement equipment on the nacelle was in the wake of the blade. Moreover, none of the lift and drag curves are particularly smooth as was expected. What is particularly visible in Figure 10.12 is that the drag coefficient becomes negative in the angle-of-attack region between -5 and 10 deg. This is clearly unphysical. In principle, such a problem could arise from incorrect calculation of the angle of attack. Then, at an angle thought of as zero (and, in fact, being non-zero), normal-to-chord force component (CN) could decrease the apparent drag value. However, it was verified that the problem did not arise from the incorrect angle-of-attack computation. This is because the tangential-to-chord force component (CT) in vicinity of the zero angle of attack does not change in sign (see Figure 10.15). Therefore, offsetting the angle of attack could not solve the problem which is probably caused by the inaccurate pressure-distribution measurement.

10.1.6 Error analysis

Here, further analysis of the polars is presented. It was done in order to find the source of their poor quality, and to propose changes in the experimental setup that would improve result quality in the future. The aim was to learn to which extent the following factors decreased the quality of the results:

- Inaccurate measurement of the wind speed

- Inaccurate measurement of the angle of attack
- Inaccurate measurement of the pressure distribution

The first was analyzed by plotting CL/CD. The reason was that any inaccuracy in the wind-speed measurement would be cancelled out while plotting the lift-to-drag ratio. Therefore, such a curve should match the reference better than the CL or CD curves alone. Such approach was previously proposed by Timmer [3]. It should also be pointed out that CL/CD curve was not expected to fit the references well in the angle-of-attack region between -5 and 10 deg, since CD is negative in this region. The CL/CD curve is presented in Figure 10.13 together with the references: As seen the measured CL/CD curve fits one of the reference curves well

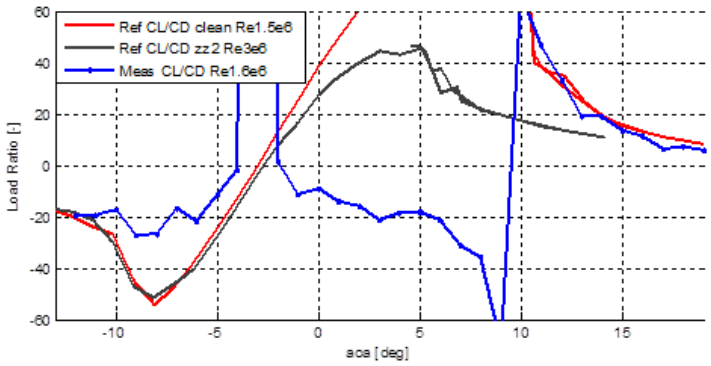

Figure 10.13. The measured CL/CD curve, compared with the reference wind-tunnel measurements

in the angle-of-attack region between 10 and 19 deg, better than the CL curve alone. On the other hand, the CL/CD curve does not fit either of the references in the angle-of-attack region between -13 and -5 degrees. Actually, it shows a worse fit than either the CL or CD curves alone. In general, it does not seem that the CL/CD curve fits any reference significantly better than the CL or CD curves alone. Therefore, it does not seem that inaccurate measurement of the wind speed was the major source of error in this experiment. The measured CN and CT curves together with the reference curves are presented in figures 10.14 and 10.15.

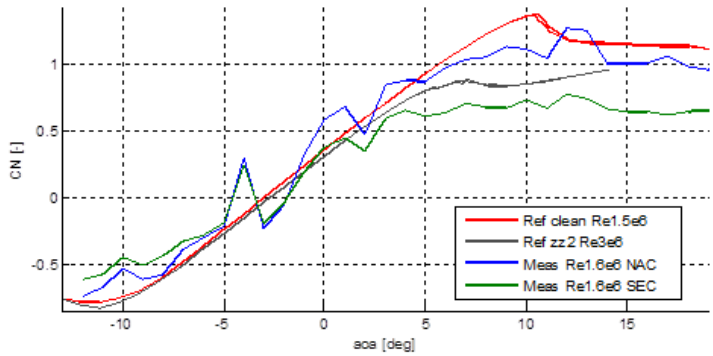

Figure 10.14. The measured CN curves, compared with the reference wind-tunnel measurements

If the angle-of-attack measurement was the main source of error, the measured CN and CT curves should resemble the reference curves better than the CL and CD curves. The reason is that CN and CT are obtained directly from the measured pressure distributions, independently

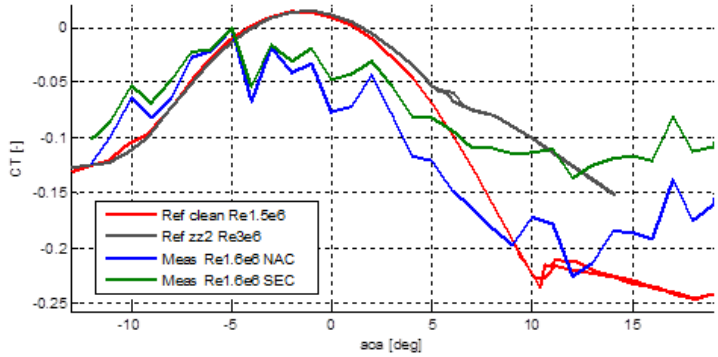

Figure 10.15. The measured CT curves, compared with the reference wind-tunnel measurements

of the angle of attack while CL and CD are functions of the angle of attack. Therefore, while the CL and CD curves would change in shape due to incorrect angle of attack measurement, the CN and CT curves would only offset in horizontal direction. In other words, incorrect measurement of the angle of attack would result in CL and CD being further from the reference curves than the CN and CT curves would be. However, CN and CT do not seem closer to the references than CL and CD. The last attempt to observe any influence of incorrect wind speed or angle of attack measurements was to plot CN/CT: Using CN/CT for the comparison removes both

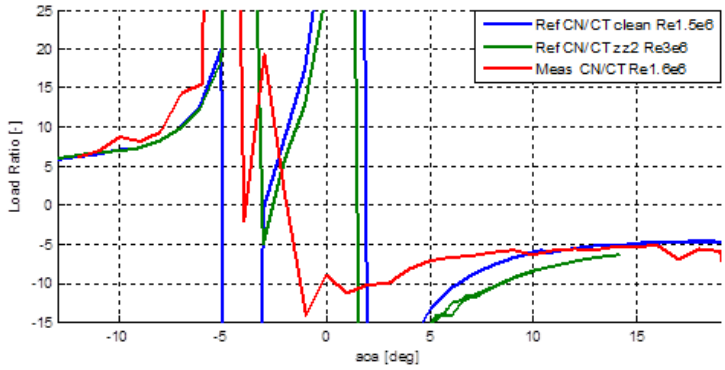

Figure 10.16. The measured CN/CT curves, compared with the reference wind-tunnel measurements

the influence of incorrect wind speed and angle of attack measurements. Using CN/CT instead of CL/CD showed that CN/CT was closer to the reference in the angle-of-attack region below -5 deg. Using CN/CT instead of CN and CT showed that CN/CT was slightly closer to the reference, especially in the angle-of-attack region above 10 deg. However, the differences were far from pronounced. The outcome of the aforementioned comparisons together with the fact that CL and CN seem to compare better with their references than CD and CT do, in the attached-flow region, indicate that the error to a large extent lies in the pressure measurement. In other words, CL and CN are of significantly higher magnitude in the attached-flow region than CD and CT are. Therefore, the signal-to-noise ratio of CL and CN might have been higher. Poor signal-to-noise ratio would also explain the non-smooth polars.

10.2 Numerical investigations

Wind turbine blade vibrations at standstill conditions were also investigated through numerical simulations within the DANAERO project. These investigations included vortex-induced and stall-induced vibrations. Thus, it was investigated whether the stand still vibrations are vortex-induced, stall-induced or a combination of both types. The work comprised analysis based on engineering models and Computational Fluid Dynamics. Two-dimensional, three-degree-of-freedom, elastically-mounted-airfoil engineering models were created. These models aimed at investigating the effect of temporal lag in the aerodynamic response of an airfoil on the aeroelastic stability limits. The motivation for this work was to investigate whether the assumption of quasi-steady aerodynamics in deep stall made in state of the art aeroelastic codes, if inaccurate, may lead to inaccurate predictions of blade standstill vibrations. Further, two- and three-dimensional CFD computations on a DU96-W-180 airfoil were carried out around 25 and 90 degrees angle of attack. These included non-moving, prescribed-motion and elastically-mounted airfoil suspensions. Moreover, analysis of the dynamic lift and drag resulting from 2D and 3D CFD computations carried out around 25 degrees angle of attack was carried out. The aim was to study the mechanisms involved in both types of vibrations as well as to learn about the conditions corresponding to the onset of both. The CFD computations were carried out with EllipSys2D and EllipSys3D Navier-Stokes solvers developed by Michelsen [4, 5] and Sørensen [6, 7]. Elastically mounted airfoil computations were performed with an EllipSys add-on for structural computations developed by Heinz et al. [8]. Detailed description of the parameter values used in the CFD computations as well as in the structural model is presented in [9].

10.2.1 Engineering elastically-mounted-airfoil aerodynamic model

The effect that time lag in the aerodynamic lift, drag and moment has on the aeroelastic stability limits was investigated by means of an engineering elastically-mounted-airfoil model. This analysis is described in more detail by Skrzypiński [9] as well as by Skrzypiński and Gaunaa [10, 11]. The current setup of the 2D 3-DOF elastically-mounted-airfoil model is presented in Figure 10.17. C is the chord line, AA is the aerodynamic axis, and EA is the elastic axis (hinge point). F_X and F_Y are the aerodynamic force components applied at AA in x and y directions, respectively. F_Θ is the aerodynamic moment applied at AA. Θ_g is the angle between C and the line (C') through EA and the center of gravity (CG). C is parallel with the x axis when the profile is in the equilibrium without the aerodynamic forces involved. The three equations of motion

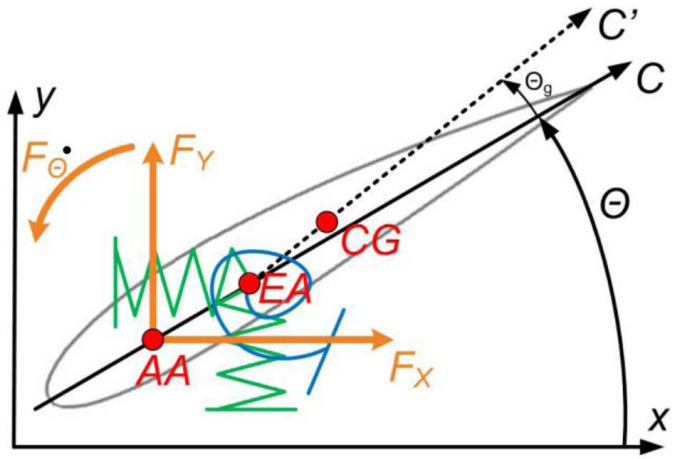

Figure 10.17. 2D 3-DOF elastically-mounted-airfoil model

used to govern the aforementioned model are described in detail in [9, 11]. The dynamic lift coefficient was calculated as the linearised static lift coefficient at an effective angle of attack.

$$C_L^{lin} = C_L^0 + \frac{dC_L^0}{d\alpha}\alpha_E^1 \tag{5}$$

where C_L^0 is the lift coefficient at the equilibrium state. Further, α_E^1 is a small perturbation of the effective angle of attack from its equilibrium value. A more detailed description of the utilized equations including the equations for the dynamic drag and moment coefficients is presented in [9, 11]. The work also included a study of the significance of the added mass terms from Jones' thin airfoil theory [12] in the equations for the aerodynamic forces.

In the study, different amounts of temporal lag were imposed on the dynamic aerodynamic response of the model. The comparison presented in Figure 10.18 shows the model's damping ratios corresponding to its edgewise oscillation for three different amounts of the temporal lag. Note that when the damping ratio was negative, the model experienced negative aerodynamic damping and therefore increasing vibrational amplitude. The three amounts of temporal lag respectively correspond to quasisteady aerodynamic response, aerodynamic response of a thin airfoil (No. 1) as described by Jones [12], and an arbitrary response being slower than the response of a thin airfoil (No.2). As it is seen in Figure 10.18, the study showed that even a

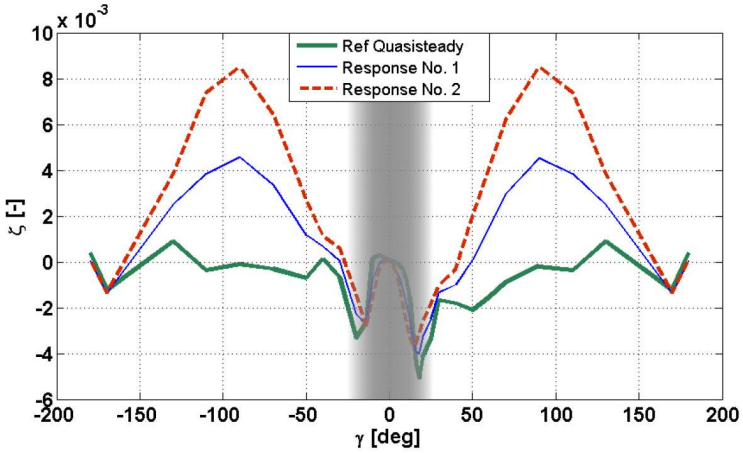

Figure 10.18. Damping ratio of the edgewise oscillation of the engineering elastically-mounted-airfoil model; three different amounts of time lag in the full aerodynamic response with Quasisteady being the fastest and No.2 being the slowest.

relatively low amount of time lag in the dynamic aerodynamic response of the model significantly increased the model's aerodynamic damping. This information, combined with the fact that state of the art aeroelastic codes assume quasisteady aerodynamics in deep stall, indicates that these aeroleastic codes may inaccurately predict aerodynamic damping in deep stall, and therefore inaccurately predict stall-induced vibrations at standstill conditions.

10.2.2 CFD investigations of vortex-induced vibrations around 90 degrees angle of attack

Locked-in vortex induced vibration is a potential threat to large wind turbine blades at standstill conditions. The part of the present work described in this section and in more detail in [9, 13] was a study of vortex-induced vibrations of the DU96-W-180 airfoil CFD model. The present study included 2D and 3D unsteady CFD computations. These included computations on non-moving, prescribed motion and elastically mounted airfoil suspensions. Stationary vortex shedding frequencies corresponding to the 2D and 3D computations were obtained by performing

a frequency analysis of the loading on the non-moving airfoil models. In the prescribed motion computations the airfoil was forced to oscillate in the direction of the chord line. The elastically mounted airfoil computations were made with both one and three degrees of freedom of movement. It is common to resolve such flows by means of computationally expensive 3D DES simulations. The motivation for including 2D computations in the present work was to investigate whether relevant flow characteristics may be captured by 2D computations. This could be beneficial because of the high computational efficiency of such computations compared to 3D DES. A DU96-W-180 non-moving airfoil model subjected to a flow at 90 degree inflow angle experienced aerodynamic force oscillations in the chordwise force of frequency corresponding to the Strouhal number of this system. To illustrate that the oscillations were caused by the vortex shedding, two snapshots of the 3D flow are presented in Figure 10.19. The figure presents vorticity magnitude. Dark areas correspond to high values. In the snapshot on the left side, a vortex is being shed off the leading edge. The vortex is marked with a circle. In the snapshot on the right side, a vortex is being shed off the trailing edge - also marked with a circle. This was confirmed by analysis of the animation showing pressure variation. Vortex-induced vibration is

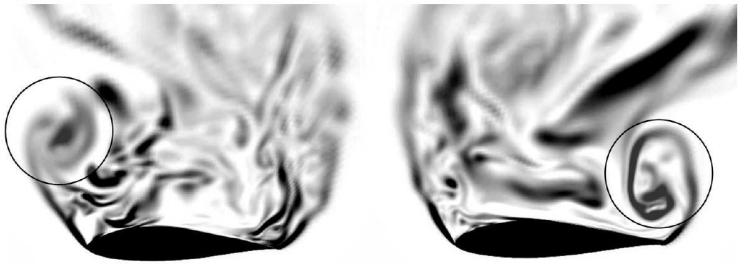

Figure 10.19. Snapshots presenting vorticity magnitude of the 3D flow around the DU96-W-180 airfoil at 90 degree inflow angle

by nature an aeroelastic problem. However, here an attempt was made to identify the aeroelastic stability limits by means of prescribed motion computations where the airfoil was subjected to forced oscillations along the chord line. The mean power was extracted from the computations. When the power was positive, the flow fed energy to the oscillating system. A number of computations were made at different vibration periods, T. Then, the mean dimensionless power was plotted as a function of the dimensionless vibration period $T^* = TV/c$. The dimensionless mean power was obtained by normalization of the mean power with density, chord length, absolute wind speed, vibrational amplitude and period:

$$P^* = \frac{T}{\rho c A V^2} \bar{P} \tag{6}$$

Figure 10.20 presents the results of the 2D RANS and 3D DES computations with three curves showing the dimensionless power, P^*, as a function of the dimensionless forced-oscillation period, T^*, of the DU96-W-180 model. Each of the curves corresponds to simulations carried out at a specific A^*/T^* ratio. The reason was that A^*/T^* - where A^* is the dimensionless oscillation amplitude - can be thought of as the level of perturbation imposed by the airfoil motion on the flow. If A^* was constant in a set of computations, then such a level of perturbation would grow with f^*. Then, computations with relatively high oscillation frequency would drive the vortex shedding and create the lock-in more likely than computations with low oscillation frequency. The dimensionless vortex shedding period of the non-moving airfoil in the 2D computations was $T^* = 7.7$. As the figure shows, the dimensionless power in all three cases increased to a peak with positive sign when the oscillation period reached 7.7. The power value also grew in the surrounding of the peak point. Note that the higher the A^*/T^* ratio was, the wider the T^* band in which the power grew was. The existence of this band and its growth with A^*/T^* indicate the existence of the so called lock-in in which the vortex shedding frequency follows

the vibrational frequency in a relatively narrow frequency band causing amplification of vibrations. All this indicated that an actual DU96-W-180 airfoil with the natural frequency of the chordwise mode close to the frequency of vortex shedding could experience the mechanism of lock-in and suffer from vortex-induced vibrations. The results presented in Figure 10.20

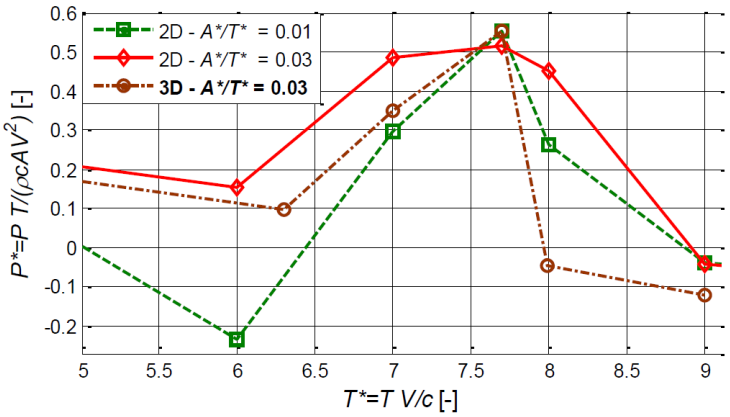

Figure 10.20. Dimensionless power related to prescribed oscillation of the DU96-W-180 profile at 90 degree angle of attack, oscillating perpendicular to the free stream; results of the 2D RANS and 3D DES computations

were verified by extracting force-displacement plots which indicated the existence of the resonance in the system, and later by performing elastically-mounted-airfoil computations which confirmed the results presented in Figure 10.20. Dimensionalization of the dimensionless numbers used in the computations indicated that large MW wind turbine blades could suffer from vortex-induced vibrations at moderate wind speeds. However, in order to verify this conclusion future work should be carried out, e.g. including computations on 3D blades taking into account their twist and taper as well as different inflow conditions.

10.2.3 CFD investigations of vortex-induced and stall-induced vibrations in stall

This section presents an analysis of 2D and 3D non-moving, prescribed motion and elastically mounted CFD computations of the DU96-W-180 airfoil in the angle of attack region potentially corresponding to the highest risk of stall-induced vibrations. The computations aimed at investigating the mechanisms of both vortex-induced and stall-induced vibrations. Like in the preceding section, the aeroelastic stability limits were investigated by calculating the mean dimensionless aerodynamic power in the prescribed motion computations. In order to facilitate the process of finding the angle-of-attack region of the highest risk of stall-induced edgewise vibrations prior to performing CFD computations, an equation for aerodynamic damping by Gaunaa and Larsen [14] was applied to the aerodynamic characteristics of the DU96-W-180 airfoil obtained experimentally by Timmer and van Rooij [15] and Timmer [3], indicating where the vibrations could emerge. It was decided that 26 degrees and 24 degrees were the angles of attack investigated further in 2D and 3D, respectively. Despite the similarities between the 2D and 3D computations presented in the preceding section, at the inflow angles considered in the present section, 2D and 3D computations returned completely different results. After analysis and discussion of these results, a decision was made that 3D computations are more reliable in the present case because of the three-dimensional flow characteristics.

Figure 10.21 presents the P^* curve corresponding to the 3D prescribed motion computations of the DU96-W-180. The power appeared positive in two T^* regions. The first was approximately between 1 and 15 while the second was approximately above 44. The first region contained relatively high values of P^* with steep rise and fall. The underlying values of T^* contained the

dimensionless period of stationary vortex shedding. These facts indicated that the increase in power was associated with vortex shedding. The same kind of vibrations is shown by both 2D and 3D prescribed motion and elastically mounted airfoil CFD simulations of the same airfoil at 90 deg angle of attack, presented in the preceding section. The second region contained T^* values larger than the frequency of stationary vortex shedding by an order of magnitude. This indicated the presence of stall induced vibrations. However, dimensionalization of the results indicated that if such vibrations occurred on a modern wind turbine blade, the associated wind speed would be far from any realistic regime, i.e. 88 m/s. The thick vertical dotted line in Figure 10.21 shows the value of T^* corresponding to the wind speed of 50 m/s. These results were verified by performing computations on the elastically mounted airfoil.

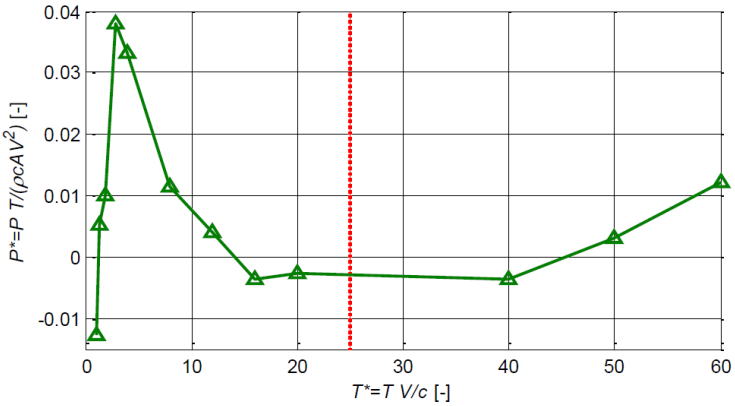

Figure 10.21. Dimensionless power related to prescribed motion 3D CFD simulations of DU96-W-180 at 24 deg angle of attack; oscillating in chordwise direction

10.2.4 Modeling of unsteady airfoil aerodynamics in stall

In one of the preceding sections, it was shown that even a relatively low amount of temporal lag in the aerodynamic response of an airfoil model in deep stall may dramatically decrease the range of angles of attacks at which the aerodynamic damping of this model is negative. Under the assumption that the actual aerodynamic response of airfoils in deep stall is slower than quasi-steady this indicates that present aeroelastic codes may over-predict deep stall standstill vibrations. To analyze this issue further, the focus of the work presented in this section was on determining the amount of temporal lag of an airfoil in deep-stall. 2D and 3D prescribed motion CFD computations were respectively carried out at 26 and 24 degrees angle of attack. Temporal lag of the aerodynamic response was quantified by means of the aforementioned engineering aerodynamic model described in detail in [9, 11]. In the model, the parameters were adjusted to match the dynamic lift and drag coefficient loops obtained during the CFD simulations. Then, these parameters were considered representative of the respective CFD simulations. Note that the angles of attack used in the present work were defined with respect to the flow velocity relative to the airfoil. The motion of the airfoil was therefore taken into account. In Figure 10.22, the following curves concerning the dynamic lift coefficient loops of the 2D CFD simulations are presented:

- Static lift coefficient resulting from the time-marching 2D CFD with the non-moving DU96-W-180
- Dynamic lift coefficient loop resulting from the prescribed motion 2D CFD
- Dynamic lift coefficient loop modeled to match the dynamic 2D CFD response using the method from [9, 11], based on the 2D CFD polars

- Dynamic lift coefficient loop modelled assuming inviscid response using the method from [9, 11], based on the 2D CFD polars
- Dynamic lift coefficient loop modelled using Beddoes-Leishman type [16, 17] dynamic stall model, based on the 2D CFD polars

The direction of the presented loops was clockwise. The results showed that the dynamic-lift response resulting from prescribed motion 2D CFD was slower than the one modelled using [9, 11] and the inviscid parameters for the temporal response. Neither the dynamic lift coefficient loop modeled using the Beddoes-Leishman type dynamic stall model [16, 17] resembled that of the prescribed motion CFD computations. The approximate dynamic 2D CFD response was modeled by tuning the parameters in the aforementioned engineering model. However, the exact shape of the CFD response was impossible to obtain. The dynamic lift coefficient loop resulting from the prescribed motion 2D CFD was averaged over 20 periods of oscillation in order to decrease the influence of the higher-frequency fluctuations associated with vortex shedding. In Figure 10.22, the following curves concerning dynamic lift coefficient loops of

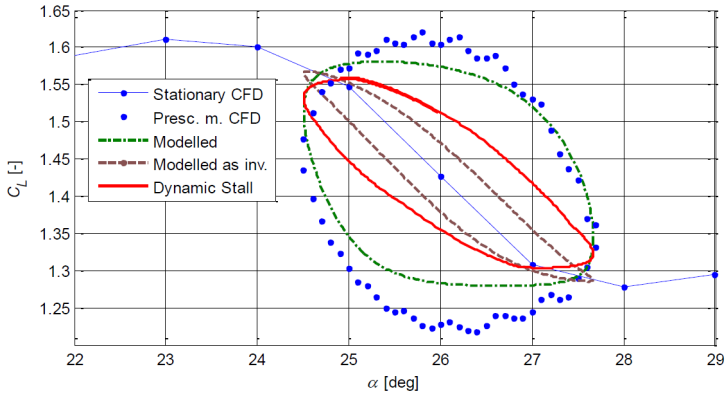

Figure 10.22. Lift coefficients from the: 2D CFD with the non-moving DU96-W-180, 2D prescribed motion CFD and from two engineering models.

the 3D CFD simulations are presented:

- Static lift coefficient resulting from the time-marching 3D CFD with the non-moving DU96-W-180
- Dynamic lift coefficient loop resulting from the prescribed motion 3D CFD
- Dynamic lift coefficient loop modeled assuming inviscid response using the method from [9, 11]; based on the 3D CFD polars
- Dynamic lift coefficient loop modeled using Beddoes-Leishman type [16, 17] dynamic stall model; based on the 3D CFD polars

The direction of the presented loops was clockwise. The results were surprising as the characteristic of the prescribed motion CFD dynamic-lift loop was completely different from the corresponding 2D CFD loop which was of negative slope. The loop averaged over 30 oscillation periods had positive slope, as if the static values were of positive instead of negative slope. Modelling the 3D CFD dynamic lift with the tools from [9, 11] or the Beddoes-Leishman model [16, 17] proved difficult and will require further investigation and possibly another approach. This is because these models are not developed to model loops with a slope of opposite sign to that of the steady values. To see results concerning drag coefficient loops of the 2D and 3D simulations, refer to [9, 18].

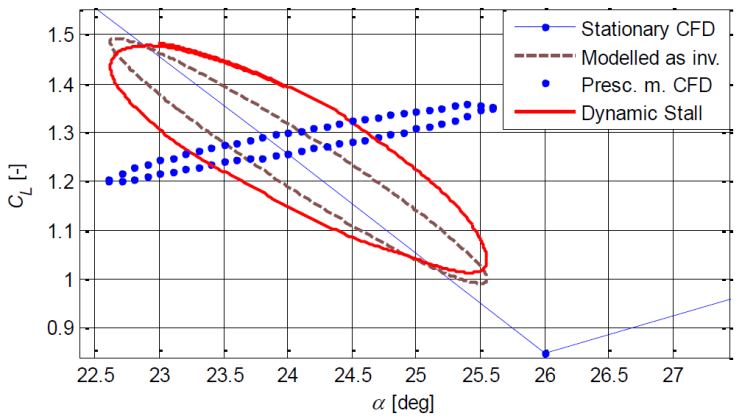

Figure 10.23. Lift coefficients from the 3D CFD with the non-moving DU96-W-180, 3D prescribed motion CFD and from two engineering models.

10.3 Conclusions

The current research on standstill wind turbine blade vibrations was divided into experimental and computational investigations. Standstill measurements carried out on LM 38.8m blade of the NM80 turbine were analyzed. Polars were extracted from the pressure-distribution time series measured at blade section 5 on August 19th, between 16:50 and 17:40. The angle of attack was determined in two alternative ways: by means of the yaw-misalignment measurement from the nacelle and the wind-direction measurement from the nearby met mast. The nacelle measurement showed to be more reliable. The wind speed was also measured at the nacelle and met mast. Dynamic pressure was measured at the stagnation point at section 5. The above mentioned were alternatively used for normalization of the loads in order to extract the polars. Wind-speed measurement from the nacelle appeared as the most reliable, qualitatively producing the most reliable polars. Unfortunately, the overall quality of the polars was unsatisfactory. Simple error analysis was performed in order to indicate whether the wind-speed or angle-of-attack measurements were the main source of error. The analysis included comparison of the CL, CD, CN, CT, CL/CD and CN/CT curves. While it was difficult to pinpoint a single faulty measurement (angle of attack, wind speed or pressure distribution), it seemed that an increase in quality of all the involved measurements, especially the pressure distribution, would be necessary to obtain reliable polars.

In the computational studies it was investigated whether the stand still vibrations are vortex-induced, stall-induced or a combination of both types. The work comprised analyzes based on engineering models and Computational Fluid Dynamics. Two-dimensional, three-degree-of-freedom, elastically-mounted-airfoil engineering models were created. Analysis based on these models showed that even a relatively low amount of time lag in the dynamic aerodynamic response significantly increases the models' aerodynamic damping. Note that state of the art aeroelastic codes assume quasisteady aerodynamics in deep stall. Therefore, these aeroelastic codes may inaccurately predict aerodynamic damping in deep stall, if the actual aerodynamic response of airfoils in deeps stall is slower than quasisteady. Further, two- and three-dimensional CFD computations on a DU96-W-180 airfoil were carried out around 25 and 90 degrees angle of attack. These included non-moving, prescribed-motion and elastically-mounted airfoil suspensions. These computations indicated the vortex-induced vibrations may occur on modern wind turbine blades at standstill conditions and moderate wind speeds. On the other hand, the occurrence of stall-induced vibrations appeared unlikely due to relatively high wind speed necessary for their onset. Analysis of dynamic lift and drag coefficient loops computed in stall with 3D CFD indicated that present engineering models may be insufficient in modeling these loops, and the problem should be investigated further in future work. Note that the present CFD computations involving 2D and 3D airfoils are not necessarily repre-

sentative of actual wind turbine blades due to lack of twist and taper. Computations on full blades should be carried out in future work together with investigations concerning different flow characteristics.

References

[1] C. Bak, H.Aa. Madsen, N. Troldborg, M. Gaunaa, W. Skrzypiński, A. Fischer, U. Paulsen, R. Møller, P. Hansen, M. Rasmussen, and P. Fuglsang. DANAERO MW: Instrumentation of the NM80 turbine and meteorology mast at Tjæreborg . Technical Report DTU Wind Energy Report-I-0083, Technical University of Denmark, 2013.

[2] C. Bak, H.Aa. Madsen, M. Gaunaa, U. Paulsen, P. Hansen, M. Rasmussen, P. Fuglsang, P. Enevoldsen, J. Laursen, and J. Romblad. DAN-AERO MW: Wind tunnel tests. Technical Report Risø-I-3047(EN), Technical University of Denmark, 2010.

[3] W.A. Timmer. Two-dimensional aerodynamic characteristics of wind turbine airfoils at high angles-of-attack. *3rd Conference on The science of making Torque from Wind, Crete, Greece,* 2010.

[4] J.A. Michelsen. Basis3D - a platform for development of multiblock PDE solvers. Technical report AFM 92-05, Technical University of Denmark, Lyngby, 1992.

[5] J.A. Michelsen. Block structured multigrid solution of 2D and 3D elliptic PDEs. Technical Report AFM 94-06, Technical University of Denmark, 1994.

[6] N.N. Sørensen. *General Purpose Flow Solver Applied to Flow over Hills*. PhD thesis, Technical University of Denmark, 1995.

[7] N.N. Sørensen. HyGrid a 2-D Mesh Generator. Technical report, Risø National Laboratory, 1998.

[8] J. Heinz, N.N. Sørensen, and F. Zahle. Investigation of the load reduction potential of two trailing edge flap controls using CFD. *Wind Energy*, 14, 2011.

[9] W. Skrzypiński. *Analysis and modeling of unsteady aerodynamics with application to wind turbine blade vibration at standstill condition*. PhD thesis, Technical University of Denmark, 2012.

[10] W. Skrzypiński and M. Gaunaa. Wind turbine blade vibration at standstill conditions âĂŞ the effect of imposing time lag onto aerodynamic response. *EWEC, Warsaw, Poland*, 2010.

[11] W. Skrzypiński and M. Gaunaa. Wind turbine blade vibration at standstill conditions - the effect of imposing lag on the aerodynamic response of an elastically mounted airfoil. *Submitted to Wind Energy*, 2013.

[12] R.T. Jones. The Unsteady Lift of a Wing of Finite Aspect Ratio. Technical Report NACA Repprt 681, 1940.

[13] W. Skrzypiński, M. Gaunaa, N.N. Sørensen, F. Zahle, and J. Heinz. Vortex-induced vibrations of a DU96-W-180 airfoil at 90 degrees angle of attack. *Submitted to Wind Energy*, 2013.

[14] M. Gaunaa and T.J. Larsen. Stilstandslaster. In C. Bak, editor, *Forskning i Aeroelasticitet EFP-2002*. Risø-R-1434(DA), Risø National Laboratory, 2004.

[15] W. Timmer. Wind tunnel test results for airfoils NACA 633-418 and Risø B1-18. Technical Report WE-082063, Delft University of Technology, Faculty of Aerospace Engineering, Wind Energy Research Group, 2008.

[16] J.G. Leishman and T.S. Beddoes. A semi empirical model for dynamic stall. *Journal of the American Helicopter Society*, 34:3–17, 1989.

[17] Hansen M.H., M Gaunaa, and H.Aa. Madsen. Beddoes-Leishman type dynamic stall model in state-space and indicial formulations. Technical Report Risø-R-1354(EN), Risø National Laboratory for Sustainable Energy, Technical University of Denmark, 2004.

[18] W. Skrzypiński, M. Gaunaa, N.N. Sørensen, and F. Zahle. Modeling of unsteady airfoil aerodynamics for the prediction of blade standstill vibrations. *EWEA, Copenhagen, Denmark*, 2012.

11 Investigations of Wind Turbine Wake Deficit and Loads in Partial Wake Operation

Author(s): N. Troldborg, H.A. Madsen, C. Bak

The inflow conditions and loads on the NM80 wind turbine operating partially in the wake of another wind turbine are analysed from field measurements as well as from numerical simulations using an actuator line technique combined with LES and predictions of an aero elastic engineering wake model.

11.1 Introduction

The inflow and load conditions on a turbine, which is operating in the wake of one or more turbines, deviate significantly from that of an isolated turbine. Typically a wake inflow causes increased fatigue loads, and in particular yaw loads, especially when the turbine is in partial wake operation. However, even when the wind direction is such that a turbine on average is operating fully in the wake of another turbine, large scale meandering of the wake causes the wake operating turbine to continuously experiencing part wake operation. For this reason wake meandering may significantly contribute to increased fatigue loads and this including this effect is of crucial importance when simulating turbines in wind farms. Even though a large body of work exists on wakes and wake operation, modelling partial wake situations as well as other cases with extreme shear over the rotor disc is a very challenging task, which even advanced state-of-the-art models has difficulties to handle as outlined by Madsen et al. [1] The objective of this paper is to present an analysis of the structure and dynamics of a wake based on Pitot tube measurements obtained along the blade of a modern wind turbine. Furthermore, to investigate how a turbine is loaded when it is partially exposed to wake flow. Finally, to investigate the ability of the actuator line method and an advanced aero-elastic engineering model to modelling the complex phenomenon of wake operation through a comparison with the measurements.

11.2 The DAN-AERO experiment

The used experimental data were obtained as a part of the DAN-AERO MW project [2, 3], in which one blade of a NM80 2MW wind turbine was heavily instrumented with various measuring equipment including e.g.:

- 4×64 surface pressure taps at four radial stations r=13 m, 19 m, 30 m and 37 m. In this way pressure distributions were obtained and integrating the pressure distributions resulted in normal forces and tangential forces normal to and parallel with the chord length, respectively.
- 4 five-hole Pitot tubes at the radial stations 14.5 m, 20.3 m, 31 m and 36 m. From these tubes the relative velocity, the inflow angle and slip angle can be determined.
- Strain gauges at 10 different radial stations. From these strain gauges the flap and edge moment can be determined. For the present analysis only the strain gauge located at the radial station 3 m was used. This sensor represents the flap root moment.

The instrumented turbine has a diameter of 80 m and is situated in a wind farm at the flat Tjæreborg Enge site. The wind farm is sketched in Figure 11.1 and consists of 8 turbines organized in two rows. The turbines in the southern row and WT3 are all of the NM80 type, while the others are Vestas V80's. The met mast denoted M1, which is located between WT2 and WT4, provides measurements of respectively wind speed, wind direction, pressure and

temperature at various heights above ground. As indicated in the figure, for a wind direction of 201^o the instrumented turbine WT3 operates fully in the wake of turbine WT4.

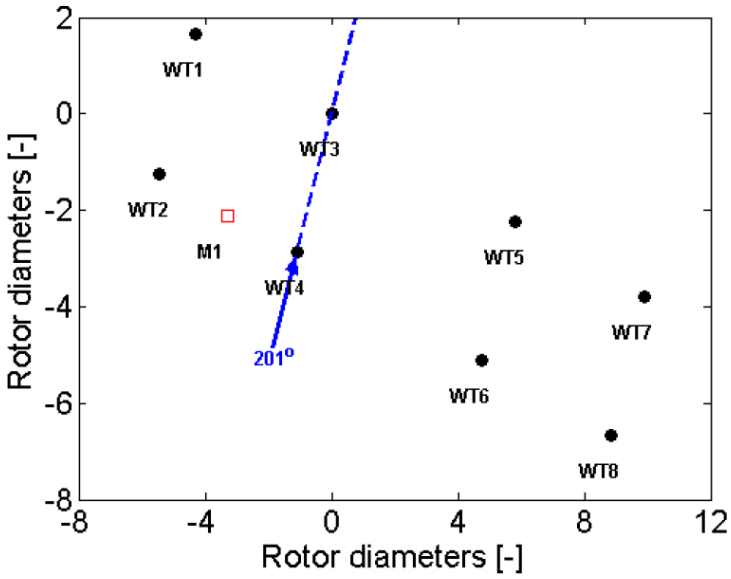

Figure 11.1. Layout of the Tjæreborg wind farm including meteorological mast (M1). The instrumented turbine is denoted WT3.

11.3 Computational methods

11.3.1 The actuator line simulations and atmospheric boundary layer modelling

The numerical simulations are carried out with the three-dimensional Navier-Stokes solver EllipSys3D [4–6] together with an actuator line [7] representation of the wind turbine blades. The atmospheric boundary layer is modeled using a technique where body forces, applied to the entire computational domain, are used to impose a given steady wind shear profile, while free-stream turbulence is modelled by introducing synthetic turbulent velocity fluctuations to the mean flow in a predefined cross-section upstream of the first rotor [8]. The numerical set-up is as described in [9].

11.3.2 Aeroelastic simulations

The aero elastic simulations are conducted using the HAWC2 model combined with the dynamic wake meandering (DWM) model [10] for representing the wake dynamics.

11.4 Results and discussion

The present analysis is based on two datasets measured on September 1^{st} 2009. The two datasets were chosen because they combine partial wake operation with well defined operational conditions, i.e. constant rotor speed, pitch and yaw position. The overall conditions during the two selected dataset are summarized in Table 11.1. The two cases represent approximately half wake and 2/3 wake operation.

Case	1	2
Date	01-09-2009 (12:30)	01-09-2009 (13:30)
Wind speed (57 m)	13.2 m/s	13.4 m/s
Turbulence intensity	7.5%	6.8%
Shear coefficient	0.26	0.19
Wind direction (17 m)	187^o	195^o
Wind direction (57 m)	187^o	195^o
Wind direction (90 m)	190^o	199^o
Yaw position	165^o	182^o
Yaw error	22^o	13^o
Rotor speed	16.2 RPM	16.2 RPM
Pitch	-4.75^o	-1.25^o

Table 11.1. Operational conditions in the two selected cases

11.4.1 Inflow conditions

In order to give an impression of the inflow experienced by the instrumented turbine Figures 11.2 and 11.3 show polar plots of respectively the measured and computed inflow angle at the radial station r = 31 m for each of the two cases. The corresponding results for the relative velocity are shown in Figures 11.4 and 11.5. The error bars included in the plots show the standard deviation of the predicted curves, while the green and red curves show the maximum and minimum predictions in the datasets, respectively. Note that azimuth angle equal to 0^o corresponds to the blade pointing upwards. Qualitatively, the agreement between actuator line

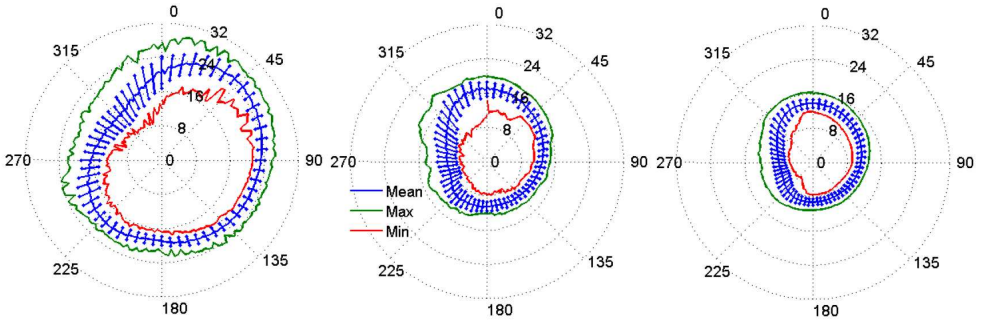

Figure 11.2. Azimuthal variation of the inflow angle at r=31 m in case 1. From left to right: Measurements, actuator line simulations and HAWC2 simulations.

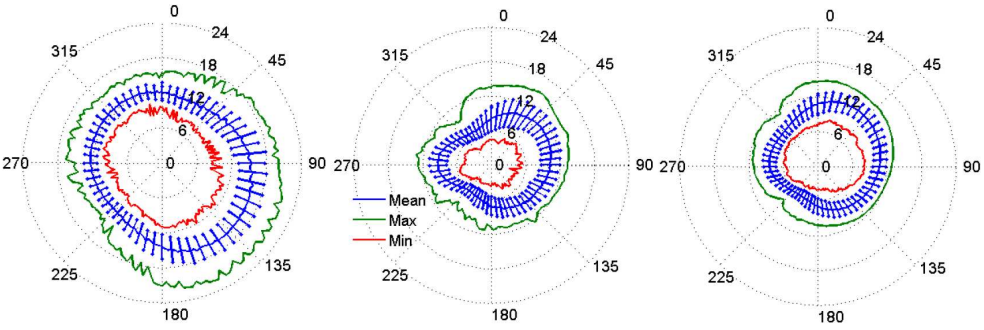

Figure 11.3. Azimuthal variation of the inflow angle at r=31 m in case 2. From left to right: Measurements, actuator line simulations and HAWC2 simulations.

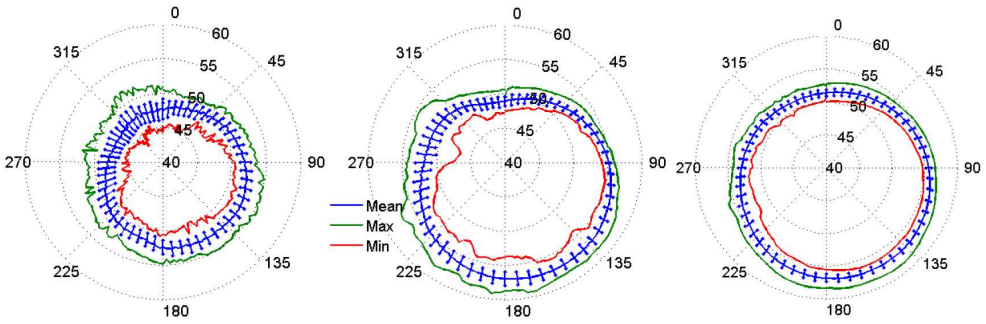

Figure 11.4. Azimuthal variation of the relative velocity at section 8 (r=31 m) in case 1. From left to right: Measurements, actuator line simulations and HAWC2 simulations.

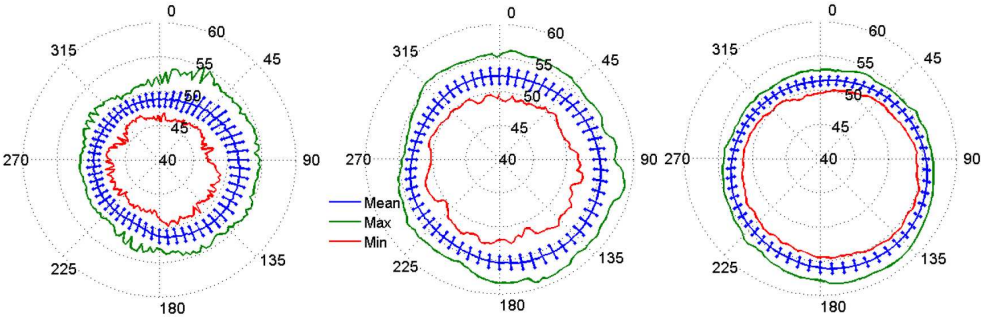

Figure 11.5. Azimuthal variation of the relative velocity at section 8 (r=31 m) in case 2. From left to right: Measurements, actuator line simulations and HAWC2 simulations.

and HAWC2 simulations is fairly good. However, when compared to measurements there are many differences. The most apparent is the inflow angle, which in the measurements, in both cases, is shifted compared to the simulations. It is difficult to explain the reason for this behavior in the measurements. One should rather expect a behavior as predicted by the two simulations where the inflow angle maximizes at azimuth angles between 45^o and 90^o where the blade is expected to be outside of the wake and at the same time is moving with the wind. Despite these differences both measurements and simulations predicts the same overall behaviour in the standard deviation: In case 1 the standard deviation of the inflow angle is clearly lowest for azimuth positions where the blade is outside the wake, where the opposite is true in case 2. The reason that the standard deviation in case 2 apparently is larger where at least parts of the blade on average should be outside of the wake is probably due to wake meandering. The overall behavior of the relative velocity predicted by both actuator line and HAWC2 simulations seem to agree fairly well with the measurements, though there are differences in the magnitude. However, since the measured values are at the position at the Pitot tube and the computed results are on the blade itself, one should not expect quantitative good agreement. The meandering effect mentioned above is clearly seen in Figure 11.6, which shows a representative time trace of the inflow angle at r = 31 m in case 1. The large peaks in the inflow angle occur whenever the blade rotates outside of the wake. The large variation in the magnitude of these peaks is evidently a sign of a meandering inflow wake. Furthermore, it is interesting to notice how abrupt the peaks in the inflow angle occur. This behaviour indicates that the incoming wake in a meandering frame of reference has very sharp edges.

11.4.2 Aerodynamic blade loading

Figure 11.7 shows the measured and simulated azimuth variation of the flap root moment in the two cases, respectively. Note that the shown flap root moments have been normalized with the

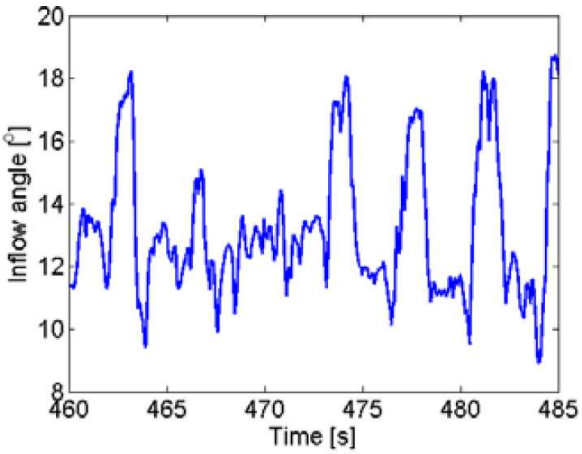

Figure 11.6. Time trace of inflow angle at r=31 m in case 1.

maximum value of the HAWC2 simulation. The numerical methods predict lower flap root moments than measured by the strain gauge. In case 1 the computed shape of the flap root moment deviates significantly from the measured curve. In the simulations the influence of the wake is clearly seen to reduce the flap root moment over approximately half of a rotor revolution, whereas it in the measurements only is reduced over approximately 1/4 of the rotor revolution. In case 2 there is a good agreement between actuator line simulations and HAWC2 simulations. In this case the overall shape of the flap root moment also compare rather well with the measurements. Figure 11.8 compares the measured and simulated loading tangential and normal to the chord. The loading has in all cases been normalized with the maximum normal load predicted by the HAWC2 simulation at r=30m. Note that there are only measurements available at the two inner sections because the pressure measurements on the two outer sections on this date were corrupted. In case 1 there are significant differences between measurements and simulations. Again the measured values indicate that this may not be a half wake case because the measured loads for azimuth angles between 0^o and 90^o are larger than in the simulations. In case 2 there is generally a much better agreement between measurements and simulations. However, again the simulations predict lower tangential loading at azimuth angles between 0^o and 90^o.

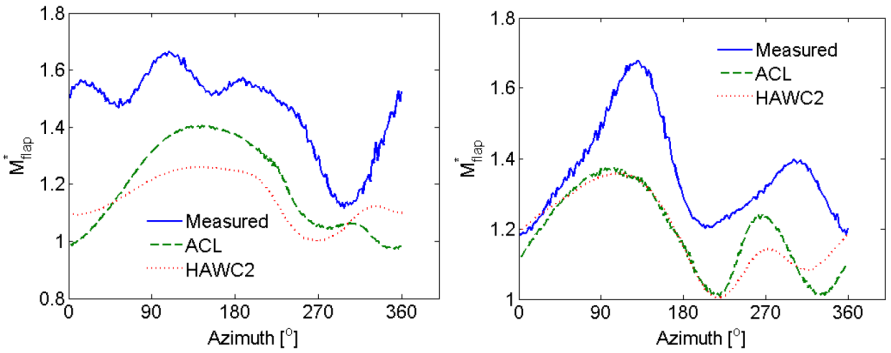

Figure 11.7. Scaled flap root moment as a function of azimuth position in case 1 (left) and 2 (right).

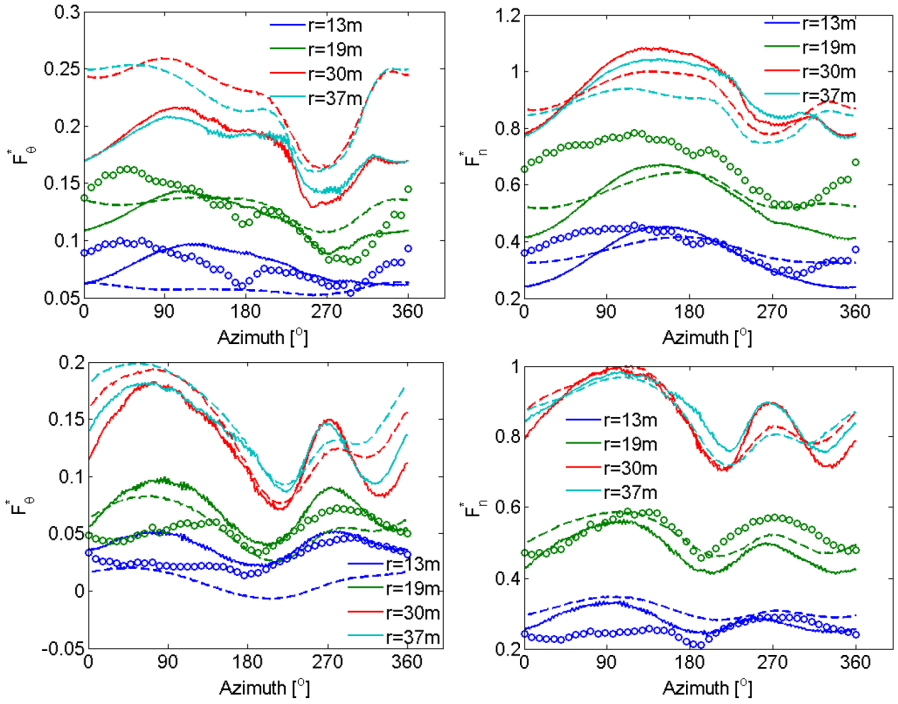

Figure 11.8. Scaled tangential and normal loading, respectively as a function of azimuth position in case 1 (top) and case 2 (bottom). Circles: Measurements; Full line: actuator line; Dashed line: Hawc2. Color code in legend.

11.4.3 Influence flexible blades

In the comparisons shown in the previous section only the aerodynamic loading was considered in the simulations. In order to study the influence of the structure dynamics including flexible blades and the mass of the blade the two cases were simulated again using HAWC2 with an aeroelastic model included. Figure 11.9 compares the aerodynamic flap root moment predicted with flexible and stiff blades. Also included in the plot is the structural moment. As seen accounting for the structure dynamics significantly improves the comparison with the measurements both in terms of shape and magnitude.

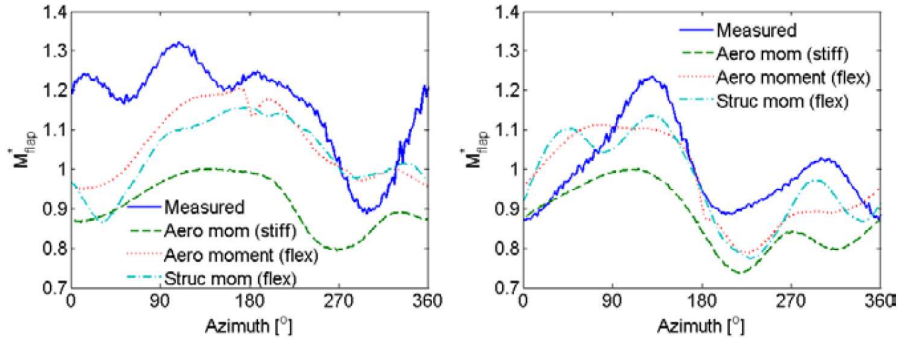

Figure 11.9. Scaled flap root moment as a function of azimuth position in case 1 (left) and 2 (right).

11.5 Conclusions

The inflow and loads on a wind turbine operating partially in the wake of another turbine has been analyzed from measurements and two different computational methods. A comparison of measured and computed values revealed fair qualitative agreement but also significant differences. Further investigations have to be made to determine what is causing the observed differences. The analysis showed that the inflow angle can be used to separate the blade azimuth positions where the blade is inside the wake from those where it is outside and hence enables derivation of statistics of e.g. angle of attack variations both inside and outside the wake. Furthermore, it was shown that despite the ambient flow being turbulent the wake as seen in a meandering frame of reference is well defined with a sharp edge at the wake boundary. Finally, it was shown that including the structure dynamics of the blade in the aeroelastic simulations significantly improved the agreement with measured flap root moments.

References

[1] H.Aa. Madsen, V. Riziotis, F. , Zahle, M.O.L. Hansen, H. Snel, F. Grasso, T.J. Larsen, E. Politis, and F. Rasmussen. Blade element momentum modeling of inflow with shear in comparison with advanced model results. *Wind Energy*, 15:63–81, 2012.

[2] C. Bak, H.A. Madsen, U.S. Paulsen, M. Gaunaa, N.N. Sø rensen, P. Fuglsang, J. Romblad, N.A. Olesen, P. Enevoldsen, J. Laursen, and L. Jensen. DAN AERO MW: Detailed aerodynamic measurements on a full scale MW wind turbine. *EWEC, Warsaw, Poland*, 2010.

[3] H.A. Madsen, C. Bak, U.S. Paulsen, M. Gaunaa, N.N. Sørensen, P. Fuglsang, J. Romblad, N.A. Olesen, P. Enevoldsen, J. Laursen, and L. Jensen. The DANAERO MW Experiments. *AIAA 2010-645, 48th AIAA Aerospace Sciences Meeting and Exhibit, Orlando, Florida*, 2010.

[4] J.A. Michelsen. Basis3D - a platform for development of multiblock PDE solvers. Technical report AFM 92-05, Technical University of Denmark, Lyngby, 1992.

[5] J.A. Michelsen. Block structured multigrid solution of 2D and 3D elliptic PDEs. Technical Report AFM 94-06, Technical University of Denmark, 1994.

[6] N.N. Sørensen. *General Purpose Flow Solver Applied to Flow over Hills*. PhD thesis, Technical University of Denmark, 1995.

[7] Sørensen J.N. and Shen W.Z. Numerical modelling of wind turbine wakes. *Fluids Engineering*, 124, 2002.

[8] N. Troldborg, J.N. Sørensen, R. Mikkelsen, and N.N Sørensen. A simple atmospheric boundary layer model applied to large eddy simulations of wind turbine wakes. *Accepted for publications in Wind Energy*, 2013.

[9] N. Troldborg, G.C. Larsen, H. Aa. Madsen, K.S. Hansen, J.N. Sørensen, and R. Mikkelsen. Numerical simulations of wake interaction between two wind turbines at various inflow conditions. *Wind Energy*, 14:859–876, 2011.

[10] G.C. Larsen, H.Aa. Madsen, K. Thomsen, and T.J. Larsen. Wake meandering: a pragmatic approach. *Wind Energy*, 11:377–395, 2008.

12 Aerodynamic Noise Characterization of NM80 Turbine through High-Frequency Surface Pressure Measurements

Author(s): F. Bertagnolio, H.A. Madsen, C. Bak, N. Troldborg, A. Fischer

The aim of this section is to investigate and characterize the aerodynamic noise emission from the blade of the NM80 turbine and in particular to study the influence of atmospheric turbulence and the turbulence from operation in wake of another turbine on noise emission.

12.1 Introduction

The aerodynamic noise produced by modern megawatt-sized wind turbines originates mainly from two types of flow-structure interactions: turbulent inflow noise which is usually dominating in the low-frequency range, and trailing edge-turbulent boundary layer noise in the high-frequency range (see Wagner [1] for a review on wind turbine noise).
Turbulent inflow (TI) noise is produced by atmospheric turbulence vortices that upon impingement on a wind turbine blade generate opposite surface pressure (SP) fluctuations on each side of the blade, subsequently radiating as sound. Such incoming atmospheric turbulence may have two origins: the natural wind turbulence created within the atmospheric boundary layer (BL) and/or the wake flow structures generated by one or more wind turbines, or alternatively by other large objects such as buildings or trees, located upstream of the wind turbine of interest.
Trailing edge (TE) noise is produced by the convection past the sharp TE of an airfoil of the vortices generated within the turbulent BL developing on the airfoil surface itself, resulting in a scattering phenomenon. Theoretical work shows that the radiated noise in the far-field can be directly related to the SP turbulent fluctuations near the TE [2, 3].
Since both TI and TE noise are related to the SP fluctuations, the SP spectra may be used to characterize noise emission in the far-field for both mechanisms, TI noise being predominantly generated in the area of the airfoil section near the leading edge (LE) [4, 5] whereas TE noise is characterized by airfoil SP fluctuations occurring near the TE [3]. It should be emphasized that the SP fluctuations generated by either the atmospheric TI or the airfoil turbulent BL vortices are less prone to be contaminated by spurious experimental noise since the intensity of these fluctuations is typically larger than the sound that they will subsequently radiate or than any other ambient noise for that matter. Therefore, measuring these SP fluctuations contributes to an accurate characterization of the actual aeroacoustic noise generated by a wind turbine.
This chapter uses field measurements, wind tunnel tests and two different modelling approaches to characterize the SP fluctuations and hence also noise emissions from the blade of the NM80 turbine. The aim is to investigate the influence of atmospheric and wake turbulence on noise emission as well as to validate the used noise models. To fit best the overall structure of the report the model validation results are placed in chapter 13 whereas the models are presented in the present chapter.

12.2 Description of the Measurements

The main characteristics of the experimental campaign are described in this section. More details concerning the experimental set-up, measurement conditions and acquired data can be found in the references [6, 7].

12.2.1 Full-Scale Wind Turbine Set-Up

A new test blade, a LM 38.8 m blade, was manufactured and during the manufacturing of the blade, a lot of sensors were integrated in the blade structure. Afterwards the blade was mounted on a NM80 2.3 MW turbine which is located in a flat terrain area and is part of a small wind farm of 8 turbines located in Tjæreborg, Denmark.
In the present work the following sensors are used:

- Pressure taps measuring static pressure distributions along the blade chord at 100 Hz at four radial positions (r=13 m, 19 m, 30 m and 37 m)
- Five-hole Pitot tubes measuring relative inflow velocity and local angle of attack (AoA) at a sampling frequency of 35 Hz at four radial positions (r=14.5 m, 20.3 m, 31 m and 36 m)
- 50 high frequency microphones for measuring SP fluctuations at 50 kHz was installed at r=37 m.
- Sensors measuring the rotational speed, pitch and azimuthal position of the blade.
- Cup and sonic anemometers as well as wind vanes for measuring wind velocity and direction at several heights at a nearby meteorology mast.
- Sensors for measuring temperature and pressure at the met mast (used for deriving air density).

12.2.2 Analysis tool

In order to analyze the pressure coefficient distributions and fluctuating SP measurements, an analysis software tool was developed. The analysis takes the following steps:

- Identify particular periods of time during the campaign that are of interest for a specific study.
- Truncate the recorded pressure distributions and SP time-series into shorter time-series so that the latter represent the state of the flow for a relative short azimuth displacement of the blade (in our case, the shorter time period is $1/4$ s or an azimuth span of 24^o).
- For each of these shorter time-series, the various aerodynamic (e.g. local AoA, relative inflow velocity, wind speed, electrical power) and geometric (e.g. azimuth position of the blade, yaw angle, wind direction) parameters are averaged during the corresponding time period of recording.
- Sort the shorter time-series by enforcing various user-defined constraints on these aerodynamic or geometric averaged values.
- Bin average the time series according to the values of one of the above aerodynamic or geometric averaged parameters, often the local AoA.
- Perform a spectral analysis on the binned SP time-series, including spectral averaging of the selected data within the same bin, whilst the binned pressure distributions are simply averaged.

12.2.3 Wind Tunnel Measurements of the NACA 63-418 Airfoil

In addition to the field experiment presented above, measurements of a NACA 63-418 airfoil section were conducted in the LM Wind Power wind tunnel in Lunderskov [7]. The airfoil model has a shape that is identical to the 37 m radius cross-section of the LM 38.8 blade of the NM80 turbine, though with a shorter 0.9 m chord compared to the 1.2 m chord on the blade at this radius.

The airfoil model was equipped with pressure taps and microphones in the same way as for the equipped wind turbine blade section. In addition to measurements carried out in a clean tunnel with a turbulence intensity around 0.1%, other measurements were carried out with a turbulence grid in the inlet to the test section raising the turbulence intensity to about 1.2%. Finally, SP measurements were conducted with two different trip/roughness tapes mounted close to the LE of the airfoil.

12.2.4 Pitot Tubes and Calibration of Inflow Angles

From the five-hole Pitot tube measurements two inflow angles can be derived as well as the relative velocity. The Pitot tubes were positioned relatively to the blade so that one of the measured angles is the local AoA of the inflow to the blade. However, for analyzing noise model results as well as for comparisons with the wind tunnel measurements on the copy of the blade section, it is necessary to convert this local inflow angle to a standard AoA which is the angle between the chordline and the free wind vector for an airfoil section in a two-dimensional (2D) flow. The transfer functions to convert from angles of attack measured by the Pitot tubes to angles of attack measured in the wind tunnel is established from analysis of the pressure distributions on the turbine blade and in the wind tunnel, respectively as described by Bak [8] and verified by Bertagnolio et al. [9].

Unfortunately, the Pitot at the most outboard section ($r = 36\,\mathrm{m}$) was malfunctioning and there the AoA measured with the Pitot tube located at the next inward station at radius $r = 31\,m$ had to be used for analyzing the pressure measurement data at $r = 37\,\mathrm{m}$. However, through analysis of measurements and use of the Blade Element Momentum (BEM) theory by Glauert [10] Bertagnolio et al. [9] showed that the difference between the AoA at $r = 31\,\mathrm{m}$ and $r = 37\,\mathrm{m}$ is small. A conclusion which was also confirmed using 3D CFD calculations.

12.3 Numerical Models

In this section the various modelling techniques used here are described. The so-called TNO-Blake TE noise model is used to calculate SP fluctuations generated by the airfoil turbulent BL in the vicinity of the TE. In addition, Amiet's TI noise model is used to calculate SP fluctuations near the airfoil LE as a response to the inflow turbulence. The TNO-Blake model requires as input additional informations concerning the BL characteristics. For this purpose, 2D CFD calculations of the airfoil section are performed at specified AoA and Reynolds number.

12.3.1 CFD Reynolds-Averaged Navier-Stokes simulations

The in-house developed Navier-Stokes incompressible finite volume flow solver EllipSys2D [11–13] is used for the steady state RANS simulations on the NACA 63-418 airfoil. The $k-\omega$ SST turbulence model by Menter [14] in its original version is used to obtain the turbulent viscosity. The O-type mesh used for the calculations is refined near the airfoil surface so that the non-dimensionalized distance of the first mesh point from the airfoil surface always satisfies the condition $y^+ \leq 1$ as required for this type of computations. The grid extends 35 chords away from the airfoil. It contains 256 cells around the airfoil and 256 from the airfoil to the outer boundary. In the calculations, the transition is determined with the e^n transition model by Drela and Giles [15]. In some cases, the transition will be fixed at some specified chord location in order to model a tripping device or a known transition location.

12.3.2 Modified TNO-Blake Trailing Edge Noise Model

The turbulent BL developing over the airfoil surface is idealized as the flow over an infinite half-plane for which the main flow direction is denoted as x_1, the direction normal to the wall is x_2, and x_3 is the direction transversal to the flow and parallel to the TE. (x_1, x_2, x_3) are indifferently denoted as (x, y, z) in the following. Assuming homogeneity in time and in planes parallel to the surface, neglecting turbulence second-order moments and using Green's function formalism, a solution for the wave number-frequency SP spectrum can be obtained as an integral across the BL [16–18]. An improved version of the model [19] takes the following form:

$$\Phi_p(k_\parallel, \omega) = 4\rho_0^2 \frac{k_1^2}{k_1^2 + k_3^2} \int_0^{\delta_{BL}} 2L_2(y) \left(\frac{\partial U_1}{\partial y}(y) \right)^2 \overline{u_2^2}(y) \widetilde{\Phi}_{22}(k_\parallel, \Lambda) \times \Phi_m(\omega - U_c(y)k_1)\, e^{-2k_\parallel y}\, dy \quad (7)$$

where δ_{BL} is the BL thickness, L_2 is the vertical correlation length characterizing the vertical extent of the vertical turbulent velocity component u_2, $\overline{u_2^2}$ its mean squared value, U_1 is the streamwise mean velocity, $k_\parallel$ is the norm of the wavenumber vector $k_\parallel = (k_1, k_3)$ spanning the plane parallel to the wall, $\widetilde{\Phi}_{22}$ is the normalized spectrum of the vertical velocity fluctuations integrated over k_2, Φ_m is the so-called moving axis spectrum which describes how $\widetilde{\Phi}_{22}$ is distorted by the generation and destruction of eddies during their convection past the TE. Details of its definition can be found in the paper by Moriarty [20], but it is here approximated as a Dirac delta function assuming frozen turbulence. The convection velocity U_c of these eddies is related to the local velocity as: $U_c(y) = 0.7U_1(y)$. Note that $\widetilde{\Phi}_{22}$ depends on the integral length scale Λ (see definition below) and is therefore also a function of y.

The various quantities in the integral in Eq. (7) need to be quantified in order to evaluate the SP spectrum. In this work, the RANS-CFD solver EllipSys2D (see description above) is used. It directly provide the BL thickness and the mean velocity profile. The turbulent normal stress can be estimated from the turbulent kinetic energy (TKE) k_T calculated by the solver as: $\overline{u_2^2} = \alpha_k k_T$ where α_k is set to 0.45 and 0.3 on the suction and on the pressure side of the airfoil, respectively.

Using the classical Von Karman model and introducing anisotropy stretching factors [21], the vertical velocity spectral tensor $\widetilde{\Phi}_{22}$ reads:

$$\widetilde{\Phi}_{22}(k_\parallel, \Lambda) = \frac{4}{9\pi} \Lambda^2 \beta_1 \beta_3 \frac{(\beta_1 \Lambda k_1)^2 + (\beta_3 \Lambda k_3)^2}{[1 + (\beta_1 \Lambda k_1)^2 + (\beta_3 \Lambda k_3)^2]^{7/3}} \quad (8)$$

where the integral length scale Λ characterizes the size of the energy-containing eddies, the coefficients β_1 and β_3 are anisotropic stretching factors in the streamwise and spanwise directions, respectively. Following the approach by Lynch *et al* [22] and introducing the stretching factors in the derivation, the correlation length L_2 is defined as a frequency dependent quantity:

$$L_2(\omega) = \frac{55\Gamma(1/3)}{108\sqrt{\pi}\Gamma(17/6)} \Lambda \beta_2 \frac{3 + 11(\beta_1 \Lambda k_c)^2}{3 + 8(\beta_1 \Lambda k_c)^2} \frac{1}{\sqrt{1 + (\beta_1 \Lambda k_c)^2}}$$

where $k_c = \omega / U_c$ is the convective wavenumber and β_2 is an additional anisotropy stretching factor in the direction perpendicular to the airfoil surface. Using the turbulence dissipation rate ε calculated by the RANS solver, the integral length scale can be deduced [23] from the asymptotic behavior of the Von Karman spectrum in the inertial range as:

$$\Lambda = 0.314 k_T^{3/2} / \varepsilon \quad (9)$$

In order to close the model and as a result of a tuning procedure using experimental data (see [19] for details), the anisotropy stretching factors are given as:

$$\beta_1 = 0.4 \quad \text{and} \quad \beta_2 = (\gamma)^{1/5} \quad \text{and} \quad \beta_3 = (2\gamma)^{1/2}$$

using the following non-dimensional BL pressure gradient along the airfoil chord defined as:

$$\gamma = \frac{\delta_{BL}}{U_\tau} \left[\frac{(\partial P / \partial x_1)^2}{\rho_0 \mu} \right]^{1/3}$$

where P is the mean static pressure, U_τ is the friction velocity, and μ the dynamic viscosity.

The frequency-spectrum of the SP fluctuations that will be considered later in this paper for comparisons with measurements is obtained by integrating Eq. (7) over the whole wavenumber space:

$$\Phi_p(\omega) = \iint_{-\infty}^{+\infty} \Phi_p(\omega, k_\parallel)\, \mathrm{d}k_1 \mathrm{d}k_3 \tag{10}$$

The far-field noise spectrum $S(\omega)$ can be deduced from the SP spectrum model defined above using Howe's theory [3]. For an observer located at a distance R above the TE orthogonally to the flow leaving the TE and in the limit of low Mach number flow, it reduces to [24]:

$$S(\omega) = \frac{L}{4\pi R^2} \int_{-\infty}^{+\infty} \frac{\omega}{c_0 |k_1|}\, \Phi_p(\omega, k_\parallel)|_{k_3=0}\, \mathrm{d}k_1 \tag{11}$$

where L is the span of the considered airfoil section. Comparing Eqs. (11) and (10), it is clear that SP and far-field noise frequency spectra are closely related and that the former can be used to characterize the latter.

12.3.3 Amiet's Turbulence Inflow Noise Model

In the theoretical derivation of inflow noise by Amiet [4], the incoming turbulence is assumed to be frozen and the airfoil is idealized as a flat plate. SP fluctuations and far-field noise are generated by inflow gusts modeled by sinusoidal variations of the velocity component normal to the airfoil plane.

The airfoil SP can be found by summing up the airfoil response for all gust frequency contributions. Assuming an airfoil of chord $2b$ and span $2d$ in a turbulent flow with mean velocity U, the power spectral density (PSD) of the SP fluctuations reads:

$$\Phi_p(x, \omega) = 2U(\pi \rho_0)^2 \int_0^\infty g^*\left(\xi, K_1, k_3\right) \cdot g\left(\xi, K_1, k_3\right) \Phi_{22}(K_1, k_3)\, \mathrm{d}k_3 \tag{12}$$

where $K_1 = \omega/U$ is the convective wave-number, $\xi = x/b$, x being the abscisse along the chord relatively to the chord center. g is the airfoil response function to a vertical gust (see its detailed derivation in [5]), and Φ_{22} is the spectrum of the turbulence inflow component normal to the airfoil integrated along the normal wave-number k_2, the classical Von Karman isotropic spectrum is being assumed here. Note that the former result has been divided by a factor 4 compared to the original formula by Amiet as the latter is given for the pressure jump between the suction and pressure sides of the airfoil.

The radiated far-field noise spectrum generated by the above SP fluctuations is given as:

$$S(r, \omega) = \left(\frac{\omega \rho_0\, by}{c_0\, \sigma^2}\right)^2 \pi U d \left|L(r, K_1, K_3)\right|^2 \Phi_{22}(K_1, K_3) \tag{13}$$

where $r = \{x, y, z\}^T$ is the observer location relativelÃęy to the airfoil center, $K_3 = \omega z/c_0\, \sigma$, $\sigma^2 = x^2 + \beta^2(y^2 + z^2)$ and $\beta^2 = 1 - M^2$. The Mach number is defined as: $M = U/c_0$, where c_0 is the sound velocity. The effective lift response is calculated from the response function g as:

$$L(r, K_1, k_3) = \int_{-1}^{1} g(\xi, K_1, k_3)\, \mathrm{e}^{-i\mu\xi(M - x/\sigma)}\, \mathrm{d}\xi$$

where $\mu = MK_1 b/\beta^2$. Similarly to the TNO-Blake model in the previous section, comparing Eqs. (13) and (12) shows that SP and far-field noise frequency spectra are closely related.

Note that Amiet's TI noise theory was extended to rotor noise evaluation [25]. It was implemented and tested during the present study. However, since rotational speeds are moderate and relative Mach numbers remain sufficiently low, no significant difference was observed between results of the two model formulations. In addition, for sufficiently large TI vortices (i.e. low wave numbers) blade-to-blade correlation effects arise and concentrate sound energy around

blade passage harmonics. This phenomenon is not included in the present study. In any case, it only affects lower frequencies in the spectra that will not be considered here.

Amiet's model requires as input parameters the relative inflow velocity, the turbulence intensity to determine the normal velocity component variance $\overline{u_2^2}$ and the integral length scale for evaluating the turbulence spectrum Φ_{22}. In the case of the NM80 rotor, the relative inflow velocity can be evaluated using the BEM model or the 3D CFD calculations mentioned in Section 12.2.4 or measurement data. The remaining quantities can be evaluated using empirical formulae for atmospheric turbulence or from mast measurement data. As for the wind tunnel experiment, all these quantities are measured using hot-wire anemometry [26].

12.4 Results

This section presents the results of the analysis of the data.

12.4.1 Analysis of Pressure Coefficient Distributions

In this section, the pressure coefficient distributions measured in the LM wind tunnel and on the turbine blade are compared to the CFD calculation results. The comparisons are performed at equivalent Reynolds numbers and AoA and therefore validates the calibration technique proposed in Section 12.2.4 to convert measured local inflow angles from the Pitot tubes to actual 2D AoA.

Fig. 12.1(a) compares CFD results and LM wind tunnel measurements of the pressure coefficient distributions for two AoAs $\alpha = 8$ and 10^o . Fig. 12.1(b) shows the corresponding comparison for the LM wind tunnel and NM80 experiment measurements where a bin size of $\pm 0.5^o$ are used in the measurements on the NM80 turbine. In all cases, there is generally a good

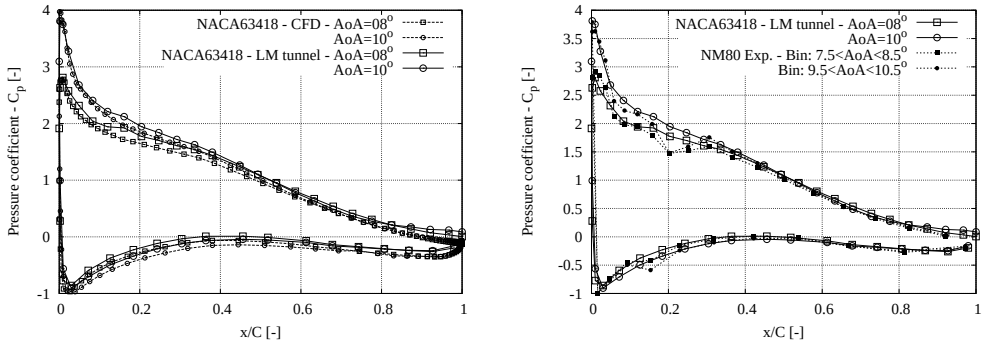

Figure 12.1. Pressure Coefficient along the NACA 63-418 Arfoil: a) CFD vs. LM wind tunnel measurements; b) LM wind tunnel vs. NM80 wind turbine at $r = 37$ m.

agreement between the computational results and measurements. The good agreement brings confidence in the methodology for extrapolating the measured AoA and relative velocity at radius $r = 31$ m to $r = 37$ m using the technique introduced in Section 12.2.4.

12.4.2 Analysis of transition point positions

In order to illustrate the differences between the actual flow on the LM 38.8 blade, the wind tunnel conditions in the LM Wind Power facility and the ideal conditions of the CFD calculation, the transition locations along the airfoil section chord on the suction side for the various cases described in section 13.1.2 are displayed as a function of the AoA in Fig. 12.2.

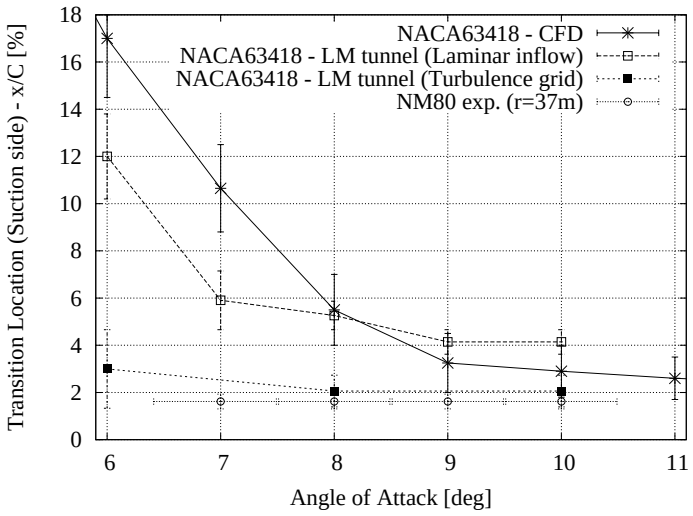

Figure 12.2. Transition Location on the Suction Side of NACA63418 Airfoil Section.

As for the measurements, the high-frequency microphones are used to detect transition as described by Døssing [27]. Uncertainties displayed as error bars in the figure are associated to the distances between two consecutive microphones along the airfoil chord that intrinsically limit the accuracy of the detection of transition location. In addition, horizontal error bars characterize the AoA uncertainties for the NM80 data associated to the binning process (see above). As for the CFD calculations, the error bars are associated to the actual transition location predicted by the e^n transition model [15] (lower limit of the error bar) and the intermittency model that is used in the code to ensure a smooth transition from a laminar BL to a fully turbulent BL (higher limit of the error bar). The results obtained for the wind tunnel experiment for which a turbulence grid was installed at the inlet of the test section are also reported.

It can clearly be observed that the transition location behavior is quantitatively similar for the CFD calculation and the wind tunnel experiment in the absence of turbulence grid (denoted hereafter as 'laminar' flow even if the wind tunnel inflow contains residual turbulence in the order of 0.1% as specified in Section 12.2.3). Contrastingly, the wind tunnel data in the presence of a turbulence grid and the experimental data acquired on the NM80 turbine exhibit a transition consistently located upstream of the previous results. In addition, in the latter cases, transition location is relatively unaffected by changes in AoA.

12.4.3 Relations between Inflow Turbulence, Transition and Boundary Layer Turbulence

In order to explain the discrepancies observed between the measured SP spectra at the TE and the CFD/TNO-Blake calculations at equivalent AoA, (see section 13.1.2) the influence of inflow turbulence and of tripping the airfoil is investigated. During the experimental campaign conducted in the LM Wind Power wind tunnel as described in Section 12.2.3, in addition to the case of a clean airfoil and laminar inflow conditions, various additional configurations were studied. In particular, the airfoil BL was tripped near the LE using a zig-zag (ZZ) tape and a turbulence grid was placed in the inlet of the wind tunnel test section increasing the inflow turbulence to approximately 1.2% [26, 28]. The two methods were both tested individually and in combination.

Firstly, the influence of the tripping and of the turbulence grid on the SP fluctuations near the airfoil LE is investigated at $x/C = 7.15\%$ on the suction side of the airfoil, which is located downstream of the transition point even for a clean airfoil in laminar inflow. The SP spectra are

plotted in Figs. 12.3(a) and (b) for AoAs equal to $\alpha = 8$ and 10^o, respectively.

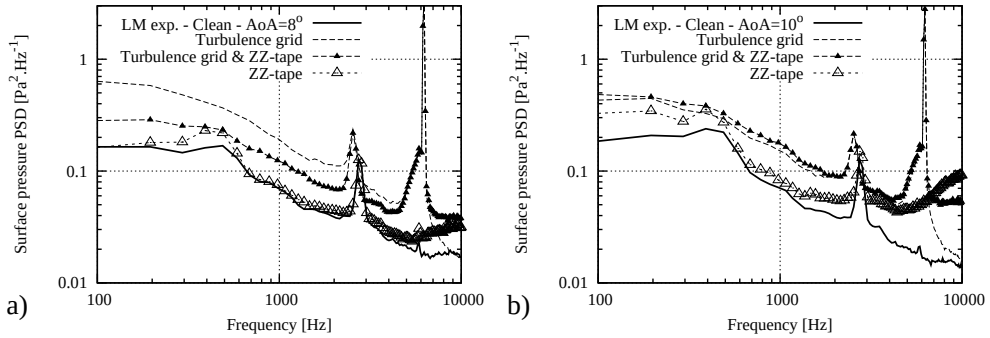

Figure 12.3. SP Spectra near LE ($x/C = 7.15\%$, Suction Side) - NACA63418 in LM Wind Tunnel: a) $\alpha = 8^o$; b) $\alpha = 10^o$.

Whereas the turbulence grid significantly increases the SP fluctuations energy in the whole frequency range compared to the clean airfoil in laminar inflow, the ZZ tape mainly influences the higher frequency range of the spectra and slightly the low frequencies. When combining both devices, at the lowest AoA the ZZ tape unexpectedly reduces the influence of the turbulence grid, whilst at the highest one it only has a small effect. Note the presence of the spurious peak in the spectra around 3000 Hz generated by the wind tunnel fan as observed in section 13.1.1, as well as the broader and intense peak around 6000 Hz associated to spurious noise generated by the turbulence grid.

Secondly, the influence of the tripping and of the turbulence grid on the SP near the TE is studied. The SP spectra measured in the wind tunnel are plotted in Figs. 12.4(a) and (b) for AoAs equal to $\alpha = 8$ and 10^o, respectively. The influences are different than what was observed

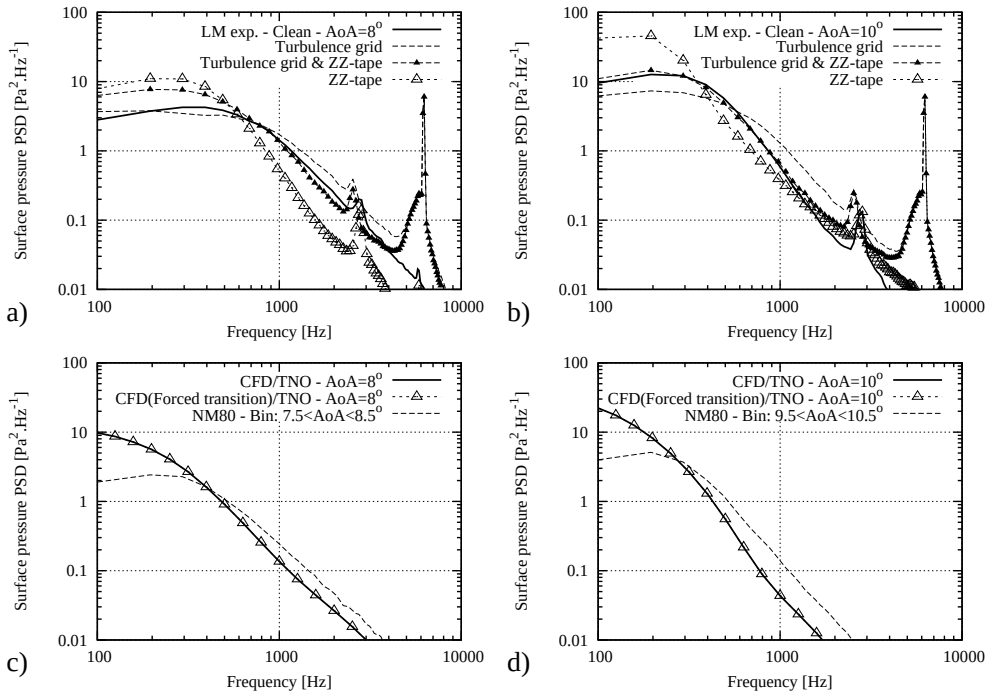

Figure 12.4. SP Spectra near TE (Suction Side): a) LM experiment at $\alpha = 8^o$ ($x/C = 92.2\%$); b) Same as (a) but $\alpha = 10^o$; c) NM80 Turbine vs. CFD/TNO at $\alpha = 8^o$ ($x/C = 93.3\%$); b) Same as (c) but $\alpha = 10^o$.

at the LE. The turbulence grid increases the SP spectral energy in the higher frequency range and decreases it in the lower range. Surprisingly, the ZZ tape has the opposite effect, though it slightly increases the SP spectral energy in the high frequency range for the highest AoA. Combining the two methods produces intermediate results. In addition, the results presented in the previous section comparing the NM80 mesurements with CFD/TNO-Blake model calculations are reported once again for two AoAs $\alpha = 8$ and 10^o in Figs. 12.4(c-d). In addition, CFD calculations were also performed by forcing transition at approximately the same location where transition does occur on the blade. It can be seen that forcing transition in this way more upstream and closer to the LE has no effect on the modeled SP spectra at the TE. The important conclusion that can be drawn by comparing Figs. 12.4(a-b) with Figs. 12.4(c-d) is that inflow turbulence has the same effect on the SP near the TE in both the wind tunnel and on the NM80 wind turbine compared to their respective reference cases, i.e. the wind tunnel without turbulence grid (laminar or quasi-laminar inflow) for the wind tunnel and CFD calculations for the NM80 turbine. This explains the discrepancies shown in Fig. 13.2(b) (section 13) where the SP spectra measured on the NM80 turbine departed from the CFD/TNO-Blake model results performed at corresponding AoA.

12.4.4 Influence of Inflow Turbulence and Wake Effects

The influence of the inflow turbulence is studied in a first step by comparing the SP measurements performed in the wind tunnel and on the LM 38.8 blade. The microphones considered in both cases are located near the LE at $x/C = 2.2\%$ on the pressure side of the airfoil/blade, which is located upstream of the transition location in all cases. These measurements are then representative of the inflow turbulence impinging on the airfoil section. These data are compared with results obtained with Amiet's model (see Section 12.3.3). In the case of the NM80 experiment, the measured spectra were acquired when the turbine operated in a free-wake situation and data were sorted out by binning the recorded time-series so that the blade is pointing vertically downward within an azimuth angular interval of 90^o. The inflow velocity at blade radius $r = 37$ m where the SP is measured can be determined from the Pitot tube. The height of the measured blade section averaged during the measurement period is estimated at 28.5 m, the tower height being 60 m. The turbulence intensity is deduced from a velocity sensor located on a nearby wind mast at the same height and is estimated to 10%. The turbulence integral length scale is estimated by the following empirical formula for atmospheric flow as $\Lambda = 0.7\times$ height, i.e. approximately 20 m. These quantities are used as input for Amiet's model. As for the wind tunnel measurements, these quantities could be acquired using hot-wire anemometry. The wind tunnel results presented hereafter include only the case for which the turbulence grid was present in the wind tunnel section upstream of the measured airfoil. The measured turbulence intensity is 1.2% and the integral lengh scale $\Lambda = 15$ mm. Note that the measured spectra displayed in the following are truncated above 2000 Hz. Indeed, as observed in Fig. 12.3, beyond this frequency wind tunnel fan noise and turbulence grid generated noise result in large broadband peaks that pollute this part of the spectra.

Due to the large difference in turbulence scales present in the wind tunnel (of the order of a centimeter) and in the atmosphere (of the order of 20 m as mentioned above), a scaling of the results is necessary. Amiet's model data collapse in the limit of high-frequencies for microphones located at the same relative chord location by using the following scaling for the SP spectra: $S_p(\omega) \approx U\overline{u_2^2}\Lambda^3/C^2$ as a function of the reduced frequency $\omega/(U/\Lambda)$ where U is the relative inflow velocity. The results are displayed in Fig. 12.5.

It can be observed that the NM80 measurements collapse quite well with Amiet's model results using the corresponding input data. The results obtained in the LM wind tunnel appear at much lower reduced frequencies due to the large difference in turbulence scales Λ. As expected, the asymptotic behavior of Amiet's model using inflow data for the wind tunnel with turbulence grid does collapse in the high-frequency limit, and ultimately with the NM80 data by extrapolating these curves. As noticed earlier for the BL flow near the TE, the lack of collapse at

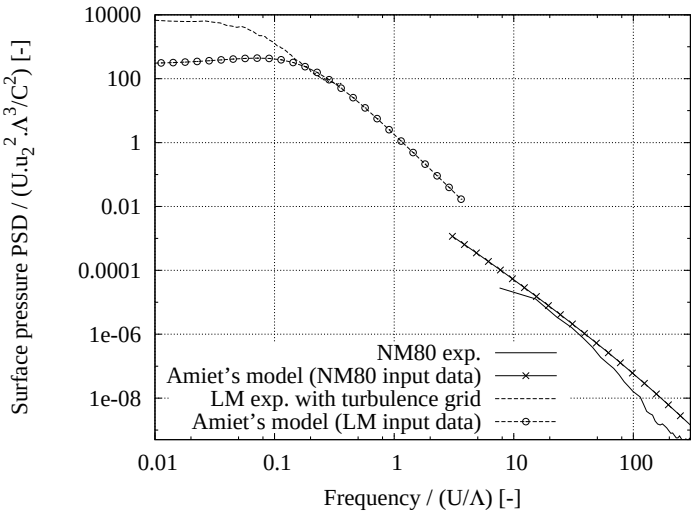

Figure 12.5. Influence of Inflow Turbulence - LE Microphone - $x/C = 2.2\%$ (Pressure side).

lower frequencies may originate from the use of the Von Karman spectrum to define the inflow turbulence and which might not be representative of the actual turbulence characteristics in this part of the spectrum.

In order to illustrate the influence of the increase of inflow turbulence due to the wake of an upstream wind turbine in the case of the NM80 turbine experiment, the following investigation is performed. During the measurement campaign described in Section 12.2.1 the wind changed direction and the NM80 wind turbine eventually stood in the wake of an upwind wind turbine. It is well known that wind turbine generates large scale vortices in their wake, which can be interpreted as a more intense turbulence intensity in the flow impinging the blade. However, it should be kept in mind that wind turbine wakes are also associated with wind velocity deficit due to the energy extracted from the wind by the wind turbine rotor. Nevertheless, since data are sorted out by constraining the time-series with respect to the electrical power generated by the turbine, the actual mean wind velocity experienced by the turbine can be compared to the free-wind case.

This wake situation is used to investigate the influence of turbulence intensity on the SP measurements both at the LE and TE. This is reported in Figs. 12.6(a-b), respectively.

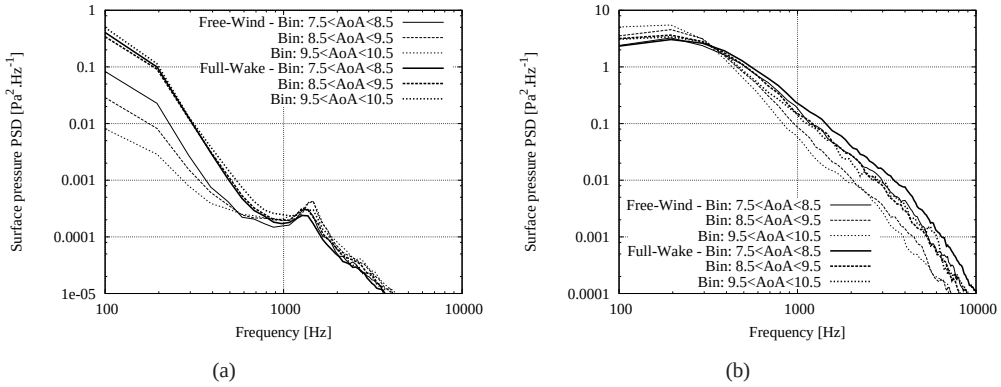

Figure 12.6. NM80 Rotor - Comparison Free-Wind/Wake - AoA Binning: a) LE Microphone - $x/C = 2.2\%$ (Pressure side); b) TE Microphone - $x/C = 93\%$ (Suction side).

The influence of the wake can clearly be observed at the LE with an significant increase of

spectral energy, mainly in the low frequency range. At the TE, the mechanism observed earlier for which the spectral energy of the SP fluctuations is increased at higher frequency and decreased at lower frequency when the inflow becomes turbulent compared to the laminar case, is further amplified in this wake situation where turbulence intensity in the inflow is supposedly also more intense as explained above.

12.5 Conclusions

Surface pressure (SP) measurements related to noise emission on a full-scale wind turbine has been analysed using reference wind tunnel measurements of an airfoil section identical to the one at the blade radius where SP are measured, as well as numerical models including BEM theory and a CFD code for aerodynamic calculations, as well as Amiet's model for TI noise and TNO-Blake model for TE noise modeling. A general good agreement between the model and measurement data is found. However, some discrepancies between the SP measured at the TE on the NM80 wind turbine and the CFD/TNO-Blake model are observed. But these can be explained by the presence of a turbulent inflow impacting the turbine blade which is not accounted for in the model.

In addition, the present study does clarify important issues about wind turbine noise mechanisms. For low frequencies, increasing the AoA yields an increase in SP spectral energy at the TE, and thereby TE noise in the far-field. For high frequencies, the tendency is reversed. The dependence of the inflow noise on AoA variations, which is not accounted for in Amiet's model, has also been highlighted.

The case of a wind turbine operating in wake is also studied. It is shown that SP fluctuations near the LE increase at lower frequencies due to the inflow turbulence associated with the presence of the wake. In contrast, SP measurements at the TE exhibit an increase of spectral energy at higher frequencies, which is a consequence of the different turbulent BL characteristics created at the TE by the inflow turbulence as observed in the wind tunnel.

References

[1] H. Wagner, R Bareiß, and G. Guidati. *Wind Turbine Noise*. Springer, Berlin, 1996.

[2] R.K. Amiet. Noise due to turbulent flow past a trailing edge. *Journal of Sound and Vibration*, 47:387–393, 1976.

[3] M.S Howe. A review of the theory of trailing edge noise. *Journal of Sound and Vibration*, 61:437–465, 1978.

[4] R.K. Amiet. Acoustic radiation from an airfoil in a turbulent stream. *Journal of Sound and Vibration*, 41:407–420, 1975.

[5] R.W. Paterson and R.K. Amiet. Acoustic Radiation and Surface Pressure Characteristics of an Airfoil Due to Incident Turbulence. *Proceedings of the* 3^{rd} *AIAA Aero-Acoustics Conference*, 1976.

[6] H.A. Madsen, C. Bak, U.S. Paulsen, M. Gaunaa, N.N. Sørensen, P. Fuglsang, J. Romblad, N.A. Olesen, P. Enevoldsen, J. Laursen, and L. Jensen. The DANAERO MW Experiments. *AIAA 2010-645, 48th AIAA Aerospace Sciences Meeting and Exhibit, Orlando, Florida*, 2010.

[7] H.Aa. Madsen, C. Bak, U.S. Paulsen, M. Gaunaa, P. Fuglsang, J. Romblad, N.A. Olesen, P. Enevoldsen, J. Laursen, and L. Jensen. The DAN-AERO MW Experiments Final report. Technical Report Risø-R-1726(EN), Technical University of Denmark, 2010.

[8] C. Bak, N. Troldborg, and H.A. Madsen. DAN-AERO MW: Measured airfoil characteristics for a MW rotor in atmospheric conditions. *EWEA, Brussels, Belgium*, 2011.

[9] F. Bertagnolio, H.Aa. Madsen, C. Bak, N. Troldborg, and A. Fischer. Aerodynamic Noise Characterization of Full-Scale Wind Turbine through High-Frequency Surface Pressure Measurements. *Submitted for publication in Journal of Sound and Vibration*, 2013.

[10] H. Glauert. *Airplane Propellers*, volume Aerodynamic Theory Volume IV. W. F. Durand, The Dover Edition (UK), 1963.

[11] N.N. Sørensen. *General Purpose Flow Solver Applied to Flow over Hills*. PhD thesis, Technical University of Denmark, 1995.

[12] J.A. Michelsen. Basis3D - a platform for development of multiblock PDE solvers. Technical report AFM 92-05, Technical University of Denmark, Lyngby, 1992.

[13] J.A. Michelsen. Block structured multigrid solution of 2D and 3D elliptic PDEs. Technical Report AFM 94-06, Technical University of Denmark, 1994.

[14] F.R. Menter. Zonal Two Equation k-ω Turbulence Models for Aerodynamic Flows. *AIAA Journal*, (93-2906), 1993.

[15] M. Drela and M.B. Giles. Viscous-inviscid analysis of transonic and low reynolds number airfoils. *AIAA Journal*, 25, 1987.

[16] R.H. Kraichnan. Pressure fluctuations in turbulent flow over a flat plate. *Journal of the Acoustical Society of America*, 28:378–390, 1956.

[17] W.K. Blake. *Mechanics of Flow-Induced Sound and Vibration: Complex flow-structure interactions*, volume II. Frenkiel, F.N. and Temple, G. (eds.), Academic Press, 1986.

[18] W.K. Blake. *Mechanics of Flow-Induced Sound and Vibration: General concepts and elementary sources*, volume I. Frenkiel, F.N. and Temple, G. (eds.), Academic Press, 1986.

[19] F. Bertagnolio. Experimental Investigation and Calibration of Surface Pressure Modeling for Trailing Edge Noise. *Proceedings of Inter-Noise 2011 Conference*, 2011.

[20] P. Moriarty, G. Guidati, and P. Migliore. Prediction of turbulent inflow and trailing-edge noise for wind turbines. *Proceedings of the* 11^{th} *AIAA/CEAS Aeroacoustics Conference, AIAA Paper 2005-2881*, 2005.

[21] R.L. Panton and J.H. Linebarger. Wall pressure spectra calculations for equilibrium boundary layers. *Journal of Fluid Mechanics*, 65:261–287, 1974.

[22] D.A. Lynch, W.K. Blake, and T.J. Mueller. Turbulence correlation length-scale relationships for the prediction of aeroacoustics response. *AIAA Journal*, 43:1187–1197, 2005.

[23] T. Lutz, A. Herrig, W. Würz, M. Kamruzzaman, and E. Krämer. Design and wind-tunnel verification of low-noise airfoils for wind turbines. *AIAA Journal*, 45:779–785, 2007.

[24] T.F. Brooks and T.H. Hodgson. Trailing Edge Noise Prediction from Measured Surface Pressures. *Journal of Sound and Vibration*, 78:69–117, 1981.

[25] R.K. Amiet. Noise produced by turbulent flow into a propeller or helicopter rotor. *Proceedings of the* 3^{rd} *AIAA Aero-Acoustics Conference*, 1976.

[26] F. Bertagnolio. WNACA0015 Measurements in LM Wind Tunnel and Turbulence Generated Noise. Technical Report Risø-R-1657(EN), Risø-DTU, Roskilde, Denmark, 2008.

[27] M. Døssing. High Frequency Microphone Measurements for Transition Detection on Airfoils. Technical Report Risø-R-1645(EN), Risø-DTU, Roskilde, Denmark, 2008.

[28] A Fischer. Hot wire anemometer turbulence measurements in the wind tunnel of lm wind power. Technical Report DTU Wind Energy Report E-0006(EN), DTU Wind Energy, Roskilde, Denmark, 2012.

Part III: Validation of models

13 Validation of Amiet's turbulent inflow noise model and the TNO Blake trailing edge model

Author(s): F. Bertagnolio, H.A. Madsen, C. Bak, N. Troldborg, A. Fischer

The Amiet model for computation of noise from inflow turbulence and the TNO model for TE noise, described in section 12.3 will now be validated against microphone results on the NM80 rotor as well as on the blade section in the LM wind tunnel. The SP measurements on the NM80 rotor were aquired at 37m̃ radius and on the NACA 63-418 airfoil in the LM wind tunnel, respectively.

13.1 Analysis of Surface Pressure Fluctuations

The validation of the models is carried out through a comparison of the influence of various parameters on the surface pressure fluctuations.

13.1.1 Influence of Microphone Chord Location

The influence of the location of the microphone along the airfoil chord near the LE of the NM80 turbine blade (at $r = 37$ m) on the SP spectra at a given AoA is studied first. The SP spectra at two chord locations on the pressure side of the airfoil, $x/C = 1.2\%$ and 2.2% respectively, are shown in Fig. 13.1(a). As predicted by Amiet's model, the measured data show a decrease

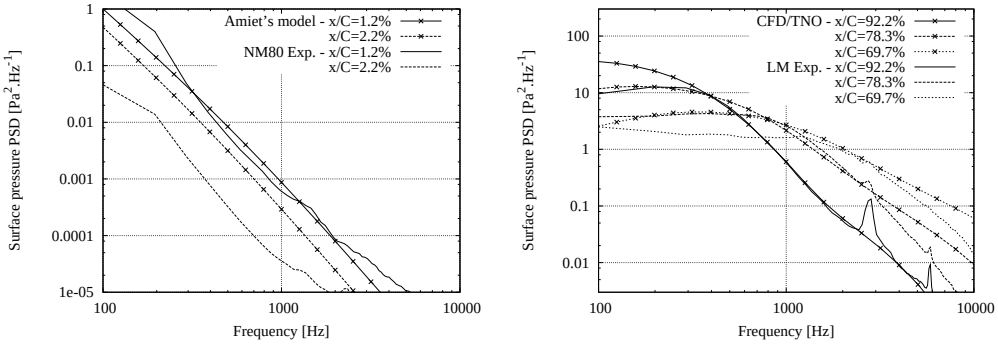

Figure 13.1. Influence of Microphone Chord Location on SP Spectra: a) NM80 Rotor - SP Spectra near LE (Pressure side); b) NACA 63-418 - SP Spectra near TE (Suction side).

of the SP fluctuation amplitudes at all frequencies as the distance from the LE increases. It should be noted that in the case of the measured data, if the distance from the LE is further increased then the SP amplitude starts to increase again. This is caused by the amplification of disturbances in the laminar BL yielding further downstream to transition and ultimately to a fully developed turbulent BL in which SP fluctuations will dominate TI generated ones [1].

As for microphones located near the TE, SP spectra are analyzed for microphones located on the suction side of the NACA 63-418 airfoil section at $x/C = 92.2$, 78.3 and 69.7%. Measurements performed in the LM Wind Power wind tunnel are compared to CFD/TNO-Blake model results, both at an AoA equal to 10^o, in Fig. 13.1(b). The decrease and increase of SP fluctuation amplitudes at higher and lower frequencies, respectively, as the TE is approached are very well reproduced by the model. In this figure, spurious peaks in the measured spectra can be

observed around 3000 Hz (and a harmonic at approximately 6000 Hz). These are the result of noise disturbances present in the wind tunnel and generated by the driving fan.

13.1.2 Influence of Local Angle of Attack

Fig. 13.2(a) shows the the SP spectra measured on the NM80 rotor blade at $x/C = 2.2\%$ on the pressure side of the airfoil for various AoA. The SP fluctuations energy decreases slightly with increasing AoA for frequencies below 600 Hz, and vice-versa above. Such phenomenon was also reported for some non-symmetric airfoils in the work by Devenport *et al* [2]. However, Amiet's theory [3] used in the present TI noise model cannot explain this phenomenon.

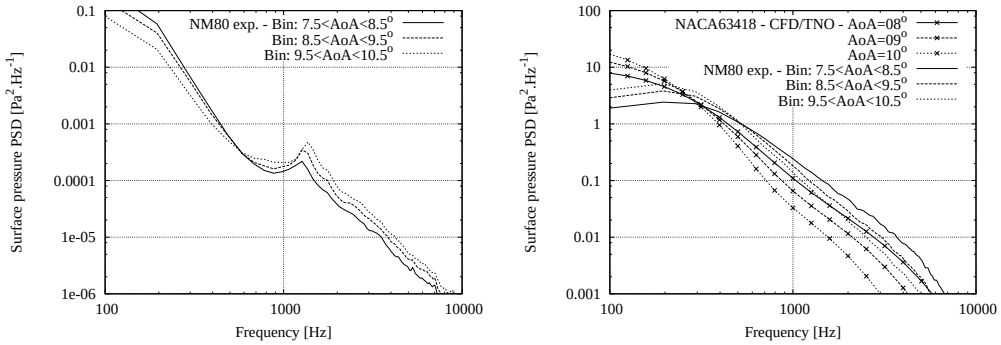

Figure 13.2. NM80 Rotor (vs. CFD/TNO-Blake Model for SP near TE) - Influence of AoA: a) SP Spectra near LE ($x/C = 2.2\%$, Pressure side); b) SP Spectra near TE ($x/C = 93\%$, Suction side).

The case of the SP spectra at the TE is considered next. In order to validate the CFD/TNO-Blake model the SP spectra measured in the wind tunnel on the NACA 63-418 airfoil section are investigated. Fig. 13.3 displays both the modeled and measured SP spectra near the TE of the airfoil ($x/C = 92.2\%$) for a Reynolds number $Re = 5 \times 10^6$ and for three different AoAs. There exists a good quantitative agreement between model results and experimental values that

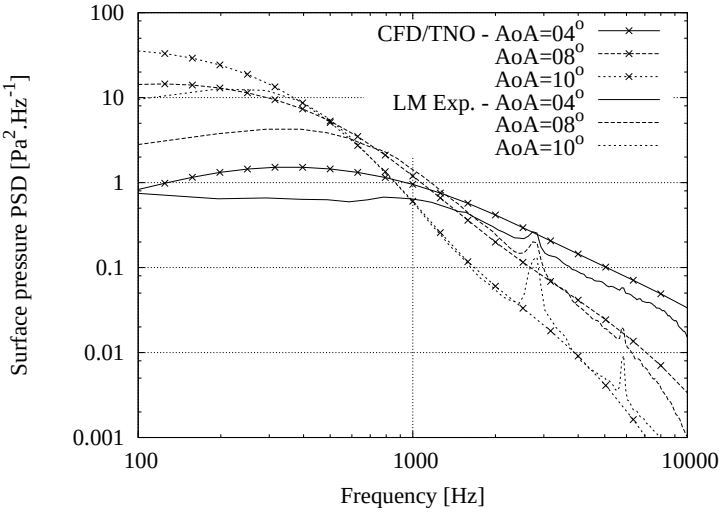

Figure 13.3. NACA63-418 (LM Wind Tunnel Exp. vs. CFD/TNO-Blake) - SP Spectra near TE ($x/C = 92.2\%$, Suction side).

deteriorates at low frequencies. The modeling at such frequencies by the TNO-Blake model is

however dubious. Indeed, the turbulence content of the BL flow is most probably not correctly estimated by the Von Karman spectrum used to describe the flow at the corresponding low wavenumbers (see Section 12.3.2). Another possible explanation for the discrepancies observed at low frequencies for the TNO-Blake model is the fact that a stratification of uncorrelated turbulent vortex sheets across the turbulent BL is assumed [4, 5]. At low wave numbers, the size of the involved turbulent vortices become non-negligible compared to the BL thickness and the above assumption breaks down.

SP spectra measured on the NM80 rotor near the TE at 37 m radius of its LM 38.8 blade are now considered. The microphone used for this SP analysis is located at 93% of the chord on the suction side. Three different bins of equal sizes and based upon the calibrated measured AoA at 31 m radius are defined as:

$$7.5 < \alpha < 8.5^o \qquad \text{and} \qquad 8.5 < \alpha < 9.5^o \qquad \text{and} \qquad 9.5 < \alpha < 10.5^o$$

According to the analysis conducted in Section 12.2.4, the AoA can be binned according to its values measured at 31 m radius and the corresponding AoA at 37 m radius should be approximately the same.

CFD RANS calculations of the NACA63-418 airfoil are performed at a Reynolds number $Re = 5 \times 10^6$, which corresponds to the value calculated by the BEM method, and SP spectra were calculated using the modified TNO-Blake model described earlier. Note that the model results are more sensitive to the amplitude of the relative inflow velocity impinging on the airfoil through the AoA dependence, than to small variations of the actual Reynolds number of the flow. The AoAs used to perform the RANS calculations are 8^o, 9^o and 10^o. These correspond, respectively, to the centers of the bins defined above for the analysis of rotor pressure coefficient and turbulent SP measurements. The relative inflow velocities are those calculated by averaging in the binning process for each of the specific AoA bin. The results are displayed in Fig. 13.2(b). As it can be seen, there exists a shift between the measured and modeled spectra, though the increase and decrease of SP fluctuation amplitudes at lower and higher frequencies, respectively, as a function of the AoA is consistently predicted. This suggests that some phenomenon that is not accounted for in the present CFD/TNO-Blake model does occur on the actual blade. Such a phenomenon was brought to light in section 12.4.3.

13.2 Conclusions

Surface pressure (SP) measurements related to noise emission on a full-scale wind turbine has been analysed using reference wind tunnel measurements of an airfoil section identical to the one at the blade radius where SP are measured, as well as numerical models including BEM theory and a CFD code for aerodynamic calculations, as well as Amiet's model for TI noise and TNO-Blake model for TE noise modeling. A general good agreement between the model and measurement data is found. However, some discrepancies between the SP measured at the TE on the NM80 wind turbine and the CFD/TNO-Blake model are observed. But these can be explained by the presence of a turbulent inflow impacting the turbine blade which is not accounted for in the model. It was also found that for both TI and TE noise models, the use of the Von Karman spectrum for describing the respective turbulence characteristics may be source of errors at very low frequencies. For the TE noise model, the assumption of uncorrelated vortex sheets across the turbulent BL may also yield poor results at low frequencies.

References

[1] M. Døssing. High Frequency Microphone Measurements for Transition Detection on Airfoils. Technical Report Risø-R-1645(EN), Risø-DTU, Roskilde, Denmark, 2008.

[2] W.J. Devenport, J.K. Staubs, and S.A.L. Glegg. Sound radiation from real airfoils in turbulence. *Journal of Sound and Vibration*, 329:3470–3483, 2010.

[3] R.K. Amiet. Acoustic radiation from an airfoil in a turbulent stream. *Journal of Sound and Vibration*, 41:407–420, 1975.

[4] W.K. Blake. *Mechanics of Flow-Induced Sound and Vibration: Complex flow-structure interactions*, volume II. Frenkiel, F.N. and Temple, G. (eds.), Academic Press, 1986.

[5] W.K. Blake. *Mechanics of Flow-Induced Sound and Vibration: General concepts and elementary sources*, volume I. Frenkiel, F.N. and Temple, G. (eds.), Academic Press, 1986.

14 Comparison of CFD rotor simulations with DANAERO measurements

Author(s): N.N. Sørensen, N. Troldborg, J. Johansen, J. Madsen, P-E Réthoré

This chapter presents a comparison of full rotor simulations using Computational Fluid Dynamics (CFD) with measurements from the DANAERO MW experiment. The study is a part of a validation study carried out in the project "Center for Computational Wind Turbine Aerodynamics and Atmospheric Turbulence" contract no.: 2104-09-0026. Simulations have been carried out by DTU Wind Energy, Siemens Wind Power and LM Wind Power, respectively so that a inter comparison between the different Navier Stokes solvers and grids can be made.

14.1 Introduction

Even though Computational Fluid Dynamics (CFD) of wind turbines, in which the geometry of the rotor is fully resolved, generally have proven to predict loads and power production on wind turbines quite accurately, this type of simulations still need further validation. One major uncertainty is that these types of simulations mostly are restricted to non-turbulent, steady inflow conditions. Also the transition modelling in particular in 3D CFD is uncertain. In this work a number of CFD rotor simulations using different flow solvers and grids are validated by comparing them to each other and to measurements obtained as part of the DANAERO MW experiment.
The present work only considers the turbine operating in non-sheared inflow. Though this is the simplest possible case the comparison will still reveal the importance of inflow turbulence and the necessity of including laminar/turbulent transition modelling at realistic Reynolds numbers.

14.2 Measurements

As part of the DANAERO MW project comprehensive inflow and load measurements were conducted on the NM80 wind turbine located at the Tjæreborg Enge site in Denmark [1]. From the extensive campaign the present work primarily uses the blade surface pressures measured at the four sections $r = 13\ m, 19\ m, 30\ m$ and $37\ m$ of the $40\ m$ long blade. The aerodynamic forces parallel and perpendicular to the chord line in each section is subsequently computed by integrating the chordwise pressure distributions.
For the purpose of validation specific benchmark cases has been selected from the measurements as described in [2]. The selected test cases include situations where the turbine is operating in non-sheared, sheared and yawed inflow conditions. However, the present work only uses the measurements in the non-sheared inflow case. For this case the inflow and operational conditions are as shown in Table 14.1. **It should be emphasized that the turbine is operating at nearly constant rotational speed and pitch in the used dataset.** The reason for choosing a case where the turbine control activity is very limited is that it is easier to simulate.

U_0 [m/s]	TI [%]	α [-]	Ω [RPM]	pitch [^{o}]	Yaw error [^{o}]
6.1	6.8	0.025	12.3	0.15	-0.6

Table 14.1. Measured inflow and operational conditions. U_0 is the mean velocity at hub height, TI the turbulence intensity, α the power law shear exponent and Ω the rotational speed of the rotor.

14.3 Computations

Simulations of the NM80 turbine have been carried out by DTU Wind Energy, Siemens Wind Power and LM Wind Power, respectively. A grid was generated by DTU Wind Energy to be used by all participant involved in the comparison study. However, LM Wind Power ended up using a different grid, which closer resembled the type of grid that they normally use for rotor simulations. This grid still contained the same number of grid points as the one provided by DTU Wind Energy.

14.3.1 Grid

The reference grid provided by DTU Wind Energy has a standard O-O mesh configuration. The radius of the domain is approximately 10 rotor diameters and the height of the first cell adjacent to the blade surface is set to satisfy the condition $y^+ < 1$ as required for this type of computations. The blades of the turbines are resolved with $256 \times 128 \times 128$ cells in the chordwise, spanwise and normal direction, respectively. The grid consists of 432 block of 32^3 ($14 \cdot 10^6$) grid cells.

14.3.2 Navier-Stokes solvers

The incompressible finite volume Reynolds Averaged Navier-Stokes (RANS) flow solver EllipSys3D [3–5] was used by both DTU Wind Energy and LM Wind Power, while Siemens Wind Power used the commercial CFX code.

14.3.3 Simulation setup

All simulations were carried out assuming steady and uniform inflow, i.e. neglecting turbine tilt as well as the small shear and yaw error present in the measurements. Turbulence was in all cases modelled using the $k-\omega$ SST turbulence model by Menter [6]. Simulations were carried out assuming both fully turbulent (ft) and transitional (tr) boundary layer flow. In addition to the case specified in Table 14.1 simulations were also carried out at inflow velocities of $U_0 = 8\ m/s$ and $U_0 = 12\ m/s$, respectively keeping all other parameters as in Table 14.1.

14.4 Results

14.4.1 Grid study

Before distributing the reference grid a thorough study was made to quantify grid dependency. In the study the overall layout was the same while the number of grid points was varied successively using the build in grid sequencing in EllipSys3D. The results of the study is shown in Table 14.2. Grid $C1$ refer to the reference grid. As seen both the shaft torque and thrust predicted on the reference grid are in close agreement to the corresponding predictions on the finer grids showing that the solutions presented in the following are grid independent.

14.4.2 Comparison of simulations

Table 14.3 shows a comparison of the simulated mechanical power predicted by the participants in the various cases. Generally, the differences between the computations at the same wind speed are very small. All simulations suggest that transition modelling do affect the power production.

Grid level	Cells	LSSTQ [Nm]	Thrust [N]
S4	$0.4 \cdot 10^6$	$250.47 \cdot 10^3$	$9.500 \cdot 10^4$
S3	$3.6 \cdot 10^6$	$247.38 \cdot 10^3$	$9.344 \cdot 10^4$
S2	$28 \cdot 10^6$	$244.19 \cdot 10^3$	$9.246 \cdot 10^4$
S1	$226 \cdot 10^6$	$244.14 \cdot 10^3$	$9.186 \cdot 10^4$
C1	$14 \cdot 10^6$	$243.55 \cdot 10^3$	$9.188 \cdot 10^4$

Table 14.2. Results of the grid dependency study

U_0 [m/s]	6.1	8.0	12.0
LM (ft)	$3.07 \cdot 10^5$	-	-
LM (tr)	$3.25 \cdot 10^5$	-	-
Siemens (ft)	$3.13 \cdot 10^5$	$6.71 \cdot 10^5$	$1.61 \cdot 10^6$
Siemens (tr)	$3.45 \cdot 10^5$	$7.41 \cdot 10^5$	$1.88 \cdot 10^6$
DTU (ft)	$3.12 \cdot 10^5$	$6.86 \cdot 10^5$	$1.66 \cdot 10^6$
DTU (tr)	$3.39 \cdot 10^5$	-	-

Table 14.3. Mechanical power [W] predicted in the various simulations assuming fully turbulent (ft) and transitional (tr) flow respectively.

14.4.3 Comparison with measurements

Figure 14.1 and 14.2 compares the measured aerodynamic forces along the blade with the corresponding forces predicted from simulations assuming fully turbulent and transitional boundary layer flow, respectively. The errorbars on the measurements indicate the standard deviation of the measurements and thus can be considered a measure of the uncertainty in the comparison. Generally, the computed normal forces are higher than measured, while the opposite is

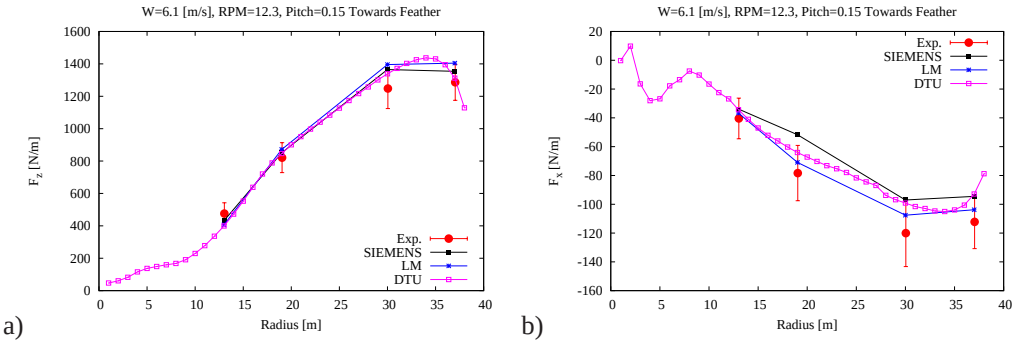

Figure 14.1. Comparison of measurements and fully turbulent computations of normal (a) and tangential (b) aerodynamic forces at $U_0 = 6.1\ m/s$

true for the tangential forces. However, since the computations in most cases lies within the errorbar of the measurements the agreement is satisfactory.
Including transition modelling improves slightly the agreement between measured and computed tangential force, while the agreement slightly worsens for the normal forces.
To get a better impression of the influence of transition modelling Figure 14.3 shows forces simulated by DTU Wind Energy assuming both fully turbulent and transitional boundary layer flow in comparison with measurements. The transition modelling mostly affects the loads on the inboard sections. It seems that including transition modelling improves the agreement between measured and computed forces at the most inboard section. Unfortunately, the measurements are not conducted far enough inboard to completely verify whether the effect of the transition model to increase significantly the tangential force at the spanwise position from approximately

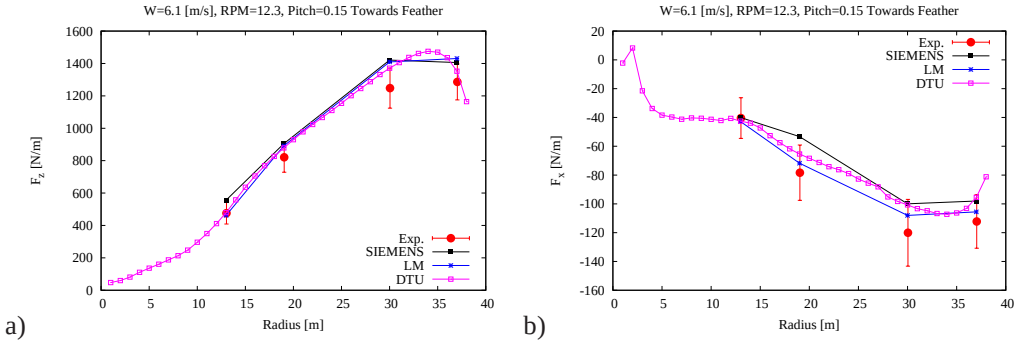

Figure 14.2. Comparison of measurements and computations including transition modelling of normal (a) and tangential (b) aerodynamic forces at $U_0 = 6.1\ m/s$

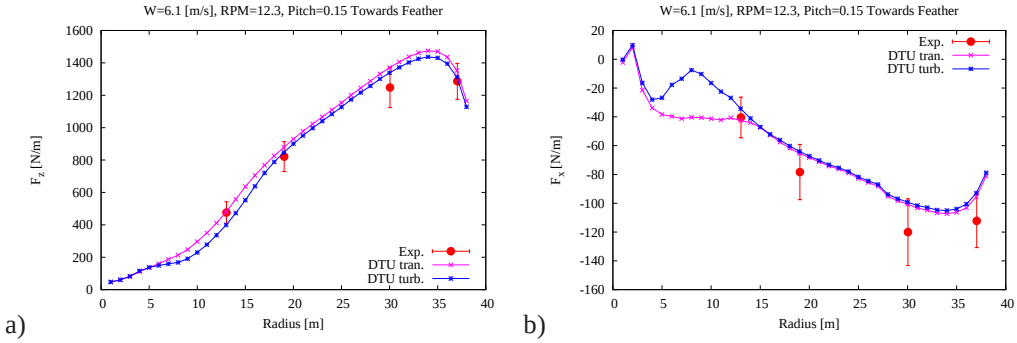

Figure 14.3. Comparison of measurements and the computations by DTU Wind Energy of normal (a) and tangential (b) aerodynamic forces at $U_0 = 6.1\ m/s$

$r = 5\ m$ to $r = 12\ m$ is reflected in the measurements.

Figure 14.4 compares measured and computed pressure coefficient distributions at each of the four blade sections. The pressure coefficient is defined as:

$$C_p = \frac{p_\infty - p}{\frac{1}{2}\rho V_{rel}^2}$$

where C_p is the normalized pressure, p_∞ is the static pressure [Pa] in the far field, p is the pressure [Pa] measured at the blade surface, ρ is the air density $[kg/m^3]$ and V_{rel} is the relative velocity [m/s]. In the measurements V_{rel} is determined from the rotational speed and the velocity at the nearby met mast. In general the agreement is quite good for all sections. The figure confirms that the agreement between measurements and computations is improved at the most inboard section by the inclusion of transition modelling, whereas it is difficult to say whether an improvement is achieved at the outer sections.

14.5 Conclusion

A comparison of field measurements and computations of aerodynamic forces and surface pressure distributions at four blade sections of the NM80 turbine operating in nearly non-sheared inflow has been conducted. The results generally show good agreement when considering the standard deviation of the measurements. Simulations were carried out assuming both fully turbulent and transitional flow over the blade boundary layer with the aim of validating the transition model against measurements. However, with the spread in the used measurements it was hard to conclude whether laminar or turbulent computations produces the best results.

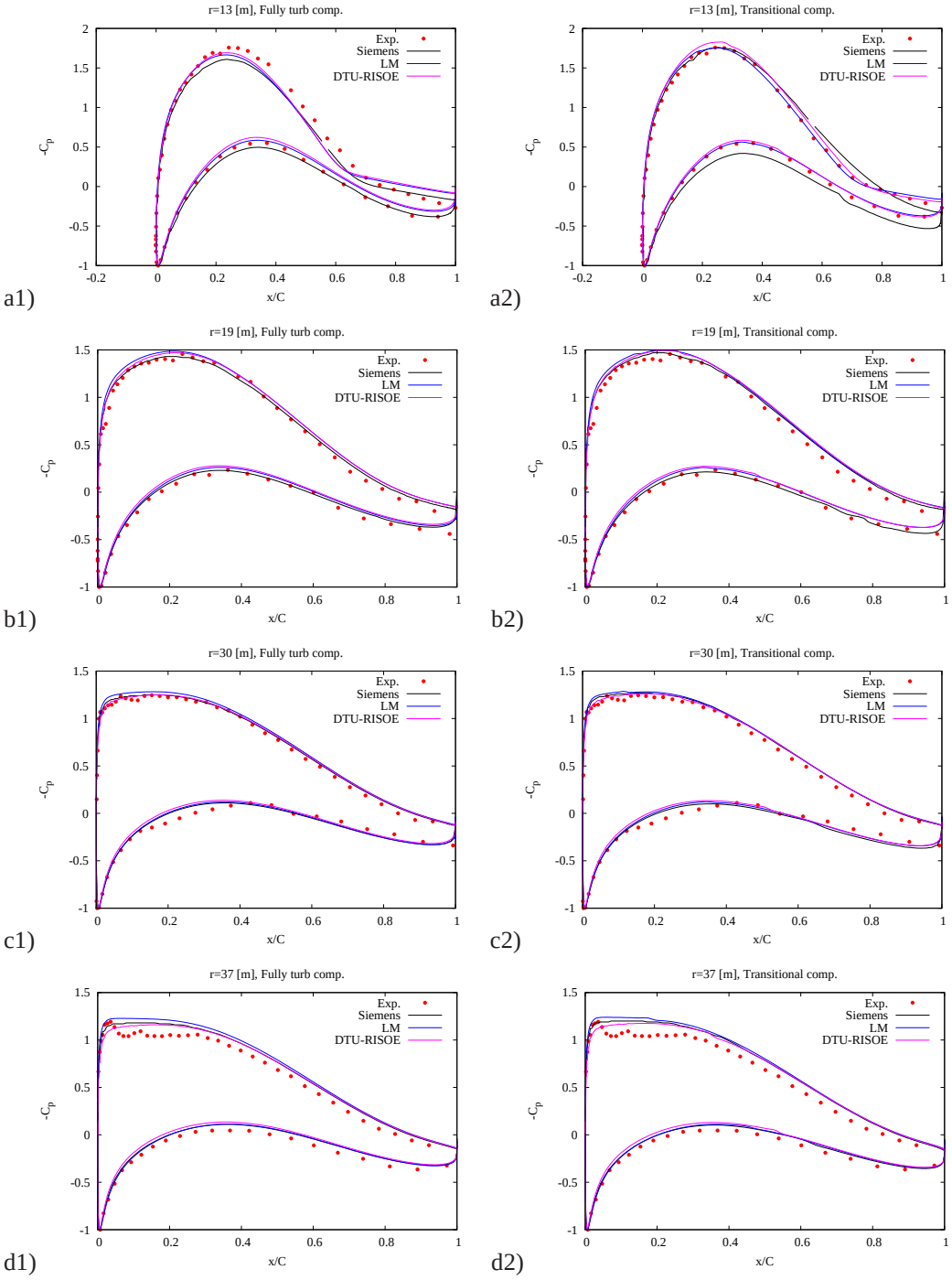

Figure 14.4. Comparison of measured and computed pressure coefficient distributions at $U_0 = 6.1\ m/s$. *a)* $r = 13\ m$; *b)* $r = 19\ m$; *c)* $r = 30\ m$; *d)* $r = 37\ m$. *Left plots: fully turbulent computations; Right plots: Transitional computations*

All simulations were carried out assuming steady and uniform inflow and the good agreement between measurements and simulations thus indicate that most of the flow physics can be captured without considering the relatively high inflow turbulence in the measurements of TI=6%.

References

[1] C. Bak, H.Aa. Madsen, N. Troldborg, M. Gaunaa, W. Skrzypiński, A. Fischer, U. Paulsen, R. Møller, P. Hansen, M. Rasmussen, and P. Fuglsang. DANAERO MW: Instrumentation of the NM80 turbine and meteorology mast at Tjæreborg . Technical Report DTU Wind Energy Report-I-0083, Technical University of Denmark, 2013.

[2] N. Troldborg. DAN-AERO MW: Potential benchmark cases from the Tjæreborg campaign. Technical Report DTU Wind Energy Report-I-0090, DTU Wind Energy, 2013.

[3] J.A. Michelsen. Basis3D - a platform for development of multiblock PDE solvers. Technical report AFM 92-05, Technical University of Denmark, Lyngby, 1992.

[4] J.A. Michelsen. Block structured multigrid solution of 2D and 3D elliptic PDEs. Technical Report AFM 94-06, Technical University of Denmark, 1994.

[5] N.N. Sørensen. *General Purpose Flow Solver Applied to Flow over Hills*. PhD thesis, Technical University of Denmark, 1995.

[6] F.R. Menter. Zonal Two Equation k-ω Turbulence Models for Aerodynamic Flows. *AIAA Journal*, (93-2906), 1993.

15 Comparison of BEM simulations with DANAERO measurements

Author(s): N. Troldborg, C. Bak, D. Veldkamp, J. Johansen, J. Madsen

This chapter presents a comparison of various Blade Element Momentum (BEM) simulations with measurements from the DANAERO MW experiment. Simulations have been carried out by DTU Wind Energy, Vestas Wind Systems, Siemens Wind Power and LM Wind Power, respectively so that in addition to validating the codes against measurements an inter comparison between the different BEM models could also be made.

15.1 Introduction

Models based on the Blade Element Momentum (BEM) theory are the most commonly used by industry for predicting aerodynamic loads on wind turbines. While these models generally predict power output and loads quite well in simple inflow conditions they may perform less favourably in more complex inflow conditions [1]. Thus, these models along with their sub models for e.g. tip correction, dynamic induction, dynamic stall and 3D aerofoil data correction still need further validation. In this work a number of BEM computations using different models are validated by comparing them to each other and to measurements obtained as part of the DANAERO MW experiment.

15.2 Measurements

As part of the DANAERO MW project comprehensive inflow and load measurements were conducted on the NM80 wind turbine located at the Tjæreborg Enge site in Denmark [2]. From the extensive campaign the present work uses the following data:

- Surface pressures measured at the four sections $r = 13\ m, 19\ m, 30\ m$ and $37\ m$ of the 40 m long blade. The aerodynamic forces parallel and perpendicular to the chord line in each section is subsequently computed by integrating the chordwise pressure distributions.
- Shaft torque

For the purpose of validation specific benchmark cases has been selected from the measurements as described in [3]. In selecting the cases focus was put on datasets where the operational conditions were favourable for model comparisons, i.e. constant rotor speed, yaw and pitch position. Thus, the instrumented turbine was generally not operating in automatic (normal) mode in the periods where the data was extracted. The selected test cases include situations where the turbine is operating in non-sheared, sheared and yawed inflow conditions. The inflow and operational conditions of each of the tested cases are shown in Table 15.1.

15.3 Computations

The BEM simulations of the NM80 turbine have been carried out by DTU Wind Energy, Vestas Wind Systems, Siemens Wind Power and LM Wind Power. DTU Wind Energy used the HAWC2Aero code [4] for the BEM computations, which is a simplified version of the aeroelastic model HAWC2, whereas Vestas Wind Systems, LM Wind Power and Siemens Wind Power used BEM codes developed in-house for their simulations.

The same aerofoil and blade data were used by all participants so that any differences in predictions are due to differences in the used BEM codes only. The aerofoil data were obtained in

Case	U_0 [m/s]	TI [%]	α [-]	Ω [RPM]	pitch [^{o}]	Yaw error [^{o}]
1	6.1	6.8	0.025	12.3	0.15	-0.6
2	10.5	3.0	0.33	16.2	-4.75	-1.3
3	10.3	3.3	0.20	16.2	-4.74	-17.1
4	8.4	4.4	0.28	16.2	-4.75	-38.6
5	7.8	4.7	0.22	16.2	-4.75	-61.5

Table 15.1. Measured inflow and operational conditions in the considered cases. U_0 is the mean velocity at hub height, TI the turbulence intensity, α the power law shear exponent and Ω the rotational speed of the rotor.

the LM Wind Power wind tunnel [5] and corrected for 3D effects using the method of Bak et al. [6], whereas the used blade data is as described in [7].

15.4 Results

15.4.1 Non-sheared inflow

Figure 15.1 compares the measured aerodynamic forces along the blade with the corresponding forces predicted from simulations in the non-sheared inflow case. The errorbars on the measurements indicate the standard deviation of the measurements. Note, that all loads have been normalized as follows:

$$F^* = \frac{F}{\bar{F}_{max,DTU}} \tag{14}$$

where $\bar{F}_{max,DTU}$ is the maximum value of the azimuthally averaged spanwise force predicted by DTU. The model predictions of both tangential and normal forces are seen to be in quite good

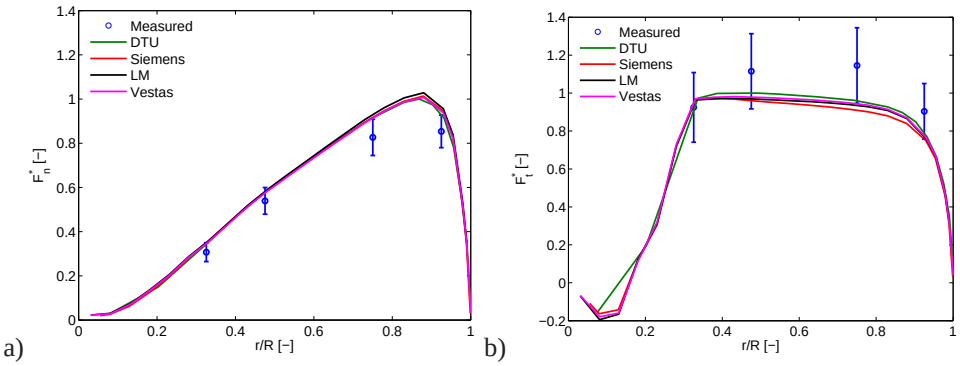

a) b)

Figure 15.1. Comparison of measurements and BEM computations of normal (a) and tangential (b) aerodynamic forces in non-sheared inflow at $U_0 = 6.1\ m/s$

agreement with each other for this case. This is further confirmed in Table 15.2, where it is seen that the differences in predicted power, torque and thrust, respectively are very small. Generally, the computed normal forces are higher than measured, while the opposite is true for the tangential forces. However, the computations still lie within the errorbars of the measurements in most cases and therefore the agreement can be considered satisfactory. The uncertainty in the measurements is also reflected in the fact that the measured torque is slightly lower than the computed torque. From the comparison of the tangential loads the opposite should be expected.

	P/P_{DTU} [-]	τ/τ_{DTU} [-]	T/T_{DTU} [-]
Measured	0.996	0.978	-
Vestas	1.007	1.007	1.002
LM	1.002	1.002	1.021
Siemens	0.984	0.984	1.016
DTU	1.000	1.000	1.000

Table 15.2. Mechanical power, torque and thrust in non-sheared inflow normalized with predictions by DTU

15.4.2 Sheared inflow

Figure 15.2 and 15.3 compare the measured aerodynamic forces along the blade at different azimuth positions with the corresponding forces predicted by Vestas Wind Systems and DTU Wind Energy in the sheared inflow case. Again the errorbars on the measurements indicate the standard deviation of the measurements. Note that an azimuth position of 0^o corresponds to the blade pointing vertically upwards. Due to a broken tube connection, the pressure tap measurements on the two outer sections were corrupted and hence no forces have been computed for these sections. The simulated normal forces are seen to be in good agreement with each other for all azimuth positions. The simulated tangential forces agree well when the blade is in the horizontal positions whereas larger differences are seen in the two vertical positions.
Generally, the agreement between the measured and computed results is rather good, though the simulations tend to under predict the normal loads at $r = 19\,m$. The measured and simulated

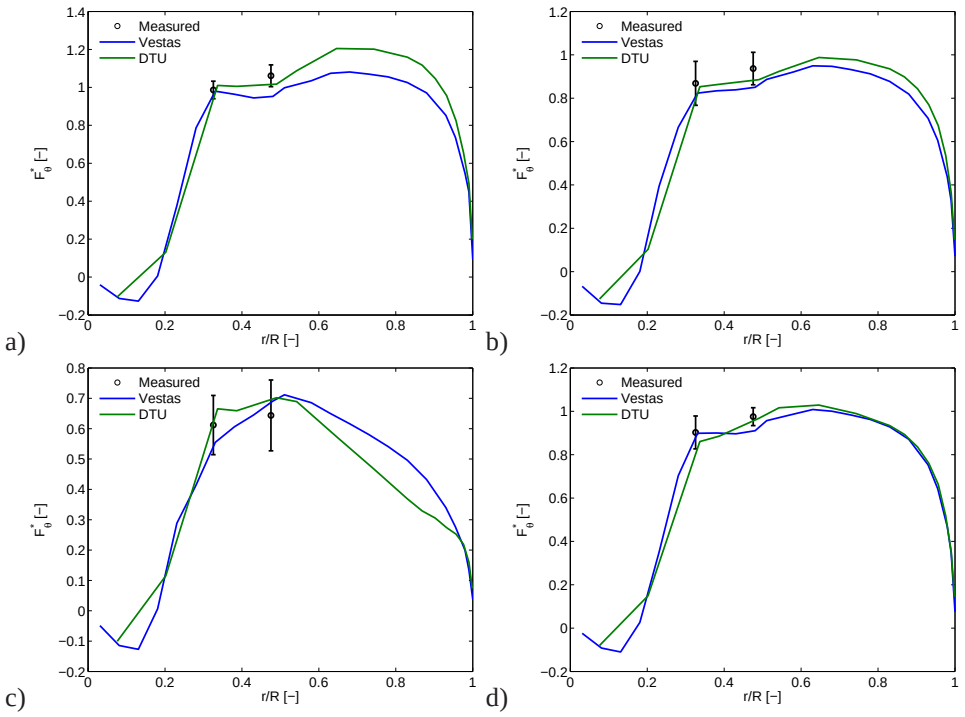

Figure 15.2. Spanwise distribution of measured and computed tangential loads at four blade positions in sheared inflow. a) 0^o (vertical upwards); b) 90^o; c) 180^o; d) 270^o.

torque, thrust and power are shown in Table 15.3. Whereas the simulations agree well in their predictions of both torque and thrust, the torque deviates significantly from what is measured. The reason for this is not known yet but is not reflected in the load measurements.

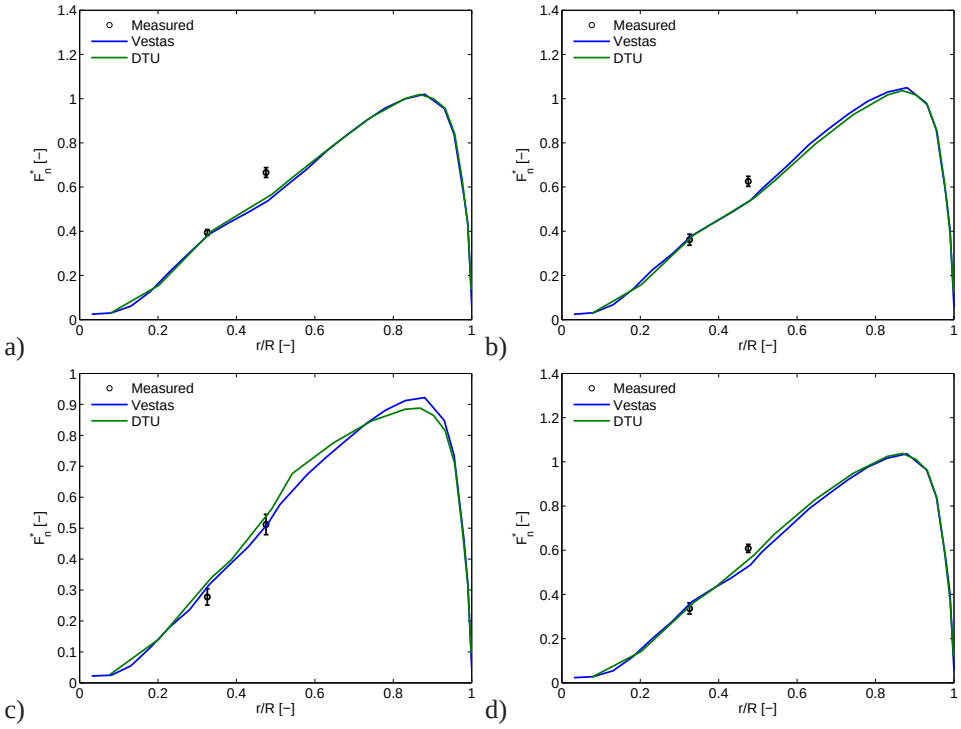

Figure 15.3. Spanwise distribution of measured and computed normal loads at four blade positions in sheared inflow. a) 0^o (vertical upwards); b) 90^o; c) 180^o; d) 270^o.

	P/P_{DTU} [-]	τ/τ_{DTU} [-]	T/T_{DTU} [-]
Measured	1.179	1.177	-
Vestas	1.010	1.010	1.009
DTU	1.000	1.000	1.000

Table 15.3. Mechanical power, torque and thrust in sheared inflow normalized with predictions by DTU

15.4.3 Yawed inflow

Figures 15.4-15.9 compare measurements of aerodynamic forces along the blade at different azimuth positions in the three considered yawed inflow cases with simulations by Vestas Wind Systems and DTU Wind Energy. In the case with a yaw error of -17.1^o there are no measurements available for the two outer most sections because of a broken tube connection to the pressure taps here. The other two cases also suffered from bad pressure measurements at the two outer sections. However, in these cases it was possible to recover the pressure distribution using the method described in [2]. Nevertheless, the measurements at the two outer sections are probably less reliable than at the two inboard sections and therefore should be interpreted with caution. In all cases the overall level of the computed blade forces agree quite well with the measurements but there are large differences in the azimuthal behaviour. In the case with a yaw error of -17.1^o the normal loads predicted by Vestas Wind Systems and DTU Wind Energy agree quite well at all blade positions whereas larger discrepancies are seen for the tangential loads.

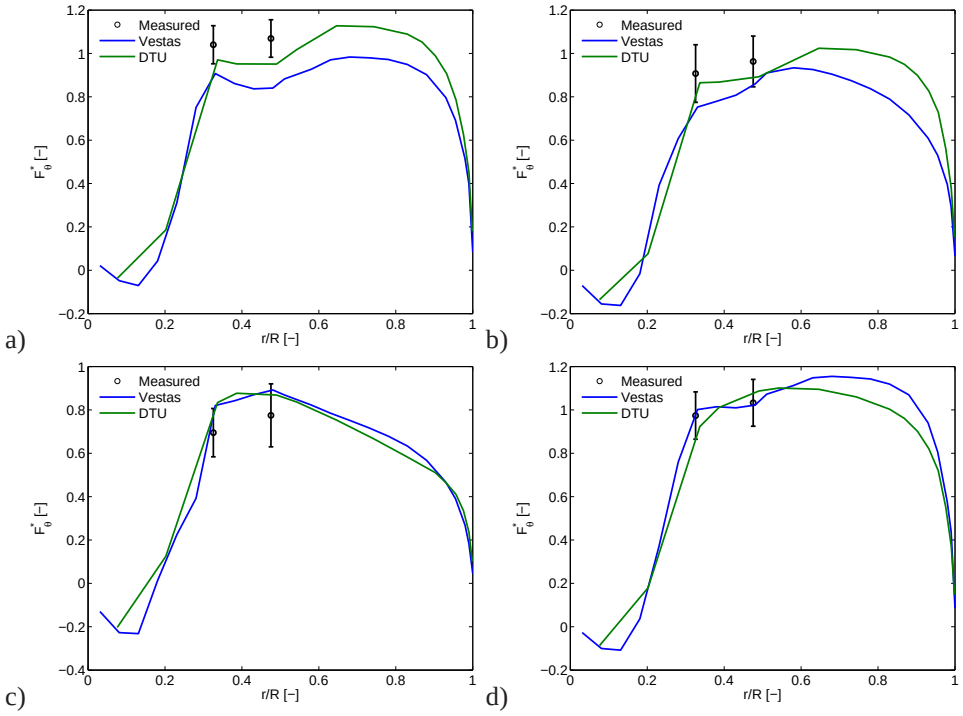

Figure 15.4. Measured and computed tangential loads at four blade positions in the case with a yaw error of -17.1^o*. a)* 0^o *(vertical upwards); b)* 90^o*; c)* 180^o*; d)* 270^o*.*

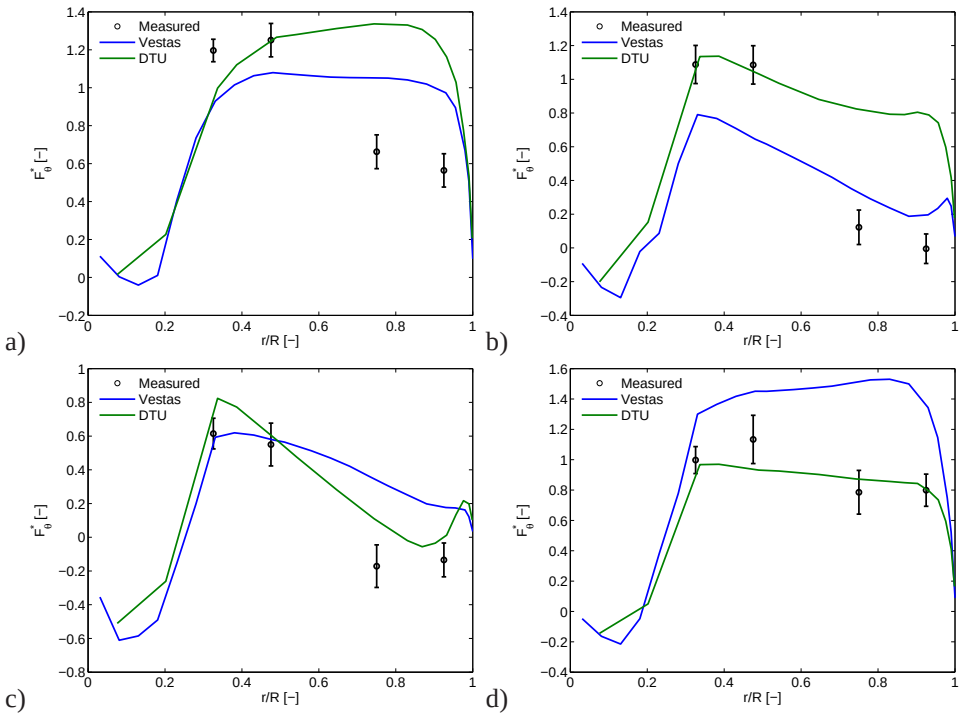

Figure 15.5. Measured and computed tangential loads at four blade positions in the case with a yaw error of -38.6^o*. a)* 0^o *(vertical upwards); b)* 90^o*; c)* 180^o*; d)* 270^o*.*

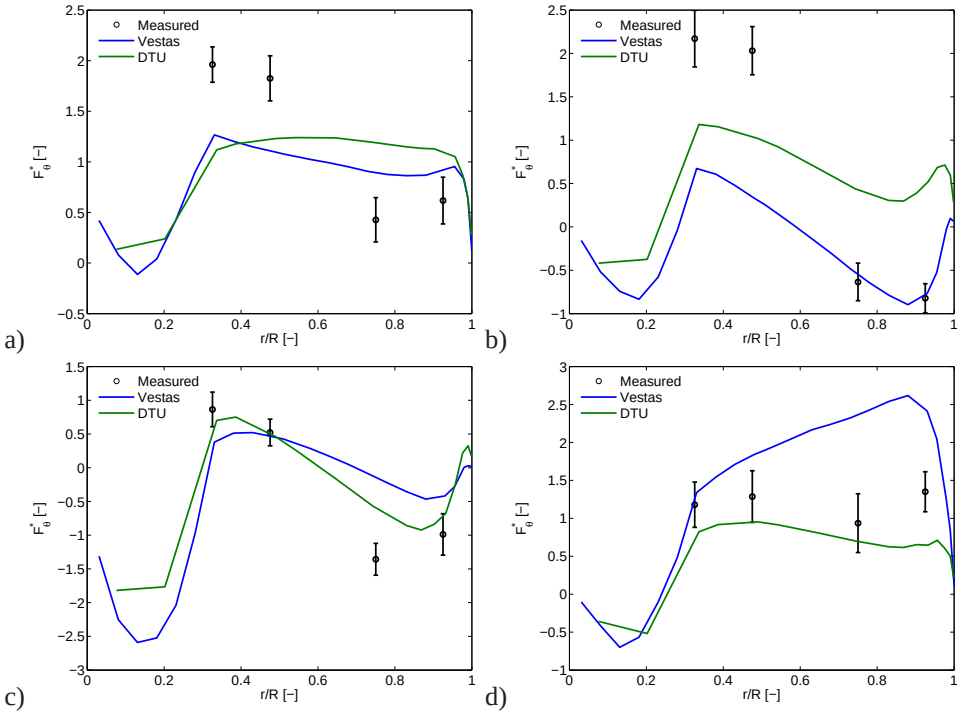

Figure 15.6. Measured and computed tangential loads at four blade positions in the case with a yaw error of -61.5^o. *a)* 0^o *(vertical upwards); b)* 90^o*; c)* 180^o*; d)* 270^o.

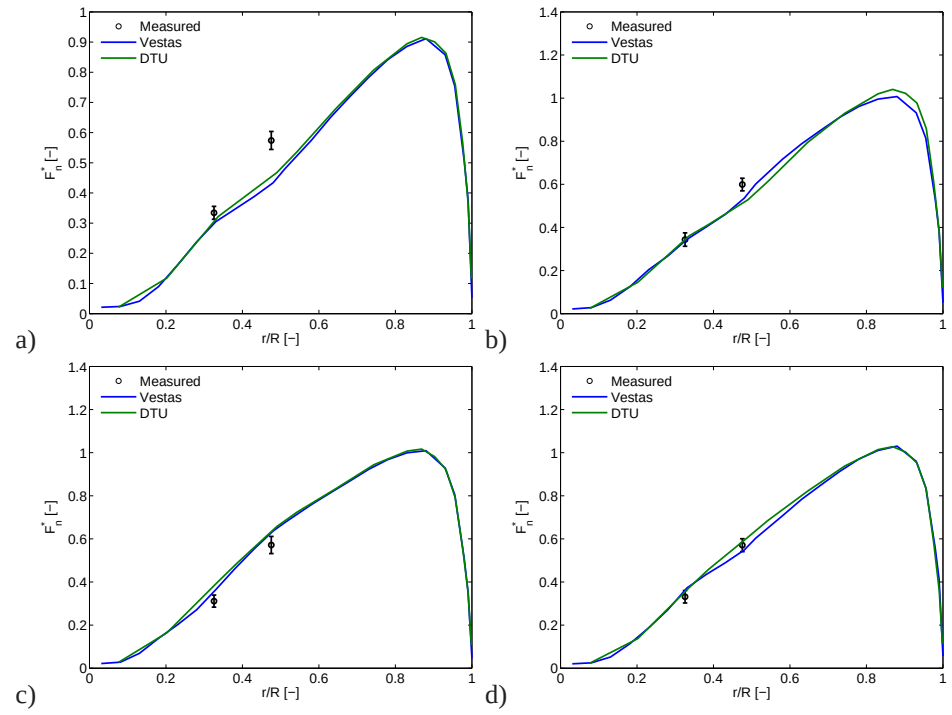

Figure 15.7. Measured and computed normal loads at four blade positions in the case with a yaw error of -17.1^o. *a)* 0^o *(vertical upwards); b)* 90^o*; c)* 180^o*; d)* 270^o.

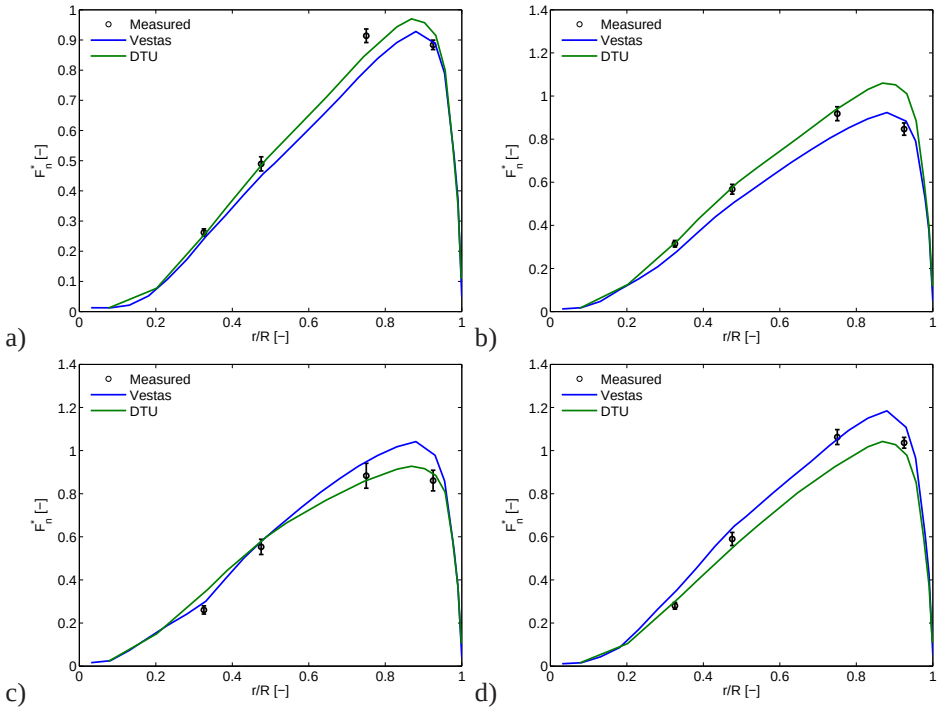

Figure 15.8. Measured and computed normal loads at four blade positions in the case with a yaw error of -38.6^o. *a)* 0^o *(vertical upwards); b)* 90^o*; c)* 180^o*; d)* 270^o.

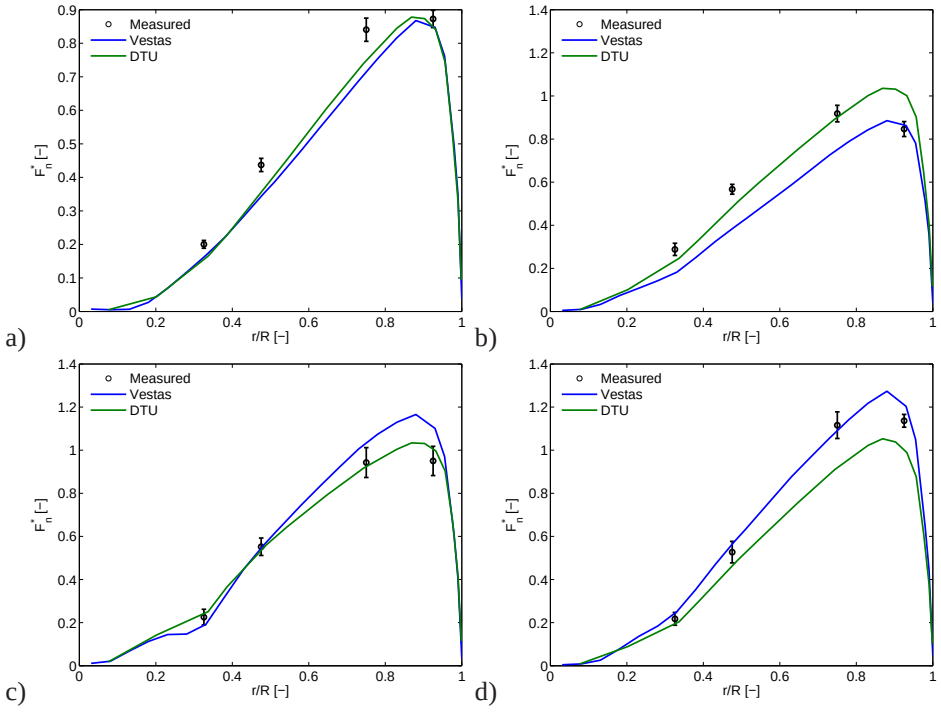

Figure 15.9. Measured and computed normal loads at four blade positions in the case with a yaw error of -61.5^o. *a)* 0^o *(vertical upwards); b)* 90^o*; c)* 180^o*; d)* 270^o.

For the other two yaw cases there are significant differences in the predictions especially in the tangential loads and when the blade is in the horizontal positions. The deviations between the model predictions indicate different implementation of the sub models used to handle yawed inflow conditions.

When comparing computed and measured torque/power it is clear that there are large discrepancies, see Table 15.4. The reasons for these discrepancies are not yet fully known but as will discussed in section 15.5 could be partly due to inaccurate aerofoil data.

	Yaw angle [^{o}]	P/P_{DTU} [-]	τ/τ_{DTU} [-]	T/T_{DTU} [-]
Measured	-17.1	1.177	1.175	-
Vestas	-17.1	0.994	0.994	1.006
DTU	-17.1	1.000	1.000	1.000
Measured	-38.6	1.259	1.257	-
Vestas	-38.6	0.963	0.963	1.015
DTU	-38.6	1.000	1.000	1.000
Measured	-61.5	2.208	2.207	-
Vestas	-61.5	0.874	0.873	1.030
DTU	-61.5	1.000	1.000	1.000

Table 15.4. Mechanical power, torque and thrust in yawed inflow normalized with predictions by DTU

15.5 Discussion

In the previous section we saw large differences between the measured and computed shaft torque in all cases except for the first. This could suggest that the sub models used for including dynamic inflow (shear, yaw etc.) are insufficient. However, there are also indications that the shaft torque measurements may be inaccurate. This is evident in case 1 where the measured tangential loads are higher than computed whereas the opposite is true for the shaft torque. A potential source of error in the comparison above could also be due to differences in the inflow conditions. Currently, the inflow conditions are determined from measurements at a met mast located about 2.5 diameter from the turbine. In future work we will, where available, use measurements from the WindScanner project (see chapter 4) to verify the accuracy of inflow conditions experienced by the turbine.

Another reason for the observed discrepancies is inaccurate aerofoil data. Figures 15.10 and 15.11 compares the used aerofoil data with the aerofoil data measured directly on the NM80 turbine, see chapter 9. As seen there are large differences for the most inboard and outboard sections. This shows the importance of correcting aerofoil data obtained in wind tunnels before using them for BEM computations. The differences in aerofoil data cannot, however, explain the discrepancies in azimuthal variations.

The significant differences between the predictions by Vestas and DTU in cases 4 and 5, indicate that there is still a need to revisit the sub-models used for handling yawed inflow in BEM codes. The predictions are both obtained using state-of-the-art BEM codes with the same aerofoil data and blade data and thus the observed differences should only be due to differences in modelling dynamic inflow.

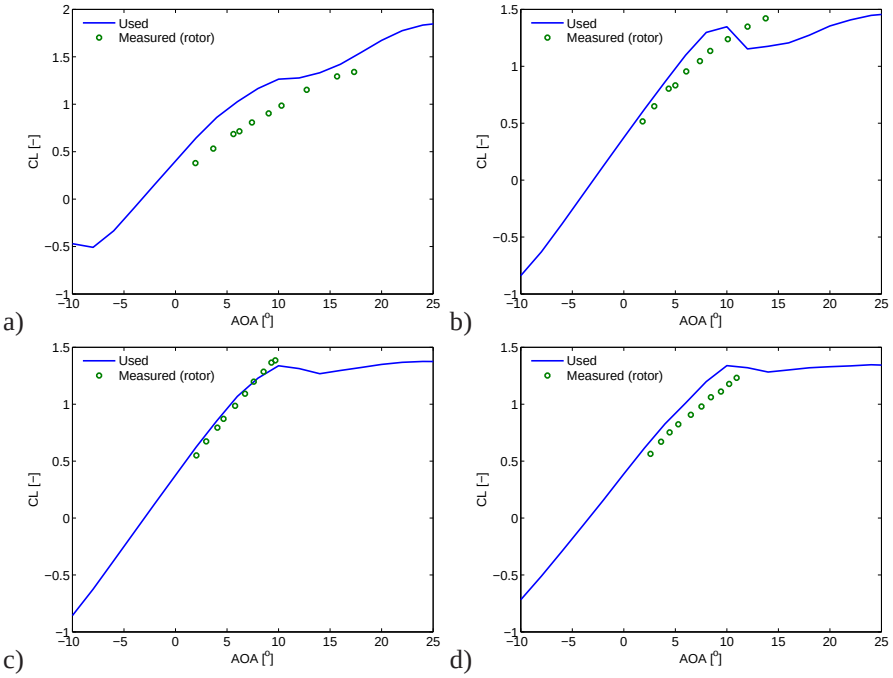

Figure 15.10. Comparison of the used lift polars with those measured on the rotor (see section 9). a) r/R=0.325 (relative thickness 33%); b) r/R=0.475 (relative thickness 24%); c) r/R=0.750 (relative thickness 20%); d) r/R=0.925 (relative thickness 18%).

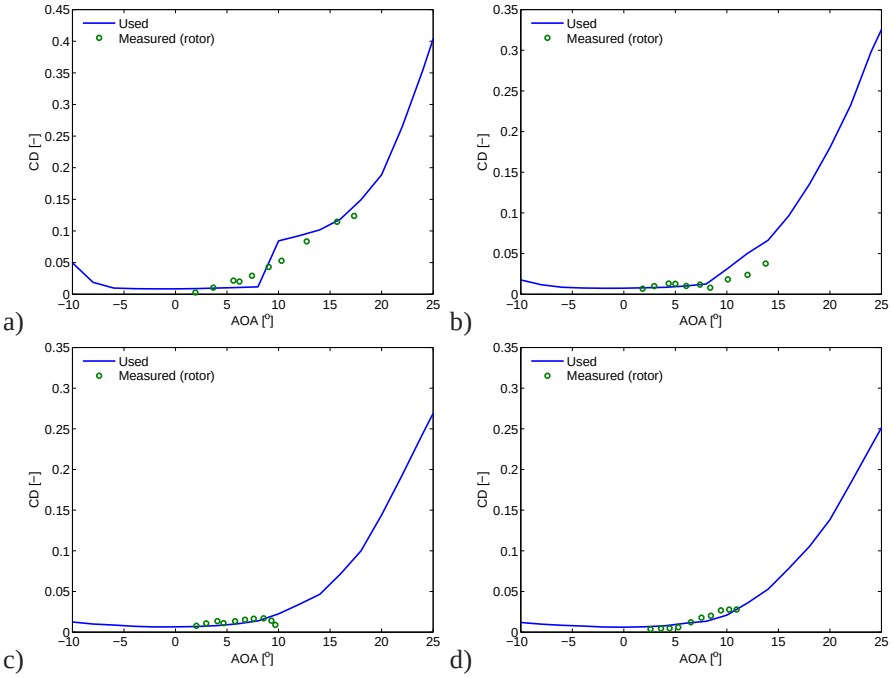

Figure 15.11. Comparison of the used drag polars with those measured on the rotor (see section 9). a) r/R=0.325 (relative thickness 33%); b) r/R=0.475 (relative thickness 24%); c) r/R=0.750 (relative thickness 20%); d) r/R=0.925 (relative thickness 18%).

15.6 Conclusion

A comparison of field measurements and BEM computations of aerodynamic blade forces on the NM80 turbine operating in various inflow conditions has been conducted.

In non-sheared inflow the simulations carried out by Vestas Wind Systems, LM Wind Power, Siemens Wind Power and DTU Wind Energy, respectively, revealed good agreement. Furthermore, the simulated results generally showed reasonable agreement with measurements in this case when considering the standard deviation of the measurements.

In sheared and/or yawed inflow the agreement between measurements and simulations carried out by Vestas Wind Systems and DTU Wind Energy was less favourable. One reason for the discrepancies is shown to be inaccurate aerofoil data and shows the importance of correcting aerofoil data obtained in wind tunnels before using them in BEM computations. However, the used aerofoil data cannot explain the differences in the azimuthal variation of the aerodynamic blade loads as well as the differences between the simulations. Further investigations are required to explain the observed discrepancies.

References

[1] H.Aa. Madsen, V. Riziotis, F. , Zahle, M.O.L. Hansen, H. Snel, F. Grasso, T.J. Larsen, E. Politis, and F. Rasmussen. Blade element momentum modeling of inflow with shear in comparison with advanced model results. *Wind Energy*, 15:63–81, 2012.

[2] C. Bak, H.Aa. Madsen, N. Troldborg, M. Gaunaa, W. Skrzypiński, A. Fischer, U. Paulsen, R. Møller, P. Hansen, M. Rasmussen, and P. Fuglsang. DANAERO MW: Instrumentation of the NM80 turbine and meteorology mast at Tjæreborg. Technical Report DTU Wind Energy Report-I-0083, Technical University of Denmark, 2013.

[3] N. Troldborg. DAN-AERO MW: Potential benchmark cases from the Tjæreborg campaign. Technical Report DTU Wind Energy Report-I-0090, DTU Wind Energy, 2013.

[4] HAWC2aero, the user's manual. Technical Report Risø-R-1631(ver. 1-1)(EN), Technical University of Denmark, 2008.

[5] C. Bak, H.Aa. Madsen, M. Gaunaa, U. Paulsen, P. Hansen, M. Rasmussen, P. Fuglsang, P. Enevoldsen, J. Laursen, and J. Romblad. DAN-AERO MW: Wind tunnel tests. Technical Report Risø-I-3047(EN), Technical University of Denmark, 2010.

[6] C. Bak, J. Johansen, and P.B. Andersen. Three-Dimensional Corrections of Airfoil Characteristics Based on Pressure Distributions. *European Wind Energy Conference, Athens*, 2006.

[7] C. Bak, H.Aa. Madsen, N. Troldborg, N.N. Sørensen, and J. Madsen. DANAERO MW: Data for the NM80 turbine at Tjæreborg Enge for aerodynamic evaluation. Technical Report DTU Wind Energy Report-I-0087, Technical University of Denmark, 2013.

Acknowledgements

This project was partly funded by the Danish Energy Agency EUDP2009-II. The validation of CFD models (chapter 14) was carried out in close collaboration with project "Center for Computational Wind Turbine Aerodynamics and Atmospheric Turbulence" contract no.: 2104-09-0026, which is funded by the Danish Strategic Research Council (DSF).

16 Appendices

A Installing the database

Author(s): N. Troldborg, P.B. Andersen, S.A. Sørensen

This appendix describes how to install the software required for making the database operational on a Windows computer. The database is designed to be used with the MySQL software.

A.1 Installing MySQL client/server

This section describes how to install the client/server MySQL software *MySQL Server 5.1* on a local Windows machine. Note that *MySQL Server 5.1* is an older version of the software but is used here because the database has been tested for this version. However, the database may also work with newer versions. *MySQL Server 5.1* is installed as follows:

- go to http://dev.mysql.com/
- click "archives" under the downloads menu in the bottom of the homepage
- select "MySQL Database Server 5.1"
- In the menu "Software Downloads by Platform" click "Microsoft Windows"
- Select "Microsoft Windows 32. (Windows Installer format)"
- Select "run" when asked if you want to run or download the file. This will start the installation wizard:
  - Step 1: Click "Next"

– Step 2: Tick "I accept the terms in the license agreement" and click "Next"

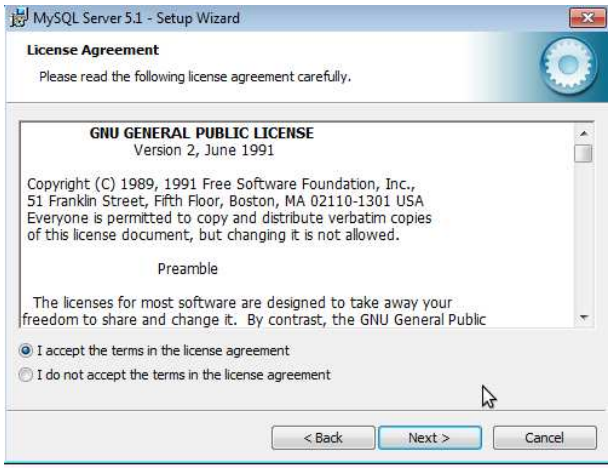

– Step 3: Choose "Typical" and click "Next"

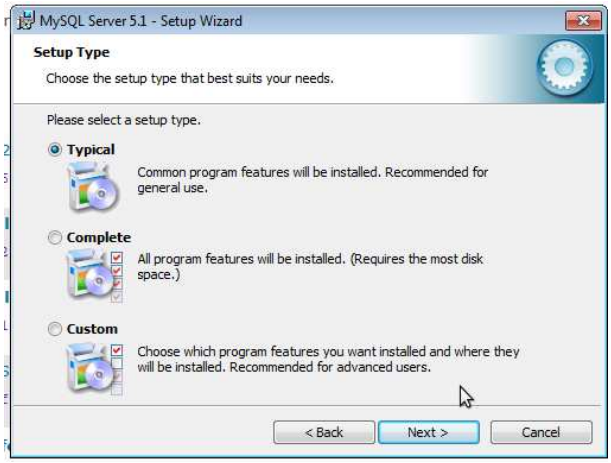

– Step 4: Click "Install"

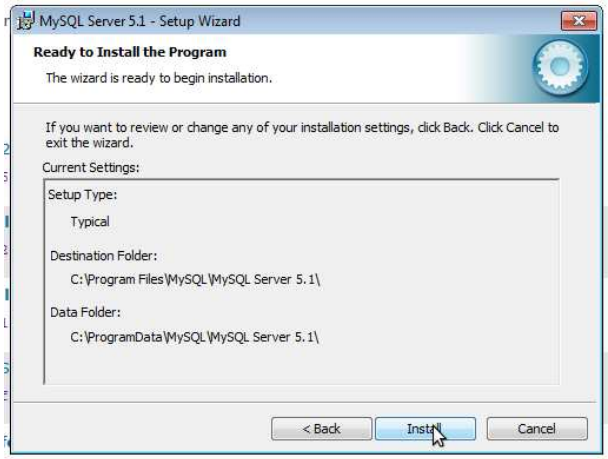

– Step 5-7: Confirm installation and click "Next" through the advertisements

– Step 8: Choose "Configure the MySQL Server now" and click "Finish"

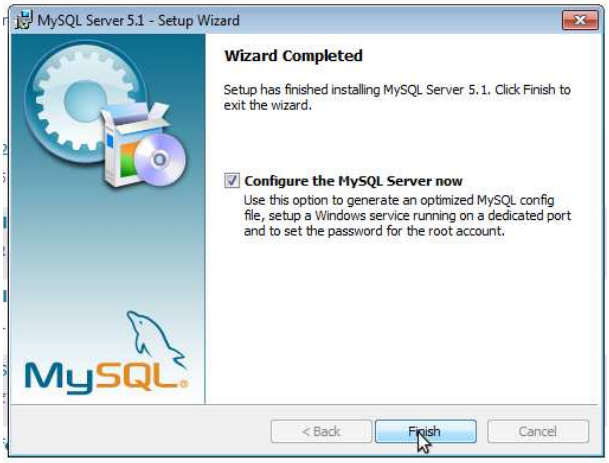

– Step 9: Click "Yes"

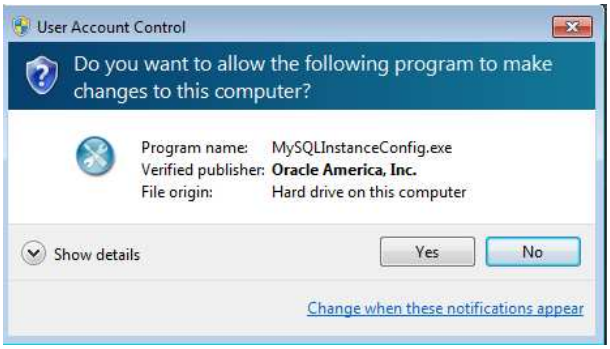

– Step 10: Click "Next"

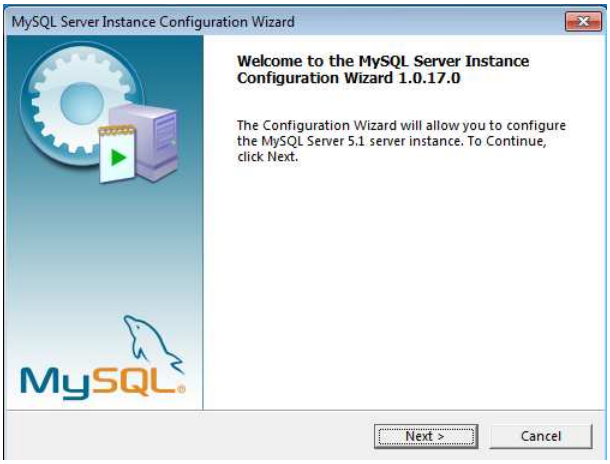

– Step 11: Choose "Detailed Configuration"

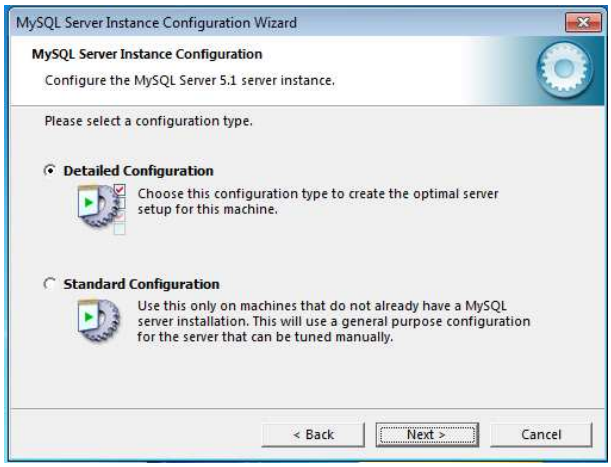

– Step 12: Choose "Developer Machine"

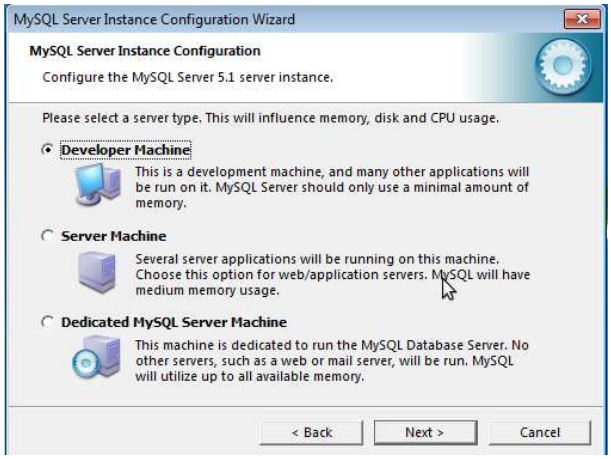

– Step 13: Choose "Non-Transactional Database Only" and click "Next"

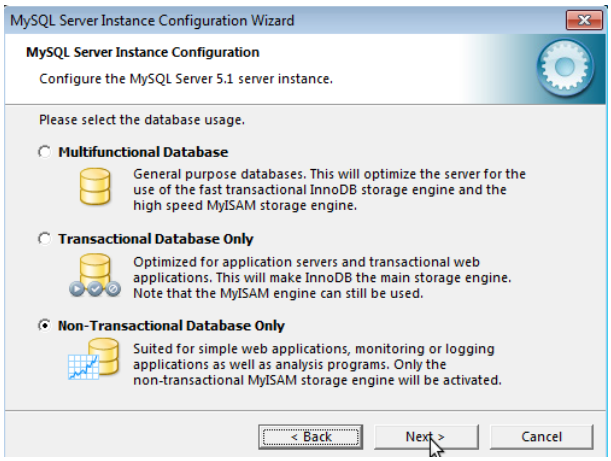

– Step 14: Choose "Manual Settings" and select number of concurrent users (this may be changed later). Then click "Next"

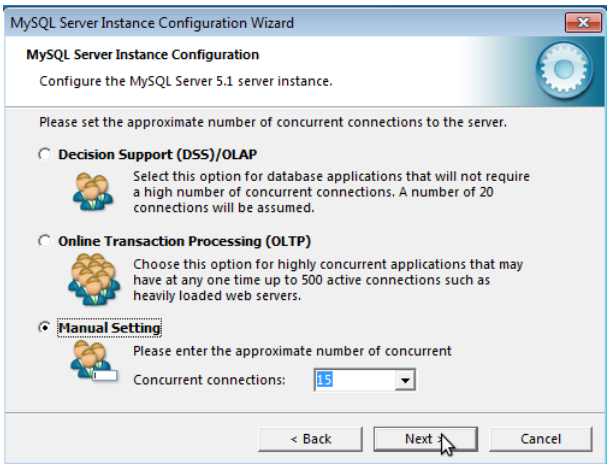

– Step 15: Tick "Enable TCP/IP Networking", "Add firewall exception for this port" and "Enable Strict Mode". Then click "Next".

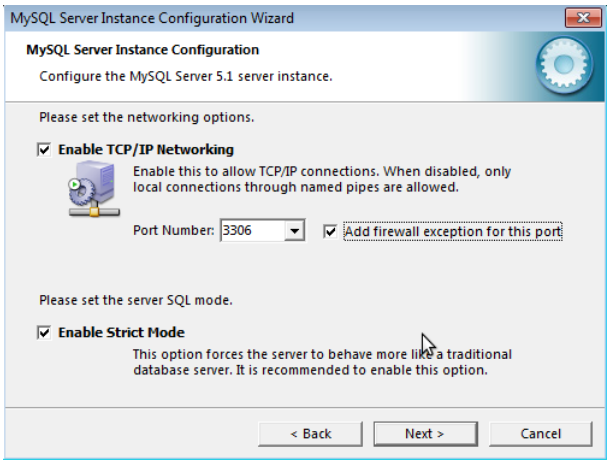

– Step 16: Choose "Standard Character Set" and click "Next"

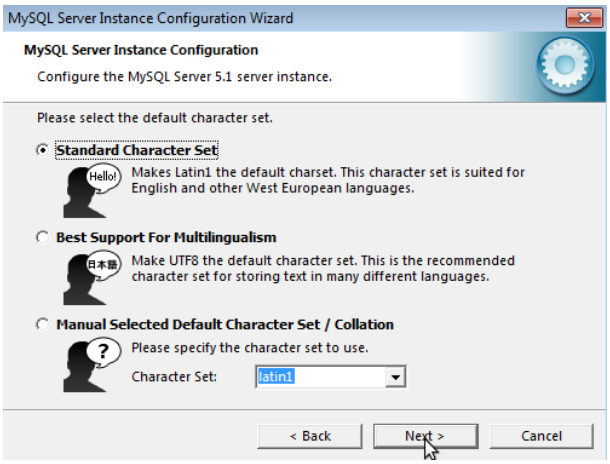

– Step 17: Choose "Install As Windows Service" and click "Next"

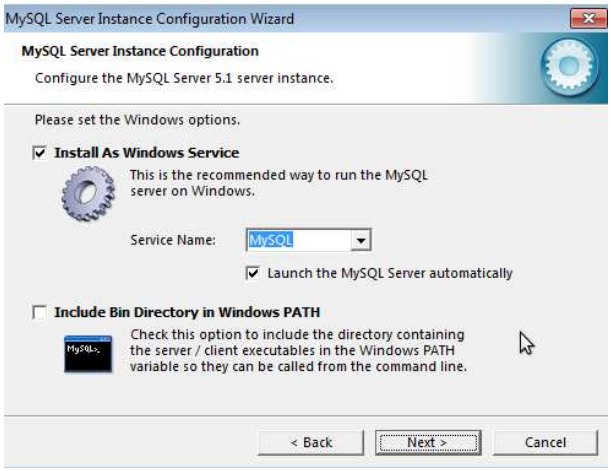

– Step 18: Choose a password for the root and click "Next"

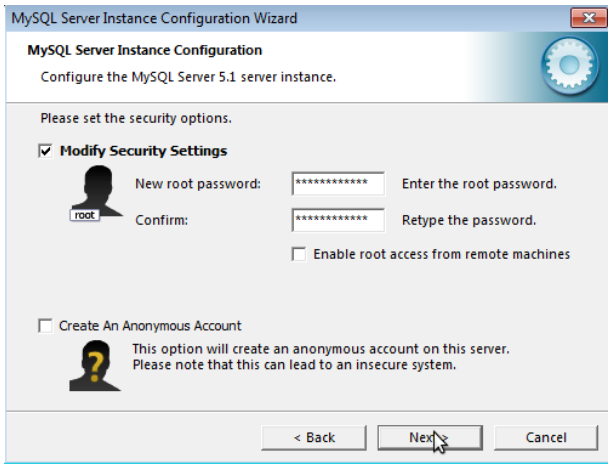

– Step 19: Click "Execute"

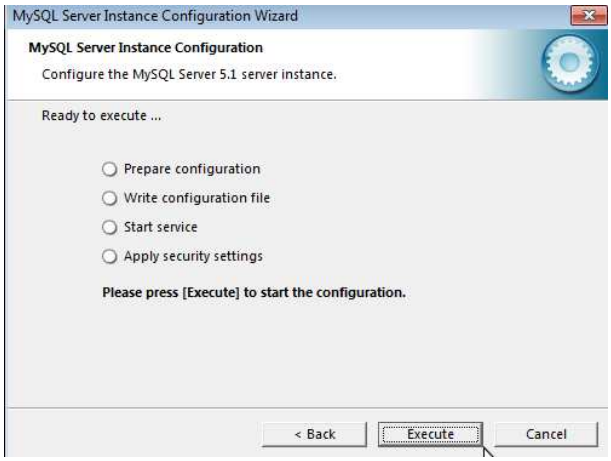

– Step 20: Click "Finish"

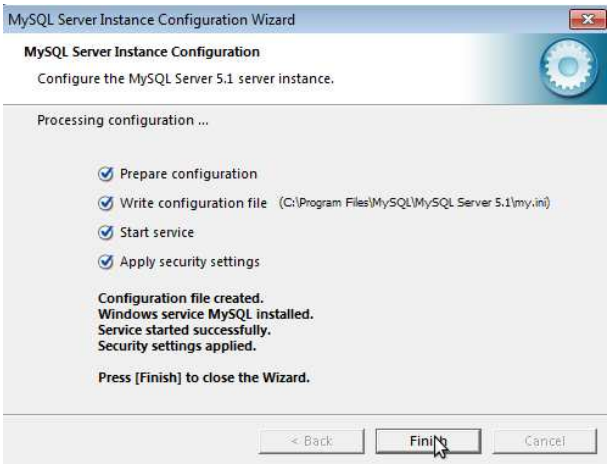

A.2 Installing GUI tools for the client

In order to simplify setting up the database and to search it for data it is recommended to install a MySQL GUI tool. This section shows how to install the tool *MySQL Tools for 5.0*, which is a small program which facilitates administrating the databases as well as searching in the database. The program is installed for Windows as follows:

- go to http://dev.mysql.com/
- click "archives" under the downloads menu in the bottom of the homepage
- select "MySQL GUI Tools"
- In the menu "Software Downloads by Platform" click "Microsoft Windows"
- Select "Microsoft Windows 32. (Windows Installer format)"
- Select "run" when asked if you want to run or download the file. This will start the installation wizard:
  - Step 1: Click "Next"

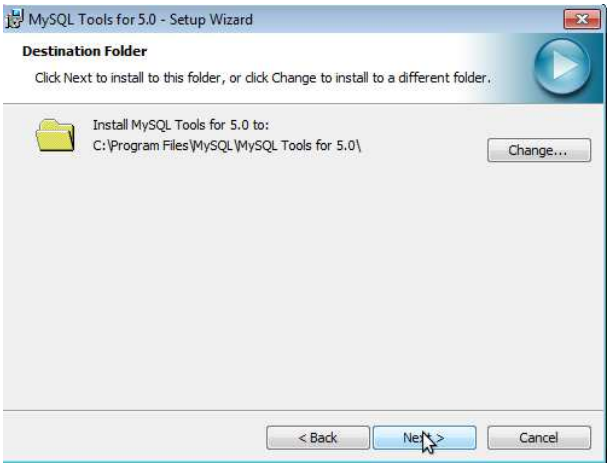

– Step 2: Choose "Complete" installation and click "Next"

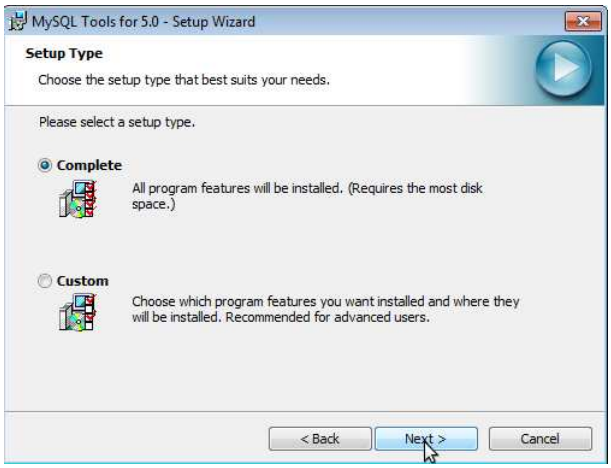

– Step 3: Click "Finish"

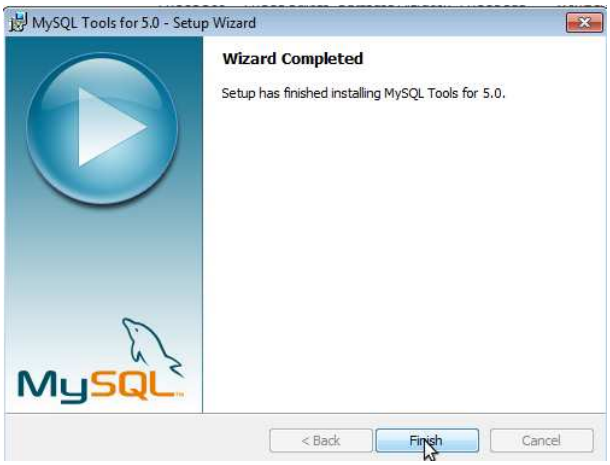

A.3 Setting up the database

To set up the database start the program *MySQL Administrator*. You will be asked for your password.
When the program starts you will be presented for a menu as shown in Figure A.1. By clicking the sub menu "Startup Variables" on the left you will get a menu as shown in Figure A.2. In "Data Directory" you can see the current path to the database. This is where the files in the database on the external hard disk should be copied to.
In the sub menu "Catalogs" on the left there is a list of all the databases available. They are located in the "Data Directory" mentioned above. In the shown case (Figure A.3) a folder has already been made which is called "danaero" where the data from the database will be copied to. This folder can be made either by right clicking the mouse in the list of schemata and select "Create New Schema" or by going to the folder through explore (in this case the data files are located in "C:/ProgramData/MySQL/MySQL Server 5.1/Data/" (note that the files may be hidden). After creating a folder in the data directory then copy the contents of the database into that folder. Now, the database is ready for use with *MySQL Query Browser* or any other MySQL tool you would like to use for searching the database.
Note that if a server is already existing then it suffice to copy the contents of the database on the external hard disk to the data folder of this server in order to make the database working.

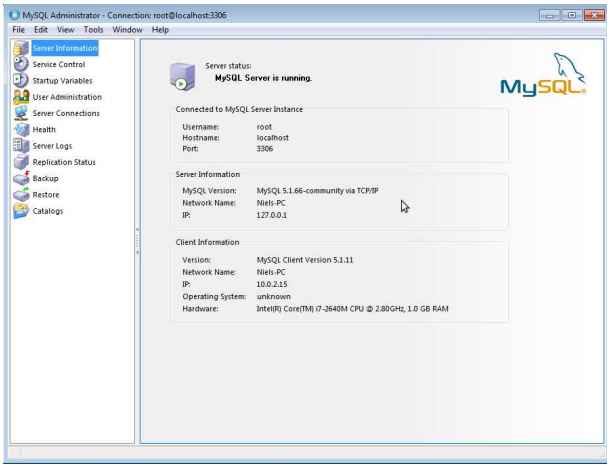

Figure A.1.

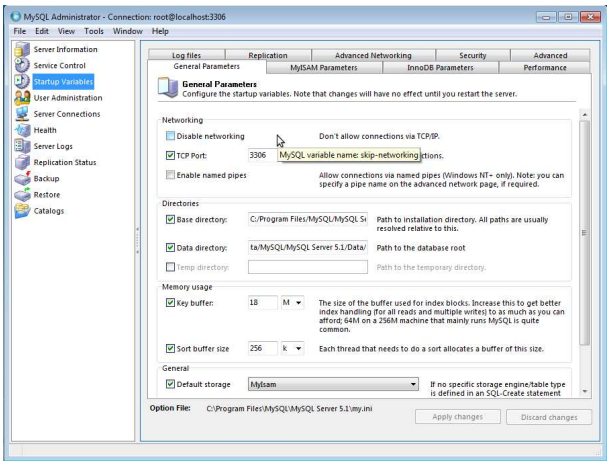

Figure A.2.

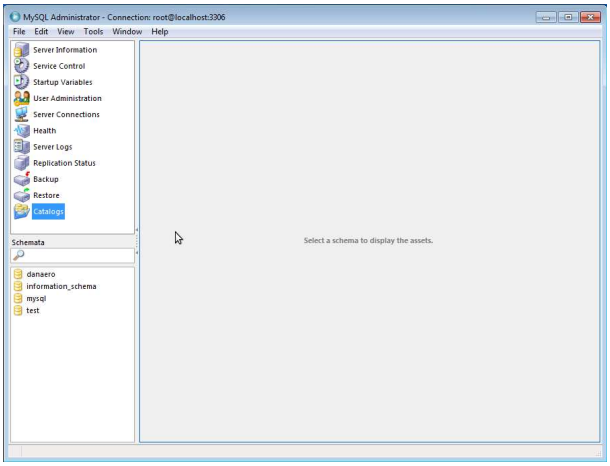

Figure A.3.

DTU Wind Energy is a department of the Technical University of Denmark with a unique integration of research, education, innovation and public/private sector consulting in the field of wind energy. Our activities develop new opportunities and technology for the global and Danish exploitation of wind energy. Research focuses on key technical-scientific fields, which are central for the development, innovation and use of wind energy and provides the basis for advanced education at the education.

We have more than 230 staff members of which approximately 60 are PhD students. Research is conducted within 9 research programmes organized into three main topics: Wind energy systems, Wind turbine technology and Basics for wind energy.

Technical University of Denmark
DTU Vindenergi
Frederiksborgvej 399
Building 118
4000 Roskilde
Denmark
Telefon 46 77 50 85
info@vindenergi.dtu.dk
www.vindenergi.dtu.dk